Effects of Viscosity on Hydrofoil Cavitation

by

RANDALL A. VILLENEUVE

B.S., University of Massachusetts (1990)

Submitted to the Department of Ocean Engineering in partial fulfillment of the requirements for the degrees of

Master of Science in Ocean Engineering

Master of Science in Mechanical Engineering

at the

MASSACHUSETTS INSTITUTE OF TECHNOLOGY
May 1993

Author.....
Department of Ocean Engineering
May 7, 1993

Certified by.....
Spyros Kinnas, Lecturer and Principal Research Engineer
Department of Ocean Engineering, Thesis Supervisor

Certified by.....
Harri Kytomaa, Associate Professor
Department of Mechanical Engineering, Thesis Reader

Accepted by.....
A. Douglas Carmichael, Chairman
Departmental Committee on Graduate Students
Department of Ocean Engineering

Accepted by.....
Ain A. Sonin, Chairman
Departmental Committee on Graduate Students
Department of Mechanical Engineering

Effects of Viscosity on Hydrofoil Cavitation

by

Randall A. Villeneuve

Submitted to the Department of Ocean Engineering on May 7, 1993, in partial fulfillment of the requirements for the degrees of

Master of Science in Ocean Engineering
and
Master of Science in Mechanical Engineering

Abstract

Presented herein, is a method for the analysis of the steady, viscous, cavitating flow about a two dimensional hydrofoil. This method is based on a low order perturbation potential formulation. Coupling of the cavitating and viscous portions of the flow is completed through the use of blowing sources. Implementation of this method, resulted in the code P2D-BLWC. The method has been shown to be convergent. Results compare favorably with those due to existing methods for the case of inviscid flow. Tests of the validity and consistency of the method for viscous cavitating flow results, gave favorable results.

As part of this research, experiments were conducted on a foil of constant chord length in a water tunnel. The conditions were such that the flow about the foil was partially cavitated. The experimentally measured displacement and momentum thicknesses, and the force coefficients, were compared with the numerical results. To account for the tunnel walls, the method was modified to include image effects.

Thesis Supervisor: Dr. Spyros Kinnas, Department of Ocean Engineering
Thesis Reader: Prof. Harri Kytomaa, Department of Mechanical Engineering

Acknowledgments

I thank my advisor, Dr. Spyros Kinnas, for his patience, advice and support. My gratitude is also extended to my thesis reader, Professor Harri Kytomaa, and academic advisor, Professor Justin Kerwin, for their helpful comments.

Support for this work was provided by the Office of Naval Research (Contract No. N00014-90-J-1086), and the Department of Defense through the National Defense Science and Engineering Graduate Fellowship.

I was fortunate in that I never had to work alone in graduate school. There were always other students and friends to confer with, seek aide from, or even whine to if necessary. I would like to thank them all, especially the members of the prop group, my office mates, and Ben, Beth, Manoj and Neal.

Everyone has had people who have influenced their life, and supported them in their pursuits. I am no exception to this, and would like to thank each of these people. Peter Hendricks, who gave me the idea about grad school in the first place. Walter Lambert and Al LaBeet, who looked the other way when I was doing homework. My father and mother in-law, Dennis and Lynda Vasconcellos, and grandmother, Evangeline Vasconcellos, each of whom were there when times were tough.

Finally, I wish to thank my wife Lisa. This poor engineer cannot think of the words which would begin to do her justice. Let me just say that, more than any other, her love, devotion and support have served to shape my life and inspire me. No man would have asked so much or have gotten better from his wife. I dedicate this thesis to her.

Table of Contents

List of Figures

List of Tables

List of Symbols

A	velocity fraction for pressure recovery model
A_{eff}	effective value of A given as $1-U^{cte}/q_c$
A_{ij}	potential induced at i the body and wake dipole distributions
$\underline{A}$	matrix for cavity solution defined in Section 3.1
B_{ij}	potential induced at point i due to a source distribution on panel j
C_D	drag coefficient
C_L	lift coefficient
C_f	friction coefficient
C	pressure coefficient
$C_\tau, \delta C_\tau$	coefficient of maximum shear stress
$C_{ij}, \tilde{C}_{ij}, \tilde{C}'_{ij}$	influences at i due to cavity blowing source distribution on panel j
c	chord length
D^c_{ij}	contribution to edge velocity at point i due to cavity mass defect j
D^v_{ij}	contribution to edge velocity at point i due to viscous mass defect j
$F(s_C)$	continuous pressure recovery function
F_i	discrete pressure recovery function
f_d	doppler frequency
G	two dimensional Green's function
H	shape parameter given by δ^* / θ or distance between tunnel walls

H^*	kinetic energy shape parameter given by θ^* / θ
H^{**}	density shape parameter given by δ^{**} / θ
H_k	kinetic shape parameter, which is equal to H for incompressible flow
h	cavity height
$\underline{J}^c$	cavity Jacobian
$\underline{J}^v$	Jacobian for boundary layer solver
k	reduced frequency given by $\omega c/U_\infty$ or cavity panel index
LE	leading edge
l	cavity length defined as arc length from cavity LE to TE
l_i	length scale for *ith* averaging interval
M_{cte}	mass flux through TE of cavity
m^c	cavity mass defect
Δm^c	tolerance of cavity mass defect
δm^c	perturbation to cavity mass defect
m^v, δm^v	viscous mass defect and its perturbation
N	number of panels on body or number of counts for velocity average
N_{bc}	number of panels between LE of foil and cavity LE
N_c	number of cavity panels
NIMG	number of image pairs
N_w	number of wake panels
$\bar{n}$	normal vector
$\tilde{n}$, $\delta\tilde{n}$	amplitude of Tollmein-Schlichting waves and its perturbation
$\tilde{n}_{crit}$	critical amplitude of Tollmein-Schlichting waves

p_C	cavity pressure
p_V	vapor pressure
p_∞	pressure of free stream
q_C	constant part of cavity velocity given as $\sqrt{1+\sigma}$
Δq_C	tolerance of q_C
δq_C	perturbation to q_C
$q(s_C)$	velocity distribution on cavity surface
R	distance used in evaluating Green's function
R_e	Reynolds number based on chord length
$R_{e\theta}$	Reynolds number based on momentum thickness
$\underline{R}^c$	residual for cavity iteration
$\underline{R}^v$	residual for boundary layer solution
$S_{C\min}$	point of minimum pressure in fully wetted flow
S_D	cavity detachment point
S_{SC}	point of separation in cavitating flow
S_{SFW}	point of separation in fully wetted flow
S_b	denotes surface of body
S_w	denotes wake surface
$\tilde{S}_{ij}$	potential induced at point *i* due to a dipole distribution on panel *j*
$\left(\tilde{S}_{ij}\right)_{2w}$	influence coefficient $\tilde{S}_{ij}$, including the effects of the wall images
s	arc length on foil surface, measured from the LE

s_c	arc length on surface underneath cavity, measured from the cavity LE
s_λ	cavity arc length at the start of the transition zone
T	surface tension coefficient
TE	trailing edge
t	distance from tunnel centerline to tunnel wall
U^{cte}	velocity at TE of cavity
ΔU^{cte}	tolerance of velocity at TE of cavity
δU^{cte}	perturbation of velocity at TE of cavity
U_e	edge velocity
U^{inv}	velocity at body surface for inviscid fully wetted flow
U_{inv}	approximation to inviscid velocity profile, used in data anslysis
U_∞	magnitude of free stream velocity
u	boundary layer velocity, nondimensionalized by U_e or particle velocity
u'	perturbation to u
u_{bl}	reconstructed boundary layer profile
u_{meas}	measured particle velocity
$\hat{u}$	particle velocity obtained by smoothing the measured profile
Δu_R	defect of streamwise velocity in the wake
$V_{ij}, \tilde{V}_{ij}, \tilde{V}'_{ij}$	influences at i due to viscous blowing source distribution on panel j
$\vec{v}$	velocity vector
v	transverse component of velocity

W_i	potential induced at point i due to wake dipole distribution
W_{jk}	weights used in velocity profile smoothing
$\underline{x}$	solution vector for cavity variables
α	angle of attack
Δ	offset of source location from tunnel centerline
δ^*	displacement thickness
δ^{**}	density thickness, which is zero for compressible flow
δ_{ij}	Kronecker delta which is equal to 1 when $i=j$, 0 otherwise
Φ	total potential
Φ_{in}	potential for the free stream
ϕ, ϕ_p	perturbation potential and its value at point p
ϕ_{s1w}	potential for a source near an infinite wall along the horizontal axis
ϕ_{s2w}	potential for a source between two infinite, parallel, horizontal walls
$\phi_{S\infty}(x_s, y_s)$	potential for a source at (x_s, y_s) for an infinite domain
$\phi_{SIMG}(x_i, y_i)$	potential due to the image source at (x_i, y_i)
ϕ_i^{inv}	perturbation potential at panel i for inviscid fully wetted flow
$\Delta\phi_w$	jump in perturbation potential at TE of foil
Γ	circulation around the body or strength of point source
η	boundary layer coordinate, in the direction normal to wall
λ	length of transition zone
λ_d	wavelength of incident beam for LDV measurements
λ^*	distance between boundary layer separation and cavity detachment
μ	absolute viscosity

υ	parameter for pressure recovery model
θ, $\delta\theta$	momentum thickness and its perturbation
θ_{SFW}	momentum thickness at point of separation in fully wetted flow
θ_d	half angle of converging beams for LDV measurements
θ^*	kinetic energy thickness, $\int u^2\left[1-u^2\right]d\eta$
ρ	fluid density
σ	cavitation number defined as $\left(p_\infty - p_c\right)/\frac{1}{2}\rho U_\infty^2$
ω	frequency of free stream fluctuations
∇	del or gradient operator

1. Introduction

Turbomachines and propellers have held a key role in many industries, for over two hundred years. Consider for instance public utilities, and their great reliance on turbomachinery for power generation. Another example of significance, is the use of propellers and hydrofoils by the marine and naval industries. Further examples could be cited, but these should be enough to illustrate that the effective design of hydraulic devices is essential to industry. Better designs would increase performance, thereby decreasing operating costs and reducing the demand for precious natural resources.

As a result of this need for improved design of hydraulic devices, engineers are required to have a greater understanding of the flow in and about these mechanisms. For decades they have made use of empirical and analytical tools, to aide in their studies. Now, with the advent of digital computers, engineers have available to them even more powerful tools for flow analysis. Using this new technology, it is no longer necessary to overly simplify or neglect many important effects as in the past. This development has been a boon to the designers of hydraulic devices. Now they can more easily address two of the greatest technical difficulties associated with their work: viscous effects; and cavitation.

Viscous effects are of primary importance when considering the design of turbomachines, hydrofoils, and propellers. The reason for this is no matter what one does to decrease the effects of viscosity, the flow is affected to some degree. Take for example the turbine blade of Figure (1-1). If one neglects to account for the influence of viscous

effects in their design, it is quite possible that the boundary layer could separate, resulting in an increase in drag and a reduction in lift. An effective design is one for which the boundary layer on the blade is thin and stable, resulting in lower drag. We see from this example, that though the influence of viscous effects on the flow can be decreased, they are always present to some level.

Cavitation, though the focus of this work, must in general be relegated to a position of secondary importance. The reason for this is that in many applications, it is possible to avoid cavity formation through the use of improved designs, or by sacrificing on operating performance. However, when cavitation does occur, its side effects, as opposed to those due to viscous effects, are of greater detriment. Consider for instance the cavitating propeller blade of Figure (1-2). The cavities shown can impact on the blade surfaces causing erosion, and produce large changes in drag or thrust. Considering these effects, and the fact that cavitation is in many recent high speed applications unavoidable, one realizes the importance of its study.

The analysis of viscous flows and their effects on hydraulic machines, has evolved quite rapidly over the course of the past century. This evolution has resulted in the gradual supplantation of analytical methods by numerical methods. Conversely, the development of techniques for the analysis of cavitating flow has been somewhat slower. Unlike their colleagues, cavitation researchers have relied heavily on analytical techniques, like those due to Wu [24], Tulin [21] and Leehey [15]. However, numerical calculations have gained in popularity, thanks to the efforts of researchers such as Uhlman [23], Lemonnier and Rowe [16], and Kinnas and Fine [12].

The development of numerical techniques for the analysis of cavitating flow, has allowed researchers to address such issues as nonlinearity, unsteadiness, and complex geometries. However, most existing numerical techniques are based on the assumption that the flow is everywhere inviscid. While this simplification does not greatly alter the general character of cavitation, it has a strong influence on cavity parameters such as

detachment, cavity length and volume. Development of methods for modeling cavitating viscous flows, is paramount to the continued improvement in the design of turbomachines and propellers.

This paper describes the author's efforts to address the problem of cavitating flow about impellers and propellers. Since this problem is a formidable one, it was necessary to limit the scope of this study to the steady cavitating flow about 2-D hydrofoils. 2-D Hydrofoils were chosen because they are fundamental to the design of turbine blades, lifting surfaces and propellers. This study is further limited to large sheet cavities which are attached to the suction side of the foil as shown in Figure (1-3). Other forms of cavitation, such as bubble, cloud, and tip (see Section 1.2 for the distinction between each form of cavitation), will not be addressed in this work.

The work described here took place in two stages. First, a model for partial sheet cavities about hydrofoils was formulated. The formulation of this model is discussed in Chapter 2. This formulation was implemented numerically, and the result is the code P2D-BLWC, which is discussed in Chapter 3. The second stage included experimentation for a partially cavitating hydrofoil as described in Chapter 4. The measurements from this experiment were used to determine empirical parameters used in the model, and for comparison with model results.

In Section 1.1, the objectives of this work are stated. A general overview of cavitation is presented in Section 1.2. This is followed by the assumptions made in modeling the flow. The chapter then closes with a brief review of research to date, which is pertinent to this study.

1.1. Objectives

As described in the last section, this research has been conducted in two stages. The focus for the first stage of this work was on modeling considerations. The objectives associated with this stage were three-fold:

(1) First it was necessary to formulate a model for the analysis of cavitating viscous flow about hydrofoils in two-dimensions. A method was chosen which models the interaction of the viscous and inviscid portions of the flow using a blowing source distribution on the body and wake surfaces. In this method the cavity, which is treated as part of the inviscid flow, is also modeled using blowing sources located on the foil beneath the cavity. As part of the inviscid solution, the cavity influence is felt via the inviscid velocity distribution which is used in the boundary layer solution. The formulation of the viscous model is due to Drela [3].

(2) The second objective was to implement the method. The code which resulted is P2D-BLWC. This code is actually a modification of PAN2D-BL, which is described in [8]. PAN2D-BL uses a low order perturbation potential method, which is coupled to Drela's viscous solver by means of the viscous blowing source distribution. It was necessary to modify PAN2D-BL to include the effects of cavity blowing sources. A Newton iterative technique was then used to determine the cavity height distribution required to satisfy the dynamic boundary condition on the cavity surface.

(3) In the course of this work comparisons of numerical and experimental results were required. However, the formulation discussed applies only to foils in an infinite domain, while the foil was tested in a tunnel. It was necessary to account for the wall effects by using the method of images.

The experimental stage was guided by the need to satisfy the following goals:

(1) In this work some empirical parameters are used in the model. These parameters pertain to the closure of the cavity. One goal was the experimental determination of these parameters.

(2) The final goal of this work, was the comparison of numerical and experimental results. Comparisons were based on integral parameters such as boundary layer displacement and momentum thicknesses. Lift and drag force coefficients were also measured and compared with those from the numerical model.

1.2. Cavitation - An Overview

In this section a brief overview of cavitation is presented. Issues of relevance to the study of cavitation are discussed. Topics include inception, types of cavitation, closure models, and the generally accepted terminology.

Cavitation is the formation of regions of vapor within a flowing fluid. These regions form wherever the local pressure falls below some minimum pressure. This pressure, which is denoted here as p_v, is called the vapor pressure. The concept of vapor pressure is well known, and values for it as a function of temperature can be obtained for water from many sources. However, in the case of cavitation, where you have a flowing fluid with impurities, the actual vapor pressure is in general different than the value obtained from such sources. This is due to the presence of air nuclei in the fluid, other impurities in the media, surface tension and viscosity. Much research has gone into determining how these factors influence the vapor pressure, and therefore cavity inception. But it is still vague as to what this pressure should be for a fluid at arbitrary conditions.

When cavities form, they have traditionally been characterized by their shape, size, and proximity to solid boundaries. The result is four relatively distinct types of cavities: bubble; cloud; tip; and sheet. Examples of each type are shown in Figures (1-2) and (1-4). What follows is a brief description of each type:

(1) Bubble cavities are typically the most abundant type. They have a wide range of sizes. What delineates them from the other types is that each bubble is independent of the others, and they are advected by the flow.

(2) Cloud cavitation is really a large group of very small bubble cavities which have been entrained in some region of the flow. This type of cavitation is typically found behind sheet cavities.

(3) Cavities also form at the tips of cavitating propellers and lifting surfaces. These so-called tip cavities, result from the low pressures found at the core of tip vortices. One feature of interest (from an aesthetic point of view) are the helical trajectories of these cavities when seen in the wake of a rotating propeller.

(4) Sheet cavities appear as large pockets of vapor which are attached to a solid boundary. They can form on or behind blunt bodies or lifting surfaces. In general, while it is possible to clearly define a cavity surface (defined as the interface between the liquid and vapor), this surface can oscillate rapidly and is less clearly defined near its trailing edge.

While each form of cavitation is important, only sheet cavities will be addressed in the present work. The reason for this is that in marine and hydraulic applications, sheet cavities are usually quite common. They also tend to be of larger volume relative to other forms and have a greater influence on performance. It must also be admitted that the treatment of sheet cavities is much simpler than that of cloud or bubble cavitation. For instance with bubble cavitation, one must account for a large number of independent bubbles which are advected by the flow and varying with time. Accounting for all forms of cavitation is beyond the scope of this work.

As stated earlier, sheet cavities form on or behind blunt bodies or lifting surfaces, as shown in Figure (1-5). They are classified according to their size in relation to the bodies they are attached to. The result of this classification are two distinct types of sheet cavities, and an example of each is shown in Figure (1-6) and Figure (1-7). The first is a

partial cavity, which has a length that is smaller than the chord length. The other type is a supercavity, which extends from a point on the body past the trailing edge. In both cases the cavity starts at a point on the body, called the detachment point. Note that for the case of supercavities, two detachment points are possible. The surface of the cavity usually is assumed to be of constant pressure over most of its extent. However, near the trailing edge, this assumption is in general not valid. Near the trailing edge of the cavity, experiments have shown that the surface is less well defined and tends to oscillate. Modeling this zone near the cavity trailing edge, and determination of the detachment point are key issues when studying sheet cavities.

Detachment has been studied extensively by many researchers. As a result, several theories for the prediction of detachment exist. The classic condition is that of smooth detachment. In this theory detachment occurs at the point of minimum pressure, and the cavity velocity and curvature is required to be continuous there. However, observation has shown that detachment occurs after the point predicted by this theory. Brennen [2] has conducted experimental investigations, which have shown a relation between Reynolds number and detachment for blunt bodies. Arakeri [1] went on to show for blunt bodies, detachment occurs at some length, λ^*, after the point of laminar boundary layer separation for fully wetted flow. The arc length at detachment, S_D, is given by

$$S_D = S_{SC} + \lambda^* \tag{1.1}$$

where, S_{SC} is the point of laminar boundary layer separation for the cavitating flow. Arakeri found that this point is related to the point of separation for fully wetted flow, S_{SFW}, by

$$S_{SC} = S_{SFW} - 2.37\left[1 + \sigma/\left(C_p\right)_{FW}\right] \times \left[S_{SFW} - S_{C\min}\right] \tag{1.2}$$

where, σ is the cavitation number, $\left(C_p\right)_{FW}$ is the minimum pressure coefficient for the fully wetted flow, and $S_{C\min}$ is the position where the pressure is a minimum for the fully wetted flow. The length λ^* is given in terms of θ_{SFW}, the momentum thickness at separation for fully wetted flow, as

$$\lambda^* = \theta_{SFW}\left\{130 - 312\frac{\mu U_\infty}{T}\left[1-\left(C_p\right)_{FW}\right]\right\} \tag{1.3}$$

Franc and Michel [6] found a similar connection between detachment and laminar boundary separation for hydrofoils. However, the criterion they formulated for detachment is not as precisely defined as that due to Arakeri.

The region near the trailing edge of the cavity is very complex. In this region the surface of the cavity is not well defined and it tends to oscillate. There is also a mass flux between the cavity and the external flow. Experiments by Meijer have shown that the pressure in this region tends to increase [17]. Different models for this transition zone have been used. Uhlman [23] used a modified Riabouchinsky model, in which the cavity is terminated with a plate normal to the foil surface. Lemonier and Rowe [16] and Kinnas and Fine [12] have used a pressure recovery model. In this model the pressure increases algebraically over some region of length λ. This length is the distance from the start of the transition zone to the cavity trailing edge as shown in Figure (1-3). The cavity surface can either terminate on the foil or to some height above it. The case where the cavity is not closed at the trailing edge corresponds to a mass flux between the cavity and external flow. The difficulty with this model is that it relies on empirical parameters such as the length λ.

1.3. Modeling Assumptions

At this point it is appropriate to discuss the assumptions which are made in developing the numerical model. They are discussed here for they are fundamental to the model, and influence the goals of the experimental studies. Figure (1-3) shows the model which results from the following simplifications:

- flow is steady and incompressible

- cavitation is limited to a single partial sheet cavity on the suction side of the foil (neglect bubbles, tip cavities, etc.)
- vorticity confined to a thin layer on the foil, cavity and wake surfaces
- pressure at the cavity surface is constant save for a region of length λ near the trailing edge, where it increases algebraically
- no mass flux between cavity and flow
- cavity height is zero at the cavity leading and trailing edges
- cavity length is fixed

This list contains those assumptions which are fundamental to this work. Several assumptions which are less fundamental have been made and are discussed in chapter 2.

1.4. A Brief Research History

This section describes past research efforts for cavitating flows. Of course, as the name of this section implies, this is only a short summary of past work. For a more complete review, the reader is referred to Knapp et al [13] or Wu [25].

The focus of this work is sheet cavities on lifting surfaces. Fundamental to this work is the assumption that the cavity surface is a streamline for the flow. This idea is not exactly new. Kirchoff and Helmholtz studied this problem over a hundred years ago. Using analytical techniques they were able to analyze supercavitating flat plates. In this work it was assumed that the cavities were semi-infinite, which corresponds to a cavitation number of zero. Levi-Civita continued this work by including the effects of curvature of the hydrofoil; however, the requirement of zero cavitation number was not relaxed.

The methods due to Kirchoff, Helmholtz and Levi-Civita, were based on conformal transformations. While these techniques allow one to treat cavities and foils of

arbitrary thickness, they are restricted to rather simple geometries and cannot be extended to treat three dimensional flows. Tulin [21] put forth a linear method based on perturbation techniques. His method allowed for the treatment of more general geometries, and later was extended to cavities with a cavitation number number greater than zero. Guerst [7] introduced a method for partially cavitating foils with finite cavitation number. Common to these linear theories is the assumption that the foil and cavity thicknesses, are much less than the chord length. This results in a simpler dynamic boundary condition on the surface of the foil. A good reference for the formulation of the two-dimensional linear problem, is the text by Newman [20].

The development of methods for the two-dimensional nonlinear problem and the three-dimensional linear and nonlinear problems, have followed one another closely. Leehey [15] introduced a method for supercavitating hydrofoils, based on a strip approximation. Uhlman [22] presented a method for the study of partially cavitating foils in three dimensions. Both these methods were based on linear theories. Uhlman's [23] surface singularity method, allowed for the treatment of fully nonlinear two dimensional partially cavitating hydrofoils. In this case the exact form of the boundary condition on the foil was satisfied. Other methods have been developed for the two dimensional problem, by Lemonnier and Rowe [16], and by Kinnas and Fine [12]. This latter method was extended by Fine to three dimensions [5].

One thing common to all the methods discussed previously is the assumption that the cavity surface is a streamline to the flow. The flow external to the cavity is assumed to be incompressible, and the fluid inside the cavity is taken to be at rest. It is assumed in these models, that in general there is no mass flux through the cavity surface. Note that these assumptions are made to make the problem tractable mathematically. Experimentation has shown that in a gross sense the resulting methods do adequately represent reality. However, these models do not allow one to gain deeper insights into the actual physics and details of the flow. Cavitating flows are highly turbulent, unsteady and

multiphase in nature. To this author's knowledge, few attempts have been made to model the actual complex flow structure. One notable attempt is due to Kato et al [9]. In that work there was no distinction between the cavity and external flow. The two phases were treated as a single viscous fluid of variable density. As they show this flow is inherently rotational, because mechanisms for the generation of vorticity, such as viscosity and baroclinicity of the fluid, are present. One drawback to their method is that it is computationally intensive, since the exact form of the equations of motion and mass conservation are used. It also relies on the specification of a number of parameters which need be obtained empirically.

The tools developed for the analysis of cavitating flows, which are overwhelmingly based on the free streamline model, have to date been adequate in the gross sense. However, we lose a great deal of physics when using the free streamline model. In contrast, the more physical model due to Kato, is too expensive for the current state of the art to be used as a design tools. What is necessary is some bridge between these two extremes, such as boundary layer methods are for the study of viscous fully wetted flow. The author does not want to imply that the present method is such a bridge. The method described herein is essentially a free streamline model, which includes the viscous effects in the form of a boundary layer. As a free streamline model, the same restrictions on mass flux between the cavity and external flow are still imposed. The intent of the present work is to more closely approximate the actual gross characteristics of cavitating flow, such as the experimentally observed thickening of the boundary layer in the wake of the cavity.

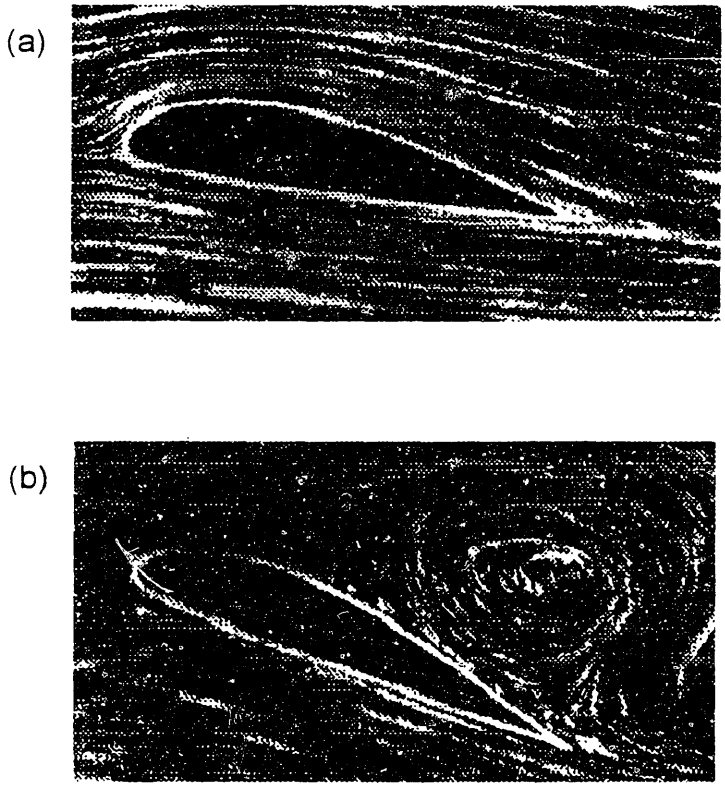

Figure (1-1) (a) Boundary layer without separation. (b) Boundary layer with separation. From Moran [18].

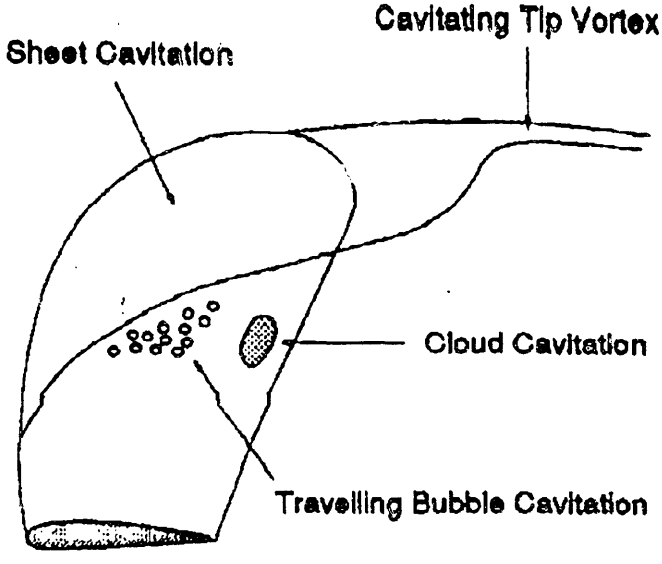

Figure (1-2) Cavitating propeller propeller blade from Fine [5].

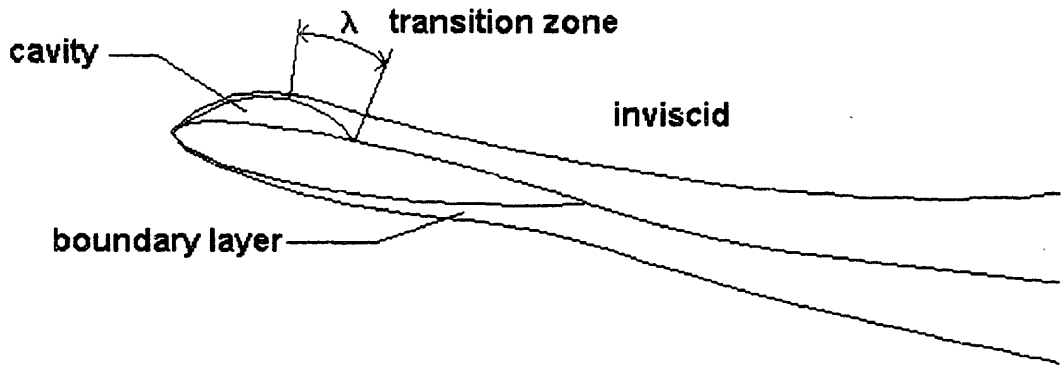

Figure (1-3) Flow schematic showing partial sheet cavity on suction side.

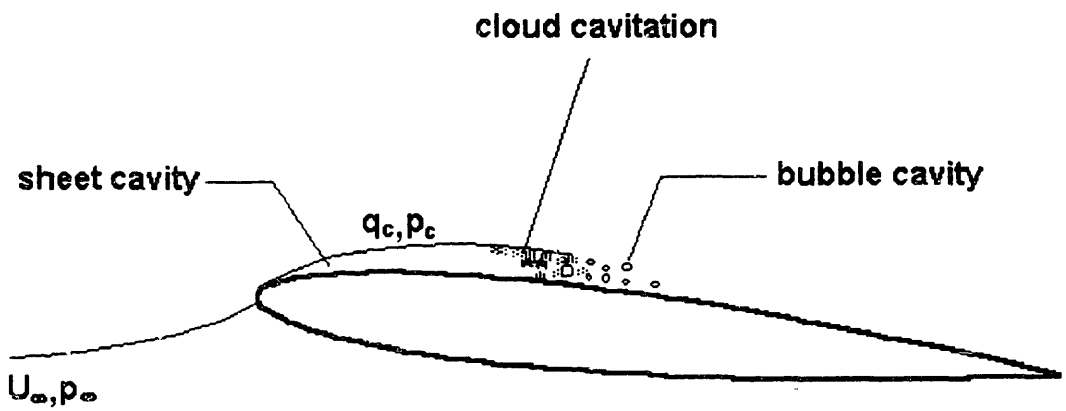

Figure (1-4) Types of cavities.

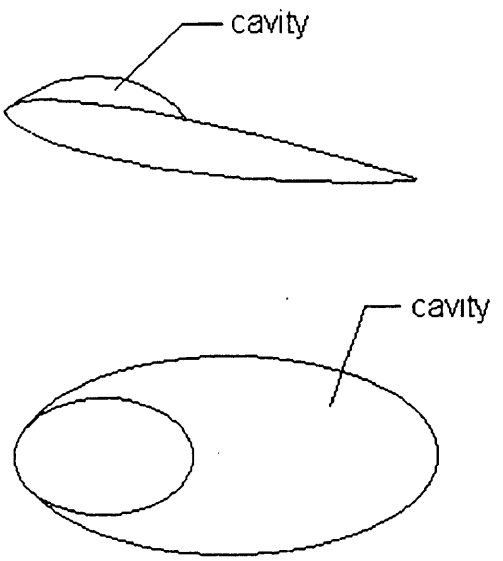

Figure (1-5) A lifting surface and blunt body with cavitation.

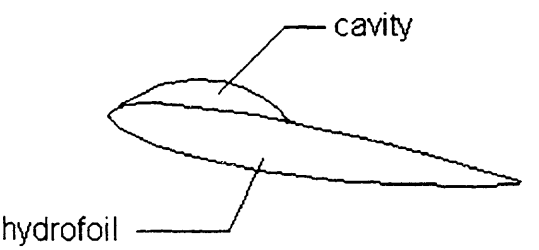

Figure (1-6) A partial cavity formed on the suction side of a hydrofoil.

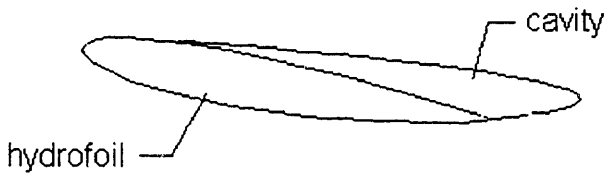

Figure (1-7) A supercavity formed on the suction side of a hydrofoil.

2. Formulation of the Model

In this chapter the method employed in the solution of the flow about two-dimensional partially cavitating lifting sections is discussed. Section 2.1 presents the derivation of the fully wetted inviscid solution method using a perturbation potential formulation. Section 2.2 goes on to describe the transpiration model employed to account for the cavity and viscous boundary layer. The details of the cavity and viscous formulations are discussed in Sections 2.3 and 2.4 respectively.

2.1. Fully Wetted Inviscid Solution

The formulation of the inviscid fully wetted solution method is discussed in this section. It is considered first for it forms the basis for the cavity and viscous models.

The inviscid flow is assumed to be two-dimensional, steady and incompressible. The flow domain is shown in Figure (2-1). The foil is assumed to be subject to a uniform flow $\vec{U}_\infty$. For these conditions the fluid velocity, $\vec{v}$, can be represented by

$$\vec{v} = \vec{U}_\infty + \nabla\phi \tag{2.1}$$

where ϕ, the perturbation potential, satisfies Laplace's equation

$$\nabla^2\phi = 0 \tag{2.2}$$

The term perturbation potential is used for ϕ represents the potential due to that portion of the velocity field which does not include the free stream. This term is somewhat misleading, since, perturbation implies that this portion of the velocity field is much

smaller than the free stream. In actuality, these disturbances can be of the same order as the free stream. But, to be consistent with the literature, this author will use the accepted term. The total potential Φ, which corresponds to (2.1), can be written as

$$\Phi = \Phi_{in} + \phi \tag{2.3}$$

Φ_{in} is the velocity potential for the free stream. For lifting surfaces at an angle of attack α, as shown in Figure (2-2), this potential is given by

$$\Phi_{in} = U_\infty (x\cos\alpha + y\sin\alpha) \tag{2.4}$$

The appropriate kinematic boundary conditions are

$$\partial\phi/\partial n = -\bar{U}_\infty \cdot \bar{n} \quad \text{on the body} \tag{2.5}$$

and

$$\nabla\phi \to 0 \quad \text{at infinity} \tag{2.6}$$

where, $\bar{n}$, is the surface normal for the foil, defined as shown in Figure (2-1). For lifting surfaces the Kutta condition

$$\nabla\phi = finite; \quad \text{at the trailing edge} \tag{2.7}$$

must be imposed.

When solving the inviscid problem, it is only necessary to solve for the perturbation potential on the body. The reason for this is that most quantities of interest, such as the velocity and pressure distributions on the body, as well as in the flow field, can be obtained from it quite easily. In light of this, Green's theorem can be applied at some point p on the foil surface, and the perturbation potential at that point is then given by

$$\pi\phi_p = \oint_{S_b}\left[\frac{\partial\phi}{\partial n}G - \phi\frac{\partial G}{\partial n}\right]dS - \int_{S_w}\Delta\phi_w\frac{\partial G}{\partial n}dS \tag{2.8}$$

Equation (2.8) is a solution to Laplace's equation for the perturbation potential, and it satisfies the boundary conditions (2.5) and (2.6). G is the infinite domain two-dimensional Green's function. It is defined in terms of the distance R between point p and the element dS as

$$G = \ln R \tag{2.9}$$

The first and second terms on the right hand side of equation (2.8) represent source and normal dipole distributions on the body S_b with strengths $\frac{\partial \phi}{\partial n}$ and ϕ, respectively. The source strengths are known from the kinematic boundary condition (2.5); but, the dipole strengths are unknown and must be solved for. The third term in equation (2.8) represents a dipole distribution on the wake surface S_w of constant strength $\Delta\phi_w$, which is equal to Γ, the circulation about the body.

The perturbation potential on the body can now be obtained by solving (2.8) in place of Laplace's equation. Note that the integrals in (2.8) are over the body and wake surfaces only. For the numerical solution one approximates the solution by making the following assumptions First the body is discretized and ϕ is solved for at a discrete number of points In this formulation, the body is represented in terms of N line segments or panels as shown in Figure (2-2). The perturbation potential and source strengths, are assumed to be constant over each of these segments. On each panel the point p at which ϕ is solved for, the control point, is taken to be the panel mid-point. The wake is assumed to lie on the x axis as shown in Figure (2-2). For the inviscid solution the wake need not be discretized, since the wake dipole is of constant strength and so can be represented by a single vortex at the trailing edge of the foil.. Based on these assumptions, equation (2.8) can now be written in discrete form for the perturbation potential on the i^{th} panel as

$$\phi_i = \sum_{j=1}^{N} B_{ij} \frac{\partial \phi_j}{\partial n} - \sum_{j=1}^{N} \tilde{S}_{ij} \phi_j - \Delta\phi_w W_i \tag{2.10}$$

where,

$$\tilde{S}_{ij} = \int_{S_j} \frac{\partial G_{ij}}{\partial n} dS \tag{2.11}$$

$$B_{ij} = \int_{S_j} G_{ij} dS \tag{2.12}$$

$$W_i = \int_{S_w} \frac{\partial G_i}{\partial n} dS \tag{2.13}$$

The Kutta condition can be shown [19] to be satisfied when the circulation, and therefore $\Delta\phi_w$, is given by

$$\Delta\phi_w = \phi_N - \phi_1 \tag{2.14}$$

where ϕ_N and ϕ_1 are the potentials at the upper and lower trailing edge panels, respectively. If one defines the influence coefficient A_{ij}

$$A_{ij} = \delta_{ij}\pi + \delta_{iN}W_N - \delta_{i1}W_1 + \tilde{S}_{ij} \tag{2.15}$$

the discrete form of Green's theorem can then be written as

$$\sum_{j=1}^{N} A_{ij}\phi_j = \sum_{j=1}^{N} B_{ij}\frac{\partial\phi_j}{\partial n} \tag{2.16}$$

Inverting A_{ij} in the above equation gives the following expression for the inviscid perturbation potential

$$\phi_i^{inv} = \sum_{k=1}^{N} A_{ik}^{-1}\left(\sum_{j=1}^{N} B_{kj}\frac{\partial\phi_j}{\partial n}\right) \tag{2.17}$$

Given the foil geometry and angle of attack, one can calculate the influence coefficients A_{ij} and B_{ij}, and the velocity normal to the body $\frac{\partial\phi_j}{\partial n}$. Equation (2.17) can then be used to obtain the N perturbation potentials ϕ_j^{inv} on the body.

2.2. Blowing Source Model

In the inviscid problem the body surface is coincident with streamlines of the free stream. However, for cavitating or viscous flows, the bounding streamline is effectively displaced from the body surface as shown in Figure (2-3). This displacement of the streamlines gives rise to the well-known concept of the displacement thickness δ^* for viscous flows, and the lesser known cavity height h for cavitating flows. One can account for this displacement of the streamlines in a similar manner as one accounts for the thickness of the foil, by adding sources on the body surface.

This method of adding sources on the body surface itself was used by Hufford [8] for viscous boundary layers in the code PAN2D-BL. Note that if one is to be rigorous, the sources should be placed at the edge of the boundary layer as given by the

displacement thickness, instead of on the foil. This introduces many complications, for the location of the edge of the boundary layer is unknown, and must be determined as part of the solution. However, placement of these sources on the foil, introduces relatively small errors in the solution.

The sources which are used to model the boundary layer and cavity are termed blowing sources. Blowing sources act as do the sources which model foil thickness for inviscid flows. The difference now is that the strength of these sources is unknown, and must be determined as part of the solution. Hufford [8] has shown that when viscous blowing sources of strength σ^v are included, the equation for perturbation potential (2.17) must be modified as follows

$$\sum_{j=1}^{N} A_{ij}\phi_j = \sum_{j=1}^{N} B_{ij}\frac{\partial \phi_j}{\partial n} + \sum_{j=1}^{N+N_w} V_{ij}\sigma_j^v \tag{2.18}$$

A further modification is required when the flow is cavitating. The resulting equation is

$$\sum_{j=1}^{N} A_{ij}\phi_j = \sum_{j=1}^{N} B_{ij}\frac{\partial \phi_j}{\partial n} - \sum_{j=1}^{N+N_w} V_{ij}\sigma_j^v + \sum_{k=1}^{N_c} C_{ik}\sigma_k^c \tag{2.19}$$

where,

$$C_{ik} = \int_{S_k} G_{ik}\,dS \tag{2.20}$$

$$V_{ij} = \int_{S_j} G_{ij}\,dS \tag{2.21}$$

The additional terms are due to the blowing sources for the viscous boundary layer and the cavity, respectively. The blowing sources for the cavity are again placed on the foil surface. This is not strictly correct, though the errors due to this approximation are small, as demonstrated by Kinnas and Fine [12]. Note that the $N + N_w$ viscous sources of strength σ_j^v are distributed not only over the body surface, but also over the wake surface as shown in Figure (2-4). For this work the wake has been represented by N_w panels which are stretched exponentially with distance from the trailing edge of the foil. The N_c cavity sources of strength σ_j^c are located on those panels which correspond to the body surface beneath the cavity as shown in Figure (2-4).

As was done in the previous section, A_{ij} can be inverted in (2.19) to give the following expression for the perturbation potential

$$\phi_i = \phi_i^{imv} + \sum_{l=1}^{N} A_{il}^{-1}\left(\sum_{j=1}^{N+N_w} V_{lj}\sigma_j^v\right) + \sum_{m=1}^{N} A_{im}^{-1}\left(\sum_{k=1}^{N_c} C_{mk}\sigma_k^c\right) \tag{2.22}$$

where ϕ_i^{imv} is given by equation (2.17). Equation (2.22) can be written more concisely if one defines the following influence coefficients

$$\tilde{V}_{ij} = \sum_{l=1}^{N} A_{il}^{-1} V_{lj} \tag{2.23}$$

$$\tilde{C}_{ik} = \sum_{m=1}^{N} A_{im}^{-1} C_{mk} \tag{2.24}$$

Adding the free stream potential to equation (2.22) gives the following equation for the total potential

$$\Phi_i = (\Phi_{in})_i - \phi_i^{imv} + \sum_{j=1}^{N+N_w} \tilde{V}_{ij}\sigma_j^v + \sum_{k=1}^{N_c} \tilde{C}_{ik}\sigma_k^c \tag{2.25}$$

Equation (2.25) serves to couple the inviscid, viscous and cavity models. To complete this coupling, one needs to relate σ_j^v to the boundary layer variables and σ_j^c to the cavity variables. Moran [18] shows that this relation for viscous sources is given by

$$\sigma_j^v = d(U_e\delta^*)/ds \tag{2.26}$$

where, U_e is the edge velocity and s is the arc length measured along the foil surface. In a similar manner, the cavity source strengths can be related to the cavity variables by

$$\sigma_j^c = d(U_e h)/ds \tag{2.27}$$

Mass defects due to the boundary layer and cavity are given by

$$m^v = U_e\delta^* \tag{2.28}$$

and

$$m^c = U_e h \tag{2.29}$$

respectively. These defects are defined at the panel nodes, as are U_e, h and δ^*. In contrast, the blowing source strengths are defined at the panel control points. The derivatives above are approximated using the following difference formulas

$$\sigma_j^v = (m_{i_n-1}^v - m_{i_n}^v)/(s_{i_n-1} - s_{i_n}) \tag{2.30}$$

$$\sigma_k^v = (m_{i_n-1}^c - m_{i_n}^c)/(s_{i_n-1} - s_{i_n}) \tag{2.31}$$

The indices i_n, j and k are defined as shown in Figure (2-4). The relation between i_n and j is simply

$$i_n = j \tag{2.32}$$

The relation between i_n and k is slightly more complicated. This relationship is given by

$$i_n = k + N/2 + N_{BC} \tag{2.33}$$

where N_{BC} is the number of panels between the foil leading edge and the start of the cavity.

By replacing the blowing source strengths in equation (2.25) with the expressions (2.30) and (2.31), the equation for the total potential can be expressed in terms of the mass defects as

$$\Phi_i = (\Phi_{in})_i + \phi_i^{inv} + \sum_{j=1}^{N+N_w-1} \tilde{V}_{ij}' m_j^v + \sum_{k=1}^{N_c-1} \tilde{C}_{ik}' m_k^c \tag{2.34}$$

where the influence coefficients $\tilde{V}_{ij}'$ and $\tilde{C}_{ik}'$ are given in terms of the arc lengths s_{i_n} and the influence coefficients $\tilde{V}_{ij}$ and $\tilde{C}_{ik}$.

The displacement thickness and cavity height are determined from their respective models; however, one needs an expression for the edge velocity which is defined as

$$U_e = \partial\Phi/\partial s \tag{2.35}$$

The potentials are defined at the panel midpoints, while the edge velocities are defined at the panel nodes. Using a difference formula, one can express the edge velocity at some node j in terms of the values of Φ and s at the control points directly preceding and following it as

$$(U_e)_i = (\Phi_{i+1} - \Phi_i)/(s_{i+1} - s_i) \tag{2.36}$$

Substituting the expression of equation (2.34) for Φ gives

$$(U_e)_i = (U^{inv})_i + \sum_{j=1}^{N+N_w-1} D_{ij}^v m_j^v + \sum_{k=1}^{N_c-1} D_{ik}^c m_k^c \tag{2.37}$$

where, the influence coefficients D_{ij}^v and D_{ik}^c are defined in terms of $\tilde{V}_{ij}'$ and $\tilde{C}_{ik}'$ and the arc lengths s_{i_n}. U^{inv} is the velocity tangent to the body for inviscid flow as defined by

$$\left(U^{imv}\right)_i = \left[\left((\Phi_{in})_{i-1} - \phi_{i-1}^{imv}\right) - \left((\Phi_{in})_i + \phi_i^{imv}\right)\right] / \left[s_{i-1} - s_i\right] \tag{2.38}$$

Equation (2.37) is the actual mechanism for coupling the inviscid, viscous and cavity models. This is so for knowledge of the edge velocity is required when solving the viscous and cavity problem, as is shown in sections 2.3 and 2.4.

2.3. Dynamic Boundary Condition on the Cavity

This section treats the formulation of the cavity model. It is assumed in this formulation that cavitation is limited to one partial sheet cavity on the suction side of the foil. The cavity detachment point is taken to be known. Cavity length l, which is the distance from the detachment point to the cavity trailing edge, is also assumed known. Note that this formulation can be used for both inviscid and viscous flows.

For this work the cavity is treated as two separate zones, as shown in Figure (2-5). The first is a constant pressure zone between A and B, at pressure p_c. This is followed by a transition zone of length λ between points B and C. The pressure in the transition zone increases from the minimum value p_c at B, to some maximum value at C. This is known as a pressure recovery termination model.

Instead of working directly with pressure, it is more convenient to use cavity velocity for this formulation. One can then recover the cavity pressure from Bernoulli's equation

$$p_\infty + \tfrac{1}{2}\rho U_\infty^2 = p_c(s_c) + \tfrac{1}{2}\rho q_c^2(s_c) \tag{2.39}$$

where p_∞ is the free stream pressure. Both cavity pressure and velocity are defined in terms of cavity arc length s_c, which is measured along the foil underneath the cavity starting at the detachment point. The cavity velocity is given by

$$q_c(s_c) = q_c\left[1 - F(s_c)\right] + U^{cte}F(s_c) \tag{2.40}$$

where U^{cte} is the edge velocity at the cavity trailing edge, and q_c is a constant defined as

$$q_c = U_\tau \sqrt{1+\sigma} \tag{2.41}$$

The cavitation number, σ, is defined in terms of cavity pressure as

$$\sigma = (p_\infty - p_c)/\tfrac{1}{2}\rho U_\infty^2 \tag{2.42}$$

$F(s_c)$ is given by

$$F(s_c) = \begin{cases} 0 & s_c \le s_\lambda \\ \left[\frac{s_c - s_\lambda}{\lambda}\right]^v & s_\lambda \le s_c \le l \end{cases} \tag{2.43}$$

where s_λ, the cavity arc length at the beginning of the transition zone, is defined as

$$s_\lambda = l - \lambda \tag{2.44}$$

This model was used by Kinnas and Fine [12].

The cavity is discretized as shown in Figure (2-6), with one cavity height being defined at each cavity panel node. Cavity height is defined as the distance from the body, along the local body normal, to the cavity surface. At each of these nodes the edge velocity must equal the cavity velocity. This condition can be expressed by combining equations (2.37) and (2.40) to get

$$q_c[1 - F(s_c)] + U^{cte} F(s_c) = \left(U^{imv}\right)_i + \sum_{j=1}^{N+N_w+1} D_{ij}^v m_j^v + \sum_{j=1}^{N_c+1} D_{ij}^c m_j^c \tag{2.45}$$

This equation, which must be satisfied at each of the $N_c + 1$ cavity nodes, involves the $N_c + 1$ unknown mass defects m^c, and the unknown velocities U^{cte} and q_c. Thus, there are two more unknowns than equations. This is resolved by taking the cavity mass defects at the cavity leading and trailing edges to be given by

$$m_1^c = 0 \tag{2.46}$$

$$m_{N_c+1}^c = M_{cte} \tag{2.47}$$

The condition of zero mass defect at the cavity leading edge corresponds to the cavity being attached to the surface of the foil. The second condition corresponds to a mass flux between the cavity and external flow of strength M_{cte}. When this mass flux is zero the cavity reattaches to the foil.

In the case of inviscid flow the viscous blowing sources are zero. Equation (2.45) for this case is

$$q_c\left[1-F(s_c)\right]+U^{cte}F(s_c)-\sum_{k=1}^{N_c+1}D_{ik}^{c}m_k^{c}=\left(U^{inv}\right)_i \tag{2.48}$$

First the fully wetted inviscid problem is solved. Then the inviscid velocity on the body, U^{inv}, is calculated at the cavity nodes. Finally, equation (2.48) is applied at the cavity nodes, and that set of equations is solved to get q_c, U^{cte}, and the mass defects. The cavity heights can then be calculated from

$$h=m^c/q_c(s_c) \tag{2.49}$$

Matters are more complicated when the flow is viscous for the blowing source strengths σ_j^v, are non-trivial and must be evaluated as part of the boundary layer solution. The viscous model, which is discussed in the next section, must then be used to provide the additional information. The solution method for this case is discussed in Chapter 3.

2.4. Viscous Formulation

The viscous model used for this research is taken from Drela [3]. A summary of his formulation is contained in this section. The reader is referred to [3] for more details about the model.

The flow is assumed to be steady and incompressible, and viscous effects are confined to a thin layer near the foil, cavity and wake surfaces. For these conditions the standard momentum integral equation is appropriate

$$\frac{d\theta}{ds}+(2+H)\frac{\theta}{U_e}\frac{dU_e}{ds}=C_f/2 \tag{2.50}$$

The so-called kinetic energy shape equation is also used

$$\theta\frac{dH^*}{ds}+\left[2H^{**}+H^*(1-H)\right]\frac{\theta}{U_e}\frac{dU_e}{ds}=2C_D-H^*\frac{C_f}{2} \tag{2.51}$$

A third equation is also necessary; however, this equation is different for laminar and turbulent flows. When the flow regime is laminar, this equation is the rate equation for the amplitude of Tollmien-Schlichting waves

$$\frac{d\tilde{n}}{ds} = \frac{d\tilde{n}}{dR_{e\theta}} \frac{dR_{e\theta}}{ds} \tag{2.52}$$

This equation is used until $\tilde{n}$ reaches some specified critical value, $\tilde{n}_{crit}$. This is referred to as an $e^{\tilde{n}_{crit}}$ transition model. Once this point is reached, the flow is considered turbulent. Equation (2.52) is then replaced by the shear stress lag equation

$$\frac{\delta}{C_\tau}\frac{dC_\tau}{ds} = 5.6\left(C_{\tau eq} - C_\tau\right) + 2\delta\left\{\frac{4}{3\delta^*}\left[\frac{C_f}{2} - \left(\frac{H_k - 1}{6.7H_k}\right)^2\right] - \frac{1}{U_e}\frac{dU_e}{ds}\right\} \tag{2.53}$$

Equations (2.50) through (2.53) contain many variables which are represented by rather complex functions. The reader is referred to [4] for these functional forms. In this paper only the primary variables will be considered. For turbulent flows these are θ, δ^*, U_e and C_τ. When the flow is laminar $\tilde{n}$ is used in place of C_τ. The number of independent variables can be reduced to three by considering the mass defect m^* in place of δ^* and U_e, and by calculating the edge velocity where necessary using (2.37).

The no-flux and no-slip boundary conditions are applied on the foil surface. On the wake surface the shear stress, and therefore C_f, are taken to be zero. This last constraint on the shear stress, also needs to be imposed on the cavity surface.

The blowing sources for the boundary layer are located at the panel control points as shown in Figure (2-4). The boundary layer variables are defined at each panel node. Note that in the wake, the boundary layer variables are assumed to be the sum of the upper and lower side variables. Equations (2.50), (2.51), (2.52) and (2.53) are approximated using central differences. At each node there are then three equations and three unknowns.

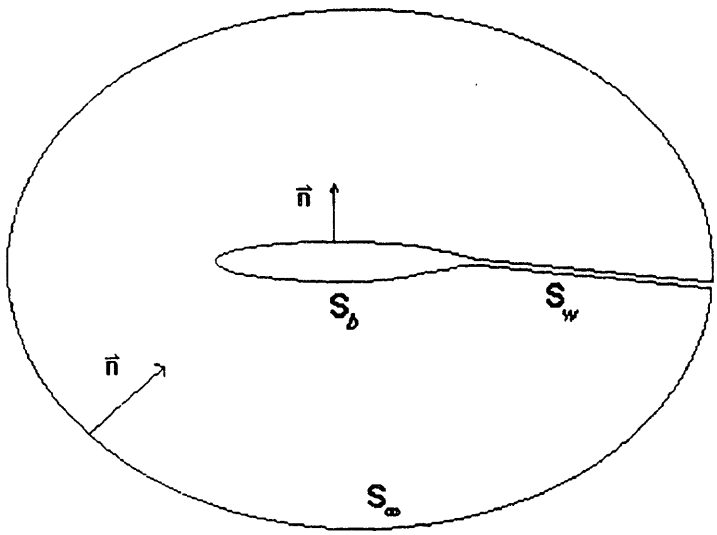

Figure (2-1) Inviscid flow domain.

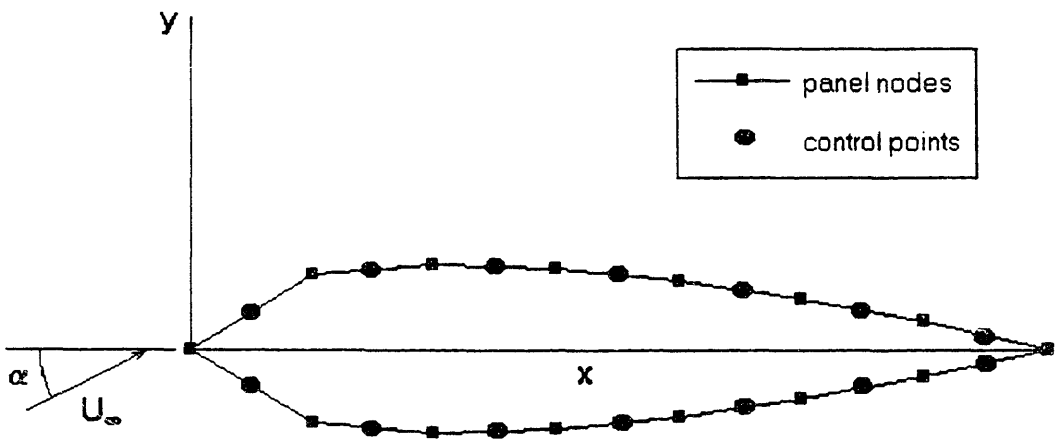

Figure (2-2) Discretization for inviscid fully wetted flow.

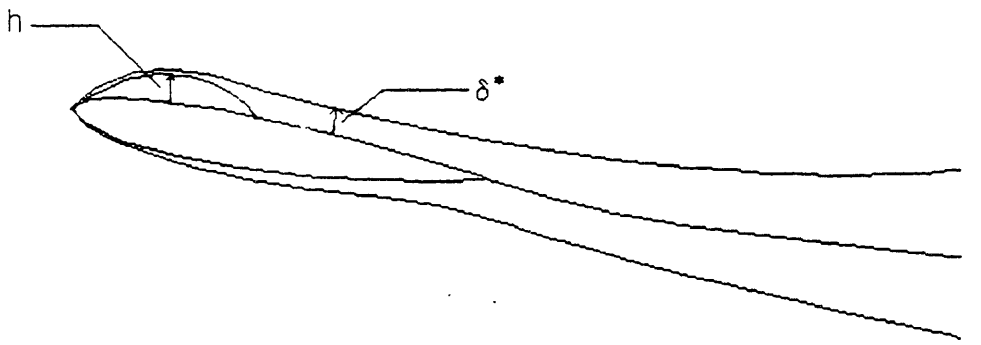

Figure (2-3) Displacement of streamlines for viscous cavitating flow.

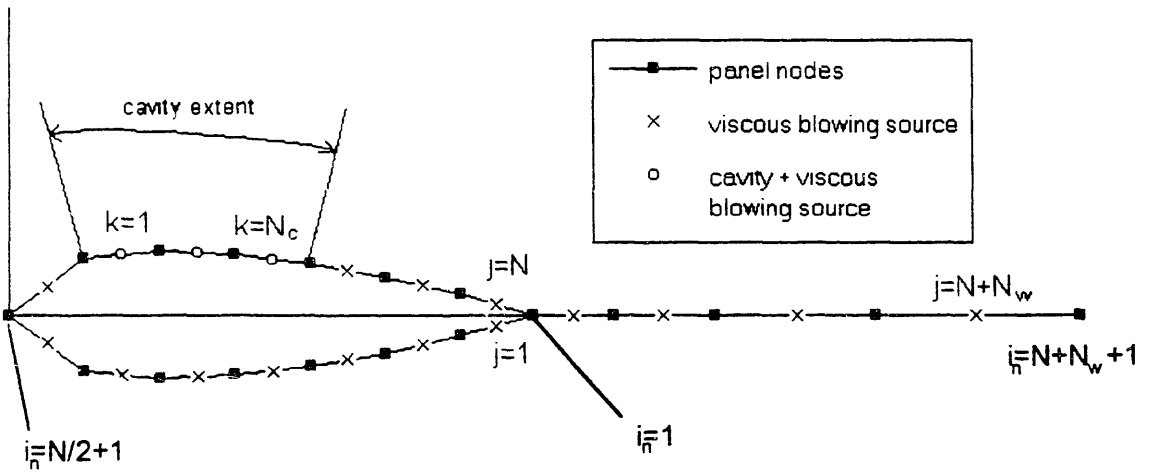

Figure (2-4) Paneling and blowing source placement for viscous cavitating flow.

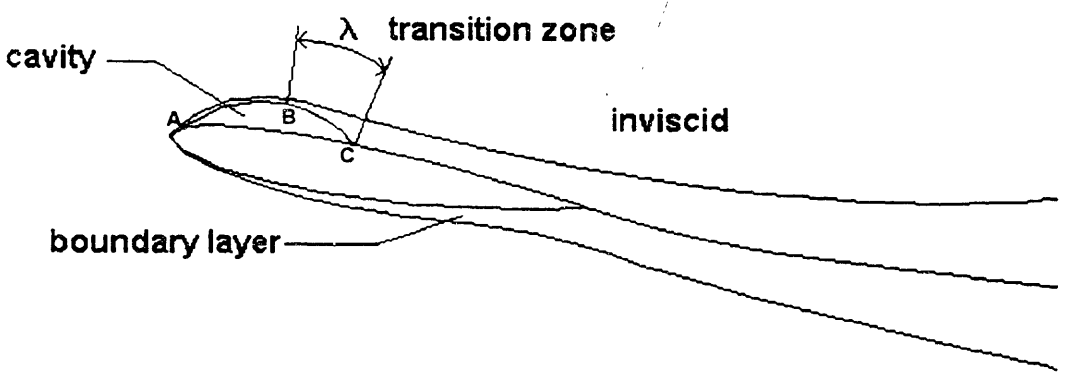

Figure (2-5) Flow model showing cavity transition zone.

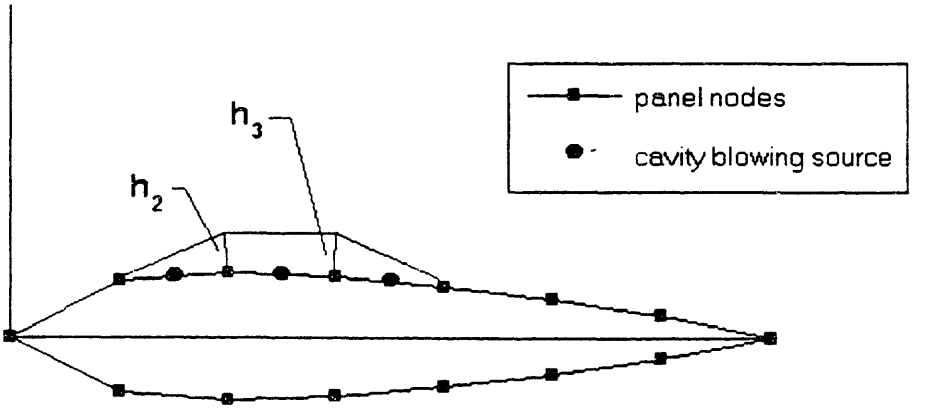

Figure (2-6) Cavity discretization for $N_c = 3$. Note that cavity heights are taken to be zero at the cavity leading and trailing edges.

3. P2D-BLWC: A Numerical Code for Viscous Flows with Cavitation

This chapter describes the implementation of the method from Chapter 2 in the form of the computer code P2D-BLWC. This code is based on PAN2D-BL, which is discussed in Hufford [8]. PAN2D-BL can be used to analyze **2D** viscous **B**oundary **L**ayers about lifting surfaces. P2D-BLWC can be used to analyze partially **C**avitating hydrofoils including the effects of **2D B**oundary **L**ayers. The solution procedure including Jacobian iteration is discussed in Section 3.1. Note that the formulation detailed in Chapter 2, can only be used for foils in unbounded flow. Section 3.2 of this chapter, describes how the method can be employed for the analysis of bounded flows via the method of images. This allows for one to deal with **W**all effects. Section 3.3 details the convergence results for P2D-BLWC. Validation of the code for fully-wetted viscous flows and partially cavitating inviscid flows is discussed in sections 3.4 and 3.5, respectively.

3.1. Implementation of the Method

In this section the actual implementation of the method outlined in Chapter 2 is discussed. The code which resulted from this implementation is P2D-BLWC. It is based on the code PAN2D-BL, which was extended to allow for the analysis of 2D partially cavitating hydrofoils, including such real fluid effects as viscosity, turbulence and separation. P2D-BLWC can also be used for flows which are bound by two parallel horizontal walls as

described in section 3.2. This feature was added so that the code results could be compared with those from experiments in a tunnel.

The viscous solver used in both PAN2D-BL and P2D-BLWC is the same that is used in XFOIL [8]. This solver takes as its input the inviscid velocity distribution on the body, along with geometry information. Using a Newton technique it iteratively solves the system of equations formed by differencing equations (2.50), (2.51), (2.52) and (2.53). The independent variables used in the boundary layer solver are m_i^v, θ_i and either $\tilde{n}_i$ or α_{T_i}. When solving the nonlinear set of equations using a Newton technique, it is necessary to define perturbations to the boundary layer variables. The perturbations to the boundary layer variables for viscous node j in the Newton scheme are δm_i^v, $\delta\theta_i$ and either $\delta\tilde{n}_i$ or $\delta\alpha_{T_i}$. The associated Newton system is

$$\left[J_{ij}^v\right]\begin{Bmatrix}\delta\theta_j\\ \delta m_j^v\\ \delta\tilde{n}_j \text{ or } \delta\alpha_{T_j}\end{Bmatrix}=\left\{-R_i^v\right\}\quad 1\le i\le N+N_w \tag{3.1}$$

where, J_{ij}^v and R_i^v are the respectively the viscous Jacobian and its residual as defined in [8]. Once the viscous mass defects are known, the edge velocity is calculated using

$$(U_e)_i=\left(U^{inv}\right)_i+\sum_{j=1}^{N+N_w-1}D_{ij}^v m_j^v+\sum_{j=1}^{N_c-1}D_{ij}^c m_j^c \tag{3.2}$$

However, the cavity mass defects, m_j^c, are unknown and must be determined.

In solving the viscous cavity problem, one could conceivably modify the Jacobian system (3.1) to account for the presence of the cavity. However, in this work a double Newton iteration is used instead. Figure (3-1) shows a flowchart of the method. The first step is the solution of the fully wetted inviscid problem. The inviscid velocity U^{inv} on the body and wake are calculated as part of this solution. The next step is to solve the cavity

problem in the absence of viscous blowing sources. This was discussed in section 2.3. The set of equations (2.48), assuming that the mass flux at the cavity trailing edge M_{cte} is zero, can be written in matrix form as

$$\begin{bmatrix} 1-F_1 & -D^c_{1,2} & \cdots & -D^c_{1,N_c} & F_1 \\ 1-F_2 & -D^c_{2,2} & \cdots & -D^c_{2,N_c} & F_2 \\ \vdots & \vdots & \ddots & \vdots & \vdots \\ \vdots & -D^c_{N_c-1,2} & \cdots & -D^c_{N_c-1,N_c} & \vdots \\ 1-F_{N_c+1} & -D^c_{N_c+1,2} & \cdots & -D^c_{N_c+1,N_c} & F_{N_c+1} \end{bmatrix} \begin{pmatrix} q_c \\ m^c_2 \\ \vdots \\ m^c_{N_c} \\ U^{cte} \end{pmatrix} = \begin{pmatrix} U^{inv}_{1-N_c+2-N_{BC}} \\ U^{inv}_{2-N_c+2-N_{BC}} \\ \vdots \\ U^{inv}_{N_c+1-N_c+2-N_{BC}} \end{pmatrix} \tag{3.3}$$

where

$$F_i = F(s_{c_i}) \tag{3.4}$$

Equation (3.3) can be written more compactly using matrix notation

$$\underline{A}\,\underline{x} = \underline{U}^{inv} \tag{3.5}$$

where, $\underline{A}$ is the matrix on the left hand side of (3.3) and $\underline{x}$ is the solution vector. $\underline{U}^{inv}$ is the edge velocity vector for fully wetted inviscid flow. The inviscid cavity solution, which is the zeroth iteration for the main Newton iteration, is given by

$$\underline{x}^0 = \underline{A}^{-1}\,\underline{U}^{inv} \tag{3.6}$$

The inviscid cavity velocity distribution for the zeroth iteration is then computed using

$$\left(U^{cav}\right)^0_i = \left(U^{inv}\right)_i + \sum_{j=2}^{N_c} D^c_{ij}\left(m^c_j\right)^0 \tag{3.7}$$

This distribution is then sent to the boundary layer solver, which calculates m^v_j, θ, and C_τ or $\tilde{n}$ for the zeroth iteration. The edge velocity can then be calculated from

$$\left(U_e\right)^0_i = \left(U^{cav}\right)^0_i + \sum_{j=1}^{N+N_w-1} D^v_{nj}\left(m^v_j\right)^0 \tag{3.8}$$

Remember that the inviscid cavity velocity includes the fully wetted inviscid velocity contribution along with the cavity contribution, so equation (3.2) need not be used for the

edge velocity calculation. The driving Newton iteration comes into play by requiring that the edge velocity equal the cavity velocity distribution at the cavity nodes

$$(q_e)_i^t = (U_e)_{i+N_2-N_{BC}}^t \qquad 1 \le i \le N_c + 1 \tag{3.9}$$

The variable t above denotes iteration number, and N_{BC} is the number of panels between the foil leading edge and the start of the cavity (see section 2.2). In general this requirement for the edge velocity is not satisfied. It is necessary to define a residual at each cavity node for the current iteration as

$$R_i^c = (q_e)_i^t - (U_e)_{i+N_2-N_{BC}}^t \qquad 1 \le i \le N_c + 1 \tag{3.10}$$

When this residual is greater than some specified tolerance, it is necessary to perturb the cavity solution and recompute the boundary layer solution based on a new inviscid cavity velocity. The perturbations to the cavity variables are defined as follows

$$q_c^{t+1} = q_c^t + \delta q_c^t \tag{3.11}$$

$$(U^{cte})^{t+1} = (U^{cte})^t + (\delta U^{cte})^t \tag{3.12}$$

and

$$(m_i^c)^{t+1} = (m_i^c)^t + (\delta m_i^c)^t \qquad 2 \le i \le N_c \tag{3.13}$$

The inviscid cavity velocity for the next iteration is given by

$$(U^{cav})_i^{t+1} = (U^{cav})_i^t + \sum_{j=2}^{N_c} D_{ij}^c (\delta m_j^c)^t \tag{3.14}$$

It only remains to show how the perturbations to the solution are computed. The perturbation vector for the solution is defined as

$$\underline{x}^{t+1} = \underline{x}^t + \underline{\delta x}^t \tag{3.15}$$

The cavity residuals, given by equation (3.10), can be written as a vector in terms of $\underline{x}^t$, $\underline{U}^{inv}$ and $(\underline{m}^v)^t$ and $\underline{D}^v$ as

$$(\underline{R}^c)^t = \underline{A}\,\underline{x}^t - \underline{U}^{inv} - \underline{D}^v (\underline{m}^v)^t \tag{3.16}$$

where, equation (3.2) was used in substitution for $(U_e)_i$. The perturbation is found from the following expression

$$\underline{J}^c \underline{\delta x}^t = -\left(\underline{R}^c\right)^t \tag{3.17}$$

where, the cavity Jacobian, $\underline{J}^c$,is defined as

$$\underline{J}^c = \frac{\partial \underline{R}^{c\,t}}{\partial \underline{x}^c} \tag{3.18}$$

Taking the derivative of (3.16) with respect to the solution vector gives

$$\underline{J}^c = \underline{A} - \frac{\partial}{\partial \underline{x}^c}\left(\underline{D}^v\left(\underline{m}^v\right)^t\right) \tag{3.19}$$

In the present work it is assumed that the viscous contribution to the edge velocity varies slowly with respect to the cavity solution. Mathematically this can be written

$$|\underline{A}| >> \left|\frac{d}{d\underline{x}^c}\left(\underline{D}^v\left(\underline{m}^v\right)^t\right)\right| \tag{3.20}$$

which results in the following simple expression for the Jacobian

$$\underline{J}^c \cong \underline{A} \tag{3.21}$$

The double Newton iteration just described, has been successfully implemented in P2D-BLWC. Results from convergence tests of the code are described in Section 3.3. Validation of the code, that is comparing it with existing codes, was possible for the cases of viscous fully wetted flow and inviscid cavity flow. The codes XFOIL and PCPAN were used for this purpose. However, no 2D boundary layer codes exist which can be used to compare the viscous cavitating flow results. In this case another method of validation is used as discussed in Section 3.6.

3.2. Modeling Wall Effects Via the Method of Images

The formulation described in chapter 2 requires that the flow domain be infinite in extent. In reality this condition may not be met. Such a situation is encountered when testing foils in a water tunnel. It is then necessary to include the effects of the tunnel walls on the flow.

Consider the experimental configuration described in chapter 4. The foil is bound between two horizontal walls as shown in Figure (3-2). One can model this by using two walls of infinite extent as shown in Figure (3-3). The foil is mounted in the tunnel at some angle of attack. The flow at infinity is assumed to be uniform. If viscous effects on the walls are neglected, it is then only necessary to satisfy the kinematic boundary condition on the walls. The question now becomes, how does one modify the formulation of Chapter 2 in such a way as to satisfy the no flux condition at the walls? One solution to this question, and by no small coincidence the one chosen here, is by using the method of images. What follows is a brief overview on the method of images, and how this method can be applied to the problem at hand.

Consider the point source of strength Γ, located at *(0,h)*, as shown in Figure (3-4). The method of images tells us that the velocity potential for this configuration, ϕ_{s1w}, can be expressed as

$$\phi_{s1w} = \phi_{S\infty}(0,h) + \phi_{SIMG}(x_i, y_i) \tag{3.22}$$

where, $\phi_{S\infty}(x_s, y_s)$, is the potential for a source at *(0,h)* in the absence of the wall, and $\phi_{SIMG}(x_i, y_i)$, the potential due to some image located at (x_i, y_i). The image potential is nothing more than the potential due to a source of the same strength placed at *(0,-h)*, as shown in Figure (3-4). So the final expression for ϕ_{s1w} is

$$\phi_{s1w} = \phi_{S\infty}(0,h) + \phi_{S\infty}(0,-h) \tag{3.23}$$

The proof for this result will not be presented here, the reader is referred to the text by Newman [20] or any introductory text on fluids.

When a second wall is added, the problem becomes a bit more complicated. Figure (3-5) shows such a case. The centerline of the tunnel is taken to be the horizontal axis. The distance from the centerline to the tunnel wall is t. A point source of strength Γ, is located at (x,Δ). In the case of one wall it was only necessary to use a single image. Adding a second requires an infinite number of images placed as shown in Figure (3-5). However, as in the case of one wall, each of these images is nothing more than a source of the same strength as the original. The potential due to a source between two walls, ϕ_{s2w}, is given by

$$\phi_{s2w} = \phi_{S\tau}(x,\Delta) + \sum_{i=1}^{\infty}\left[\phi_{S\tau}\left(x, iH + (-1)^i\Delta\right) + \phi_{S\infty}\left(x, iH - (-1)^i\Delta\right)\right] \tag{3.24}$$

where,

$$H = 2t \tag{3.25}$$

The next and last case considered here, is shown in Figure (3-6). In this case the potential is assumed to be due to a distribution of constant strength sources or dipoles of over a panel, as shown in Figure (3-6). This case is of particular interest, because in Chapter 2 the fundamental assumption was that the inviscid flow can be modeled by a number of panels with constant strength source and dipole distributions over them. Consider the panel of Figure (3-6), with a constant source distribution over it. The potential at some point i, due to this panel which shall be referred to as j, was shown to be

$$\tilde{S}_{ij} = \int_{S_j} \frac{\partial G_{ij}}{\partial n} dS \tag{3.26}$$

This result is only correct when the domain is unbounded. When walls are included it is necessary to use images so that the kinematic boundary condition at the wall may be satisfied. As in the case of a point source between two walls, an infinite number of sources are needed, placed as shown in Figure (3-6). The potential can be written

$$\left(\tilde{S}_{ij}\right)_{2w} = \tilde{S}_{ij} + \sum_{k=1}^{\infty}\left[\tilde{S}^{J}_{i,-k} + \tilde{S}^{J}_{i,-k}\right] \tag{3.27}$$

where,

$$\tilde{S}^{J}_{i,+k} = \int_{S^{J}_{+k}} \frac{\partial G_{i,+k}}{\partial n} dS \tag{3.28}$$

$$\tilde{S}^{J}_{i,-k} = \int_{S^{J}_{-k}} \frac{\partial G_{i,-k}}{\partial n} dS \tag{3.29}$$

The term $\left(\tilde{S}_{ij}\right)_{2w}$ is the effective potential at point *i* due to panel *j*, and all its image panels. $\tilde{S}^{J}_{i,+k}$ is the contribution to the potential by the *jth* panel's *kth* image above the horizontal axis, as shown in Figure (3-6). $\tilde{S}^{J}_{i,-k}$ corresponds to the contribution of a panel which lies below the horizontal axis.

In the code P2D-BLWC, the method of images has been implemented. The formulation of Chapter 2 is essentially the same when including images. The only difference is that the influence coefficients must be modified to account for the image panels The modified influence coefficients were computed using expression (3.27) for sources, and other similar expressions for dipoles. Note however that one can only use a finite number of terms in computing the modified influence coefficients. In this work the number of pairs of image panels kept was taken to be *NIMG*. There are two considerations when choosing a value for *NIMG*. First, enough pairs of images must be included so that the kinematic boundary condition at the wall has been satisfied. Then, the value chosen must be one for which the results are converged.

In determining the number of image panels required for the satisfaction of the kinematic boundary condition at the wall, it was necessary to consider two cases: inviscid flow; and inviscid flow with blowing sources. Figures (3-7) and (3-8) show the normal velocity along the lower and upper walls. In each figure, the normal velocity computed using 20 images is compared with the normal velocity computed without images. This latter case corresponds to unbounded flow. The foil section used in this comparison was a NACA65A at an angle of attack of 5°. The tunnel height was half of the chord length of the foil. Comparison of the two curves in each figure, shows that using 20 images results in a velocity which is much smaller than the velocity along the wall without images. For 20 images, the velocities were on the order of $O(10^{-4})$. It was found that using as few as

5 images gave normal velocities on the order of $O(10^{-3})$. Figure (3-9) shows similar results when viscous blowing sources are included. Shown are the velocities along the upper and lower walls computed using 10 images, for the same configuration. With only 10 image pairs we see that the normal velocities at the wall, tend to be on the order of $O(10^{-3})$ to within three chord lengths in both the up and down stream directions.

The final consideration in choosing *NIMG*, is the determination of a value such that the solution is a converged one. Many parameters can be examined when considering convergence with number of panels. Some parameters examined for this study were drag, cavity height, cavity velocity, and circulation. It was found that most of these parameters converged at about 5 to 10 images. Interestingly enough, the circulation about the foil was found to converge a bit more slowly than the other parameters. Figure (3-9) shows that it takes at least 20 panels for circulation to converge. However, the circulation for 10 images was found to be within 1 percent of the converged value.

3.3. Convergence Results for P2D-BLWC

In the last section, convergence results were shown for the code P2D-BLWC, as the number of images were varied. In this section convergence of the method with number of panels and iterations is examined. The total number of panels is equal to the number of panels on the body plus those of the wake. In this section, the number of wake panels will be fixed at 30, and the wake length is taken to be 5 chord lengths. The results presented here are meant to demonstrate convergence for the cases of inviscid and viscous cavity flow. Hufford has demonstrated convergence for viscous fully wetted flow, and the reader is referred to his thesis for details [8].

Figures (3-11) and (3-12) show results of inviscid cavity convergence tests, for a NACA65A foil with zero camber, at an angle of attack of 5°. The foil thickness is 6

percent of the chord length. Detachment was arbitrarily chosen at 10 percent of the chord length, and the converged cavitation number was found to be $\sigma = .6$. Figure (3-11) shows that cavity velocity q_c , cavitation number and circulation converge at about 90 panels. However, the velocity at the cavity trailing edge, U^{cte}, converged much less rapidly. The number of panels necessary for convergence of U^{cte} was found to be about 160. Figure (3-12) shows that the cavity height converged at the same point. These results are not particularly impressive. However, one must note that the cavity detachment point chosen, is quite far from the leading edge. Figure (3-13) shows convergence results for another configuration, but this time the detachment point was chosen using the criterion described in Section 1.2. The foil used was a NACA0010 at an angle of attack 2°. The cavity length was 30 percent of the chord, and the converged cavity number was found to be $\sigma = 68$. Use of the detachment criterion resulted in detachment at 1 percent of the chord length. In this case the cavity height distribution converged at only 80 panels, or half the number of panels for the configuration of Figure (3-13).

Figures (3-14) through (3-16) show convergence results for viscous cavity flow. The configuration is the same as that used for the convergence tests of Figure (3-13). The Reynolds number for this test was 10^6. The edge velocity on the suction side of the foil is shown in Figure (3-14). As this plot shows, the edge velocity converges at about 80 panels. Note in this figure that the edge velocity is constant over the cavity surface save for the transition zone, which in this case is 40 percent of the cavity length. This is a result of the dynamic boundary condition on the cavity surface. The displacement thickness also converges at 80 panels, as shown in Figure (3-15). A similar result for the momentum thickness is presented in Figure (3-16).

The curves shown in Figures (3-14), (3-15) and (3-16), are intended to demonstrate convergence of the method with number of panels. Another point of concern is convergence of the viscous solution with number of iterations. Remember, that the dynamic boundary condition on the cavity is satisfied by the iterative process described in

Section 3.1. The cavity solver iterates until the perturbations δq_c, δU^{cte} and δm_j^c, are less than some prescribed value. Figure (3-17) shows the cavity heights from the viscous solution for the same configuration as Figure (3-13). The results presented are for the first, fifth and twelfth iterations. From this we see that by the fifth iteration the cavity height has essentially converged. The difference between the fifth and twelfth iterations is small. Figures (3-18) and (3-19) show the edge velocity and displacement thickness for the first and fifth iterations. The twelfth was not presented because it was virtually identical to the results from the fifth iteration. By the fifth iteration we see from (3-18) that the dynamic boundary condition on the cavity is satisfied. Figure (3-20) shows the rate of convergence based on the maximum cavity height perturbation. This perturbation, δh_{max}, is 2.23×10^{-2} for the first iteration, and by the third it is 1.15×10^{-6}. These number seem small, but some basis for comparison is necessary. A relative tolerance for the cavity height can be defined as follows

$$\Delta h = \delta h / H_c \tag{3.30}$$

where, H_c is some scale value for the cavity height. An appropriate value is the maximum cavity height. This value for the first iteration is 3.5×10^{-3} using Figure (3-17). The relative tolerance for the first iteration is $\Delta h = 7.8x10^{-5}$, and by the third it is $\Delta h = 3.7x10^{-9}$. So in terms of cavity height, convergence is quite rapid. Figure (3-21) shows the convergence with number of iterations for δq_c and δU^{cte}. One can define tolerances for these variables also, where the scale in each case is the cavity velocity. shows the convergence of cavity velocity with number of iterations. These tolerances for the first iteration were found to be $\Delta q_c = 2.2x10^{-2}$ and $\Delta U^{cte} = 7.6x10^{-3}$. By the third iteration, the solution had converged to within $\Delta q_c = 1.2x10^{-6}$ and $\Delta U^{cte} = 5.6x10^{-5}$. Note that the cavity trailing edge velocity converges least rapidly of all.

3.4. Code Validation for Viscous Fully Wetted Flows

In this section the results of P2D-BLWC for viscous fully wetted flow, are compared with those from XFOIL. Although fully wetted flow is not the focus of this research, this section is included to demonstrate the validity of the results from the viscous solver.

The geometry used for this comparison was a NACA0010, at an angle of attack of 5°. The Reynolds number for these runs was 10^6, and the critical value for the transition model was taken to be 9. The initial location of transition was taken to be at 95 percent of the chord length on both the suction and pressure sides of the foil. Both codes were run using 100 panels on the foil. Since XFOIL cannot be used for bounded flows, the number of images was taken to be zero.

Figure (3-22) shows the pressure distribution on the foil computed by both XFOIL and P2D-BLWC. As this plot shows, the two results compare quite favorably over most of the foil. The greatest difference is found near the trailing edge of the foil. This is due to the fact that each code uses different discretizations for the foil. Cosine spacing was used with P2D-BLWC. The discretization used by XFOIL allowed for more panels near the leading and trailing edges of the foil as does cosine spacing, but in a slightly different manner. Another reason for the difference in the results near the trailing edge is related to the application of the Kutta condition. In P2D-BLWC, the Morino-Kutta condition is used, whereas in XFOIL a modified form is used. Similar results for the displacement thickness are shown in Figures (3-23) and (3-24). In Figure (3-23), one may notice that there is a kink at 7 percent of the chord length. This point corresponds to the point of transition as predicted by the two codes. The actual locations of transition predicted by XFOIL were at 6.6 and 96.6 percent of the chord for the suction and pressure sides respectively. P2D-BLWC predicted transition on the suction side at 7.4 percent of the chord, and on the pressure side this point was found to be at 99.8 percent of the chord.

3.5. Code Validation for Inviscid Cavity Flows

Several codes exist for the analysis of two dimensional inviscid cavitating flow. In this section the results from P2D-BLWC are compared with one of these codes. The code chosen for this comparison is called PCPAN. It is based on the method due to Kinnas and Fine [12].

The code PCPAN was chosen for the validation of P2D-BLWC, because both codes are based on low order perturbation panel methods. One would expect them to give very similar, if not identical results for a particular configuration. Where configuration is taken to mean the foil geometry, angle of attack, discretization, cavity detachment point and length. However, several fundamental differences do exist between the two methods. The most important of these are:

- The use and placement of blowing sources in P2D-BLWC.
- Extrapolation of perturbation potential at leading edge of cavity in PCPAN.
- Differences in the models for the pressure recovery zones.
- Different discretizations on the foil.

Before jumping into a discussion of the validation tests, it is worthwhile to compare each method so one can interpret any differences in the results.

As mentioned before, both methods are based on low order perturbation panel methods. By low order it is meant that any source, dipole or blowing source distributions, are assumed to have a constant strength over the panel. In PCPAN, a distribution of sources and dipoles are placed on the cavity surface and everywhere on the foil body, except under the cavity. In P2D-BLWC, source and dipoles are placed on the body and blowing sources on those panels which lie beneath the cavity. Here we find two differences occurring. The source and dipole distribution of the method described in this paper are those which correspond to fully wetted inviscid flow, while the blowing sources

are used to satisfy the dynamic boundary condition on the cavity. The second difference is that the blowing sources are placed on the foil surface, not the actual cavity surface. However, since the cavity surface is unknown, PCPAN places the cavity surface initially on the surface of the foil. So the zeroth iteration of PCPAN corresponds to the method presented in this paper.

The dynamic boundary condition on the cavity surface is

$$\frac{\partial \phi}{\partial s_c} = q_c(s_c) - \frac{\partial \Phi_{in}}{\partial s_c} \tag{3.31}$$

where, s_c in this case is the arc length along the surface of the cavity measured from the detachment point. The boundary condition (3.31), is the form applied in the present work. Kinnas and Fine work with another form of the boundary condition, obtained by integrating (3.31)

$$\phi(s_c) - \phi(0) = \int_0^{s_c} q_c(t)dt - \Phi_{in}(s_c) + \Phi_{in}(0) \tag{3.32}$$

The resulting equation involves the perturbation at the start of the cavity, $\phi(0)$. However, this is an unknown quantity, so some method is necessary to determine its value. Kinnas and Fine approximate it by using a cubic extrapolation of the perturbation potentials on those panels which precede the detachment point [12]. In the present method, no such approximation to the perturbation potential is necessary.

Before presenting the results, it is necessary to consider one more difference between the two methods, which would affect the results of the comparison. The model used for pressure recovery by Kinnas and Fine is

$$q_c(s_c) = q_c[1 - AF(s_c)] \tag{3.33}$$

Note that with this model, by specifying the constant A, one is effectively requiring that the velocity at the trailing edge of the cavity be some fraction of the cavity velocity q_c. The model used here

$$q_c(s_c) = q_c[1 - F(s_c)] + U^{cte}F(s_c) \tag{3.34}$$

places no such restriction on the velocity at the trailing edge. Instead it is determined as part of the solution. If one is to compare the two codes, it is necessary to determine A such that the two models are equivalent. The effective value for A which would satisfy this requirement is

$$A_{eff} = 1 - U^{cte}/q_c \tag{3.35}$$

When comparing the two codes, P2D-BLWC is run first so that a value of A_{eff} can be computed for input to PCPAN.

The first comparison is for a NACA65A foil at an angle of attack of 5°. The thickness of the foil relative to the chord is 0.06. The number of panels in each case was two hundred. Cavity detachment was at 10 percent of the chord length on the suction side. Cavity length was 30 percent of the chord, and the pressure recovery parameters were υ=1 0 and λ=0 05. The code P2D-BLWC was run first, and A_{eff} was found to be 0 32. Figure (3-25) shows the cavity height distributions computed by each code. Note that near the leading edge of the cavity the two distributions compare quite favorably. However, near the trailing edge of the cavity, the differences between the two curves are more pronounced. One reason for this is that, though the number of panels is the same, the discretizations are slightly different. The cavity number computed by P2D-BLWC was found to be 0.595, whereas PCPAN predicted 0.586 for a difference of 1.5%.

For the next comparison, the transition zone is taken to be λ=0. Consider the computed cavity height distributions, of Figure (3-26). The results shown are for a NACA1606, at an angle of attack of 5°. Detachment was taken to be at the leading edge, and the length of the cavity was set at 30 percent of the chord length. In this case, the discretizations were the same for each method. The effective velocity fraction was found to be A_{eff} =1. For this comparison υ=1. As Figure (3-26) shows, the curves are nearly identical near the trailing edge, with the greatest differences appearing toward the leading edge and midpsan of the cavity. Since the geometries are the same in this cases, the difference may be attributed to the approximation for the perturbation potential at the

cavity leading edge. The cavitation number predicted by P2D-BLWC was 0.607, and the value predicted by PCPAN was 0.595.

Now consider the case when the transition length is 40 percent of the cavity length. Figure (3-27) shows such a case for a NACA65A foil at an angle of attack of 5°. Detachment occurs at the leading edge, and the cavity length is 30 percent of the chord. The pressure recovery parameters are λ=0.4, υ=1 and A_{eff}=.332. As a result of this, the cavity height distributions, as computed by the two codes, are quite different as shown in Figure (3-27). The cavity as computed by the code PCPAN has negative heights near its trailing edge. This would correspond to a cavity inside the foil. In contrast, the resulting cavity height from P2D-BLWC, does not have this problem. In this case the cavity velocity as predicted by P2D-BLWC was 1.538, and the result from PCPAN was 1.528. Note that in this case, the discretizations are the same for each code.

3.6. Validation for Viscous Cavity Flows

When validating the present method for fully wetted viscous flow and inviscid cavity flow, it was also possible to use another code for the validation phase. However, for viscous cavity flows it is not possible to do this for no other similar codes exist. So some other means of validation is necessary.

In the present method, the inviscid and viscous solvers are interactive. Starting from some initial distribution, the cavity surface is perturbed each iteration and the boundary layer solution is calculated. This continues until the edge velocity on the surface satisfies the dynamic boundary condition. However, if one knew the location of the cavity surface beforehand, this iterative process would not be necessary. It is this last idea which can be used to formulate a method for validating the results from P2D-BLWC for viscous cavity flow.

The method used for validating the results of P2D-BLWC, is to take the predicted height distribution and use it as an input to some fully wetted boundary layer code. The way this is carried out in practice is quite simple. Consider Figure (3-28a), which shows a typical foil and cavity. One can replace the foil and cavity with an equivalent foil. This equivalent foil is the actual foil plus cavity as shown in Figure (3-28b). A boundary layer solution can then be computed for the equivalent foil, and compared to the solution from P2D-BLWC. Note that when solving the equivalent problem, the following condition must be imposed

$$C_f = 0 \tag{3.36}$$

on that portion of the equivalent foil which corresponds to the cavity surface. The fully wetted flow code used to solve the equivalent problem is PAN2D-BL.

The first test was conducted using a NACA0010 foil with 80 panels, at an angle of attack of 5°. The Reynolds number was 10^6, and the boundary layer parameters were λ =0.4, ν=0.5 and l=0.3. Detachment for this case was at 1 percent of the chord length. The relative tolerances for the velocities and mass defect were set at $\Delta q_c = \Delta U^{cte} = \Delta m^c = 10^{-5}$. Convergence for these tolerances occurred by the eleventh iteration. Figure (3-29) shows the edge velocity distributions on the suction side of the actual and equivalent foil. The two curves are practically identical over most of the foil. However, the equivalent distribution does deviate slightly from the actual curve over part of the cavity surface. The cavitation number computed by P2D-BLWC was σ=0.625. The cavity number for the equivalent problem, based on the maximum cavity velocity, was σ=0.628 for a difference of 0.5 percent. Figure (3-30) shows the displacement thickness distribution for each geometry. In this instance, the two curves are nearly indistinguishable.

The results for the next case tested are shown in Figures (3-31) and (3-32). The configuration is the same as in the previous case, the difference is now that 200 panels are used instead of 80. In this run, the results from P2D-BLWC for the fifth iteration were

used for the comparison with PAN2D-BL. As we see in Figure (3-31), by the fifth iteration the dynamic boundary condition on the surface is satisfied. The edge velocity for the equivalent geometry is a very good match to the result for the actual geometry. Slight differences between the two geometries are found near the cavity leading edge and the beginning of the transition zone. The displacement thicknesses distributions are nearly identical for the two geometries, as shown in Figure (3-32).

The final case tested here is for a VLR foil section. This geometry is the same as that used in the experiment described in Chapter 4. The thickness is t/c=0.04, f/c=0.02, and the leading edge radius is 0.002876 relative to the chord. The angle of attack was set at 6°. The cavity parameters for this run were λ=0.4, ν=0.5 l=0.2, and detachment was at 4 percent of the chord length. The Reynolds number was 2.86×10^6. In this case, 10 image were used to model the walls. The height of the tunnel was taken to be equal to the chord length. The tolerances used were $\Delta q_c = \Delta U^{cte} = \Delta m^c = 10^{-5}$. Convergence for this geometry occurred by the eighth iteration. Figure (3-33) shows the edge velocity results for the actual and equivalent geometries. Again the two distributions are nearly identical. Similar results are found for the displacement thickness distributions, as shown in Figure (3-34).

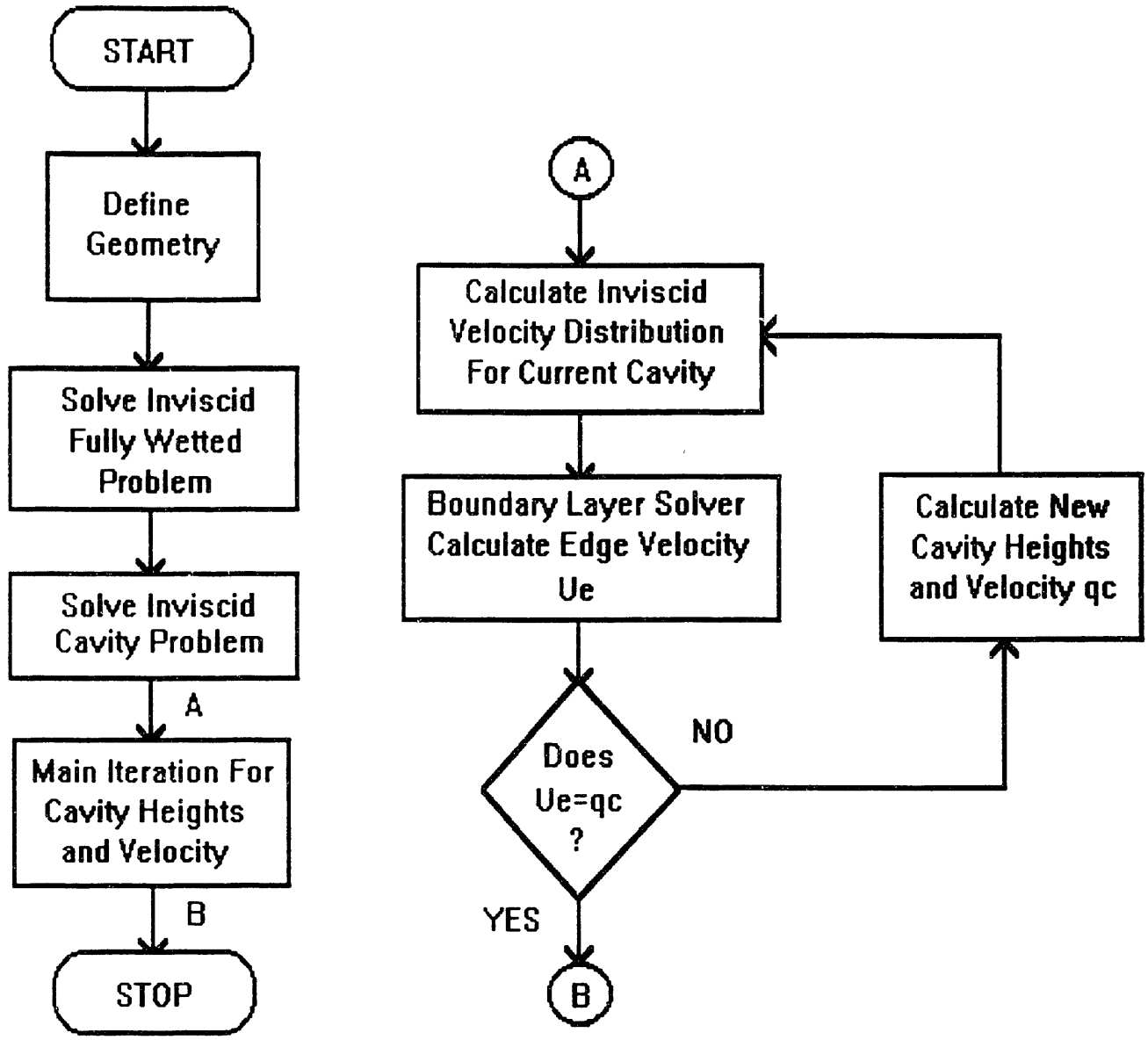

Figure (3-1) Flow chart of the double Newton iteration.

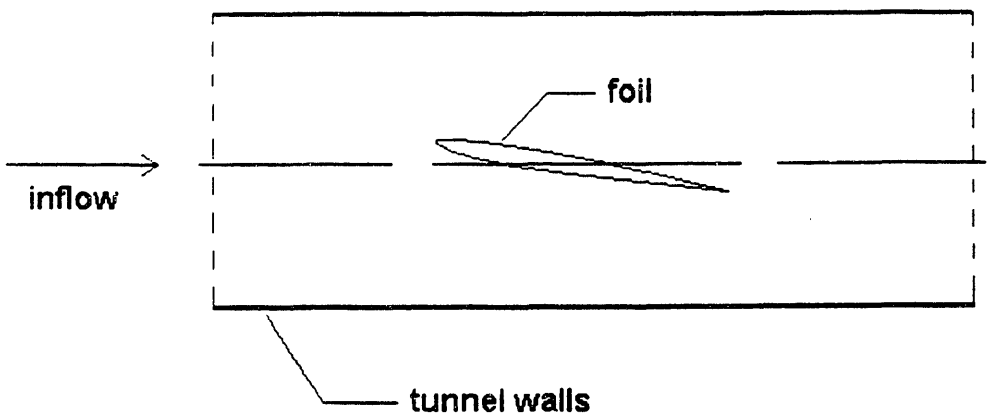

Figure (3-2) Schematic of experimental setup. Inflow to test section is approximately uniform.

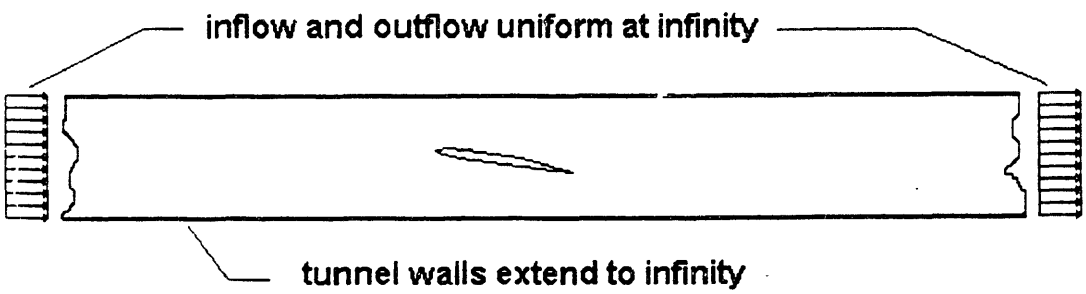

Figure (3-3) Approximating the tunnel with two semi-infinite walls.

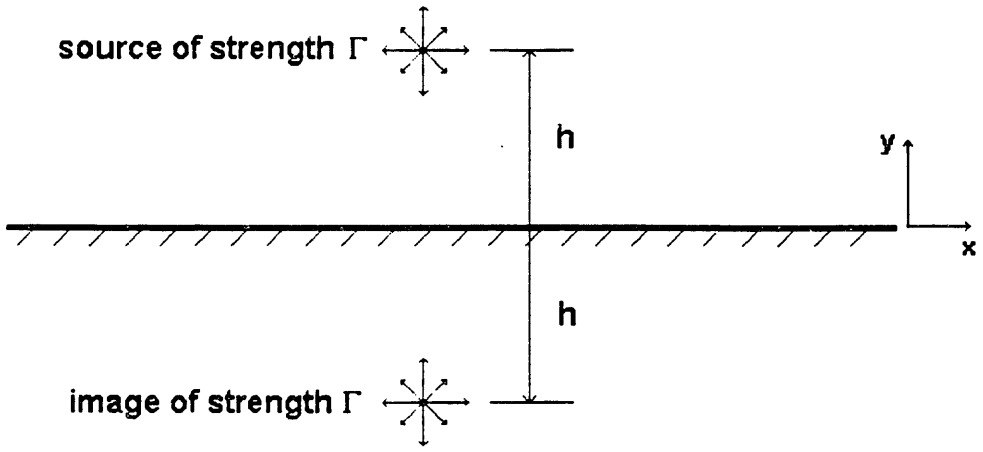

Figure (3-4) Image method applied to a source near a wall.

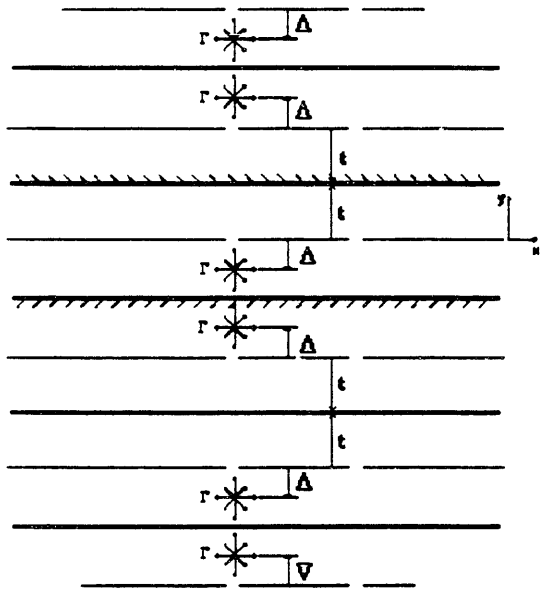

Figure (3-5) Image method applied to a source located between two walls.

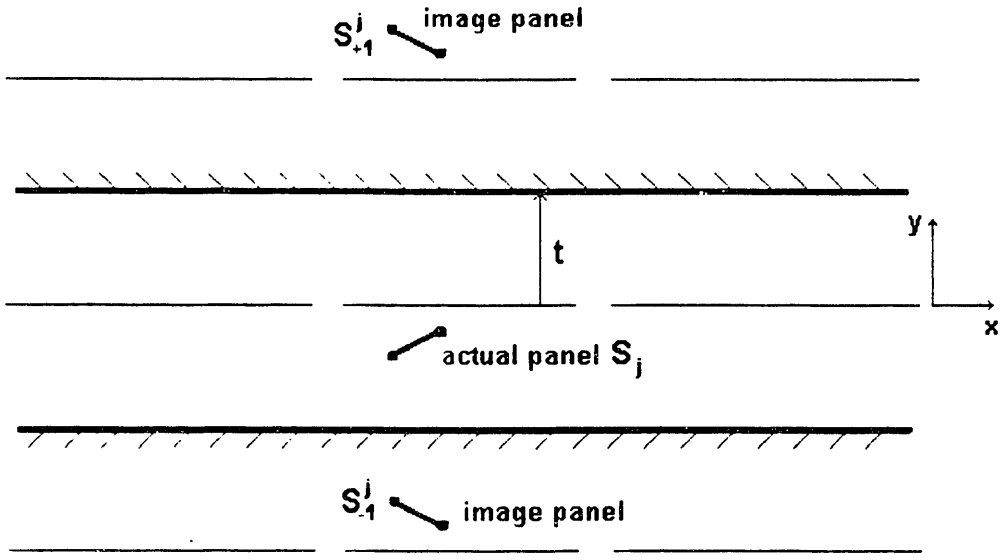

Figure (3-6) Image method applied to a panel between two walls.

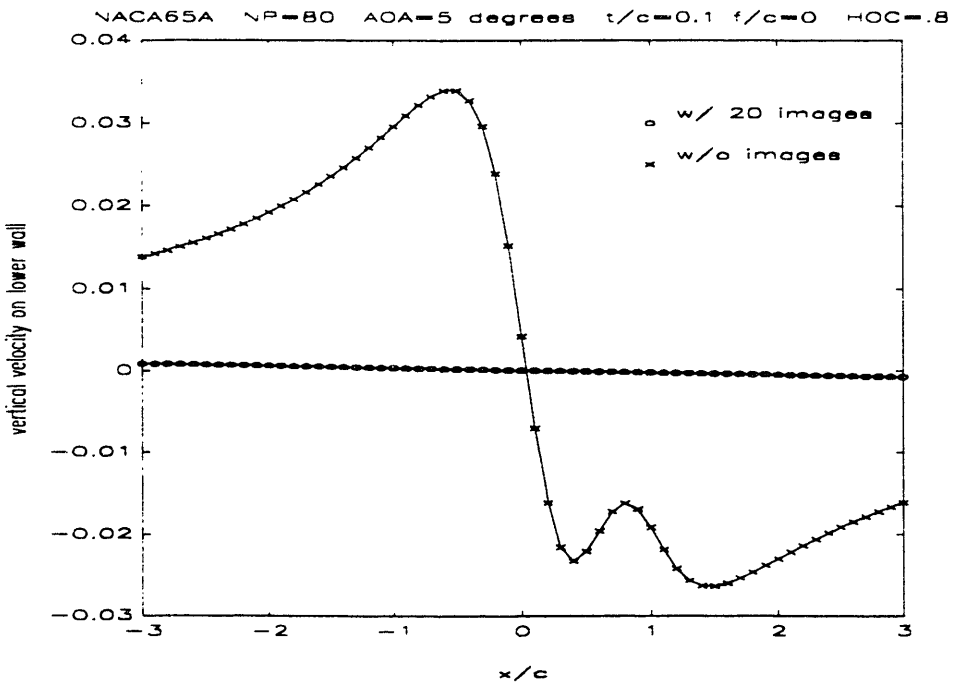

Figure (3-7) Velocity normal to lower wall with and without images for inviscid flow.

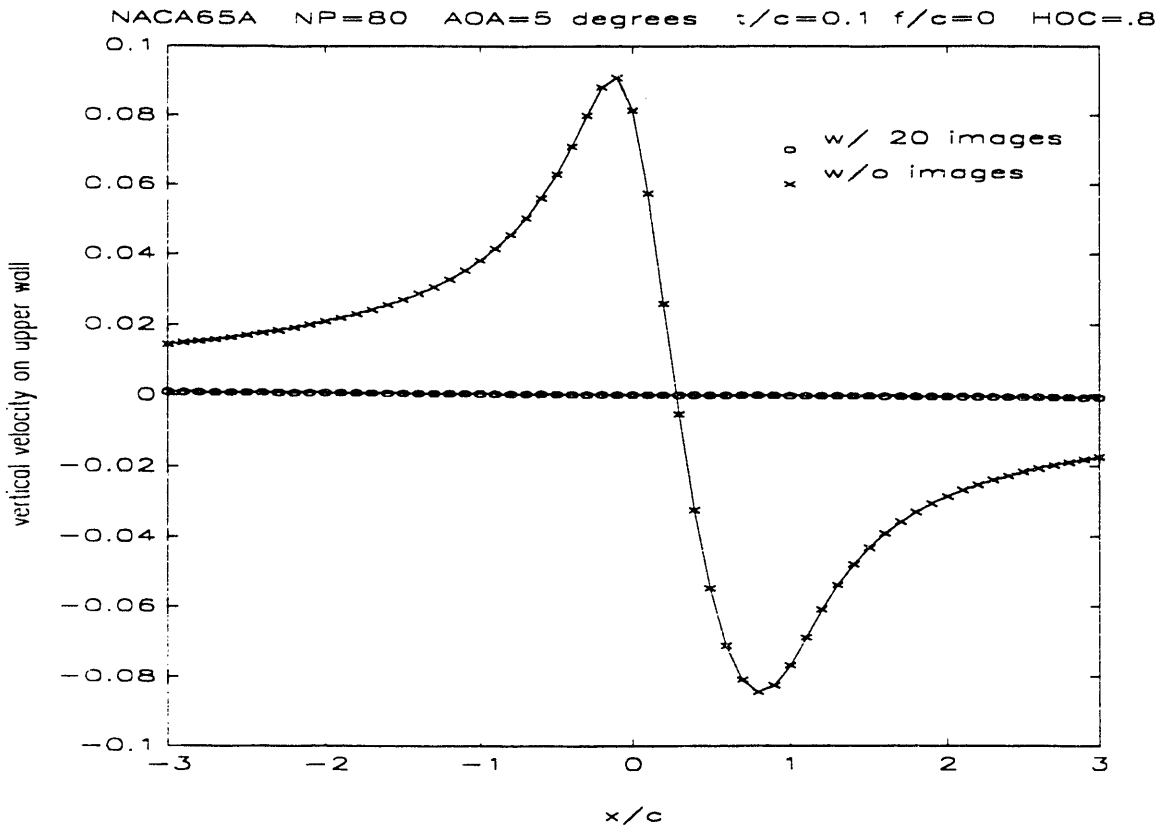

Figure (3-8) Velocity normal to upper wall with and without images for inviscid flow.

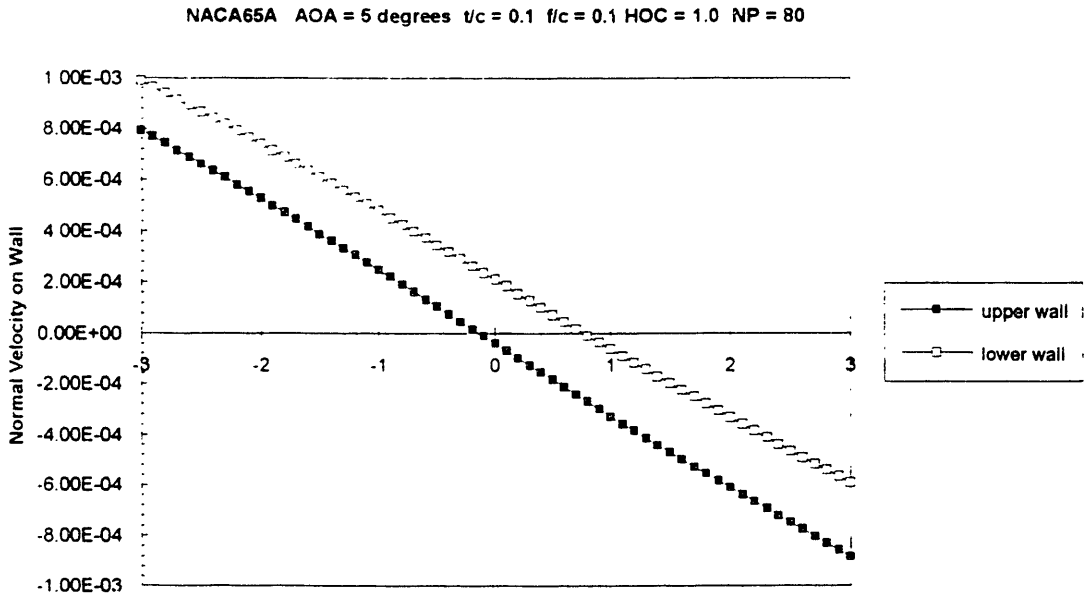

Figure (3-9) Velocity normal to walls with 10 image pairs, for viscous flow.

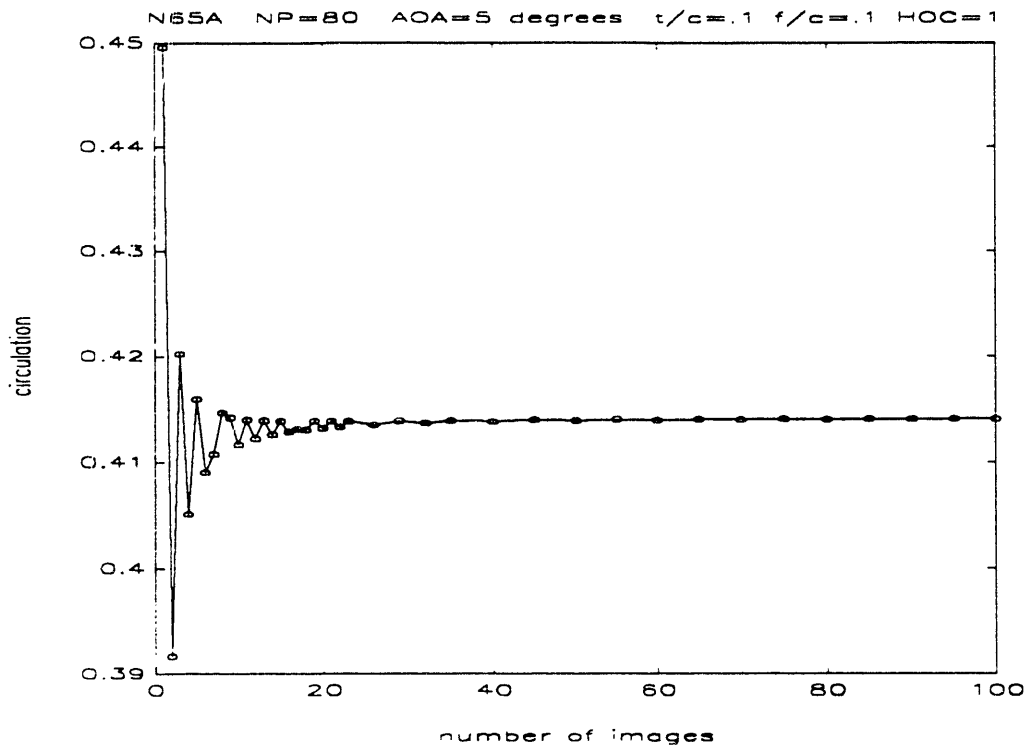

Figure (3-10) Convergence of circulation with number of images.

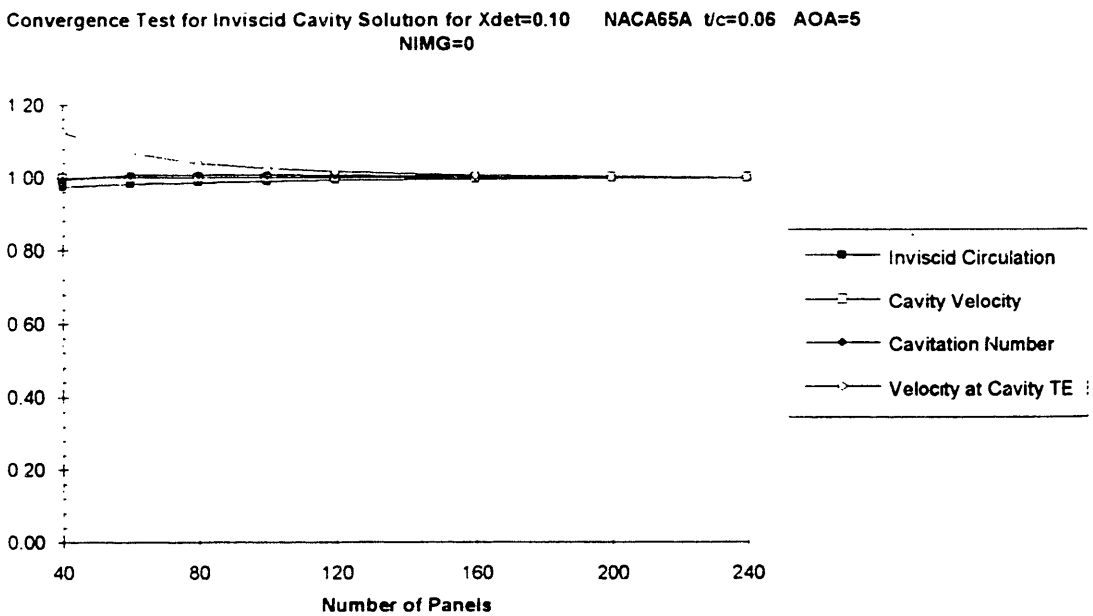

Figure (3-11) Convergence of inviscid parameters with number of panels on body (converged value=1).

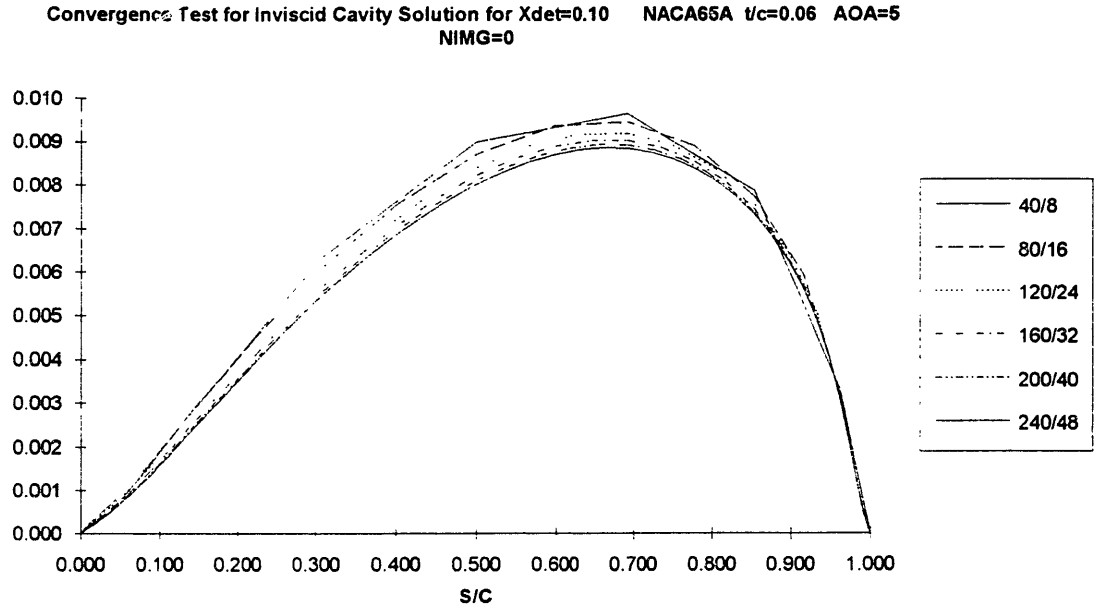

Figure (3-12) Convergence of inviscid cavity height with number of panels on body/cavity.

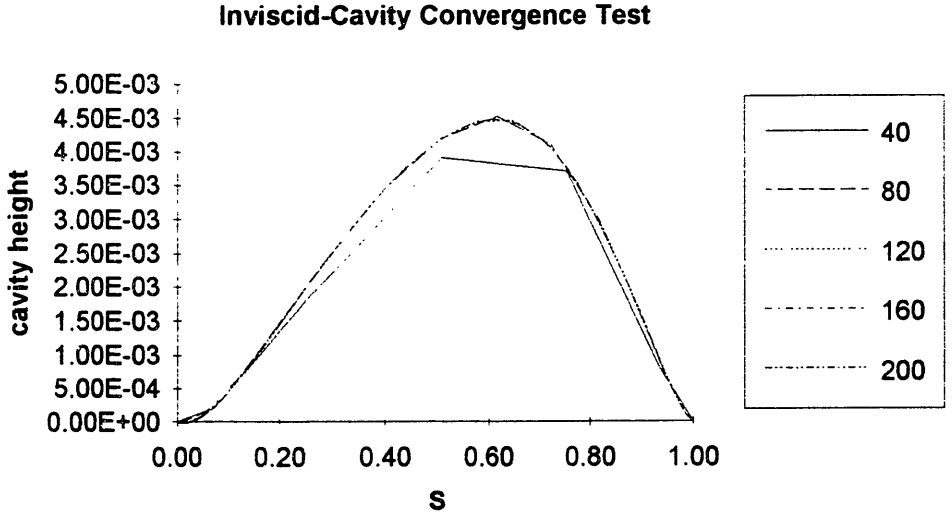

Figure (3-13) Convergence of inviscid cavity height with number of panels on body for a NACA0010 foil at an angle of attack of 2° (σ=0.68).

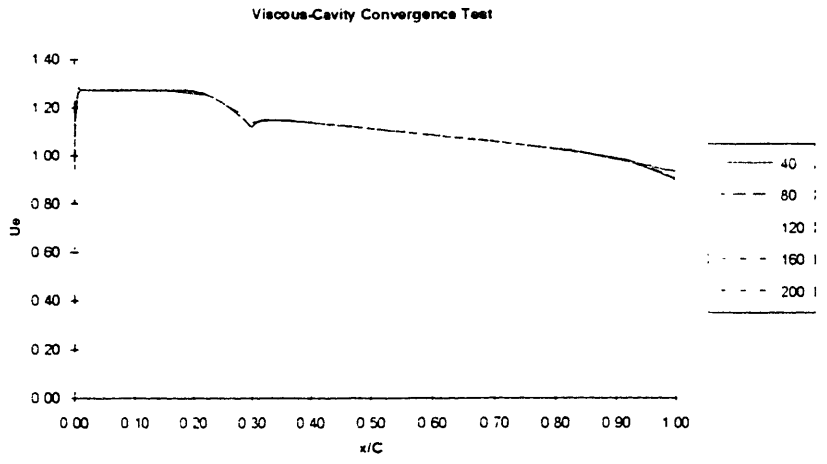

Figure (3-14) Convergence of edge velocity with number of panels on body.

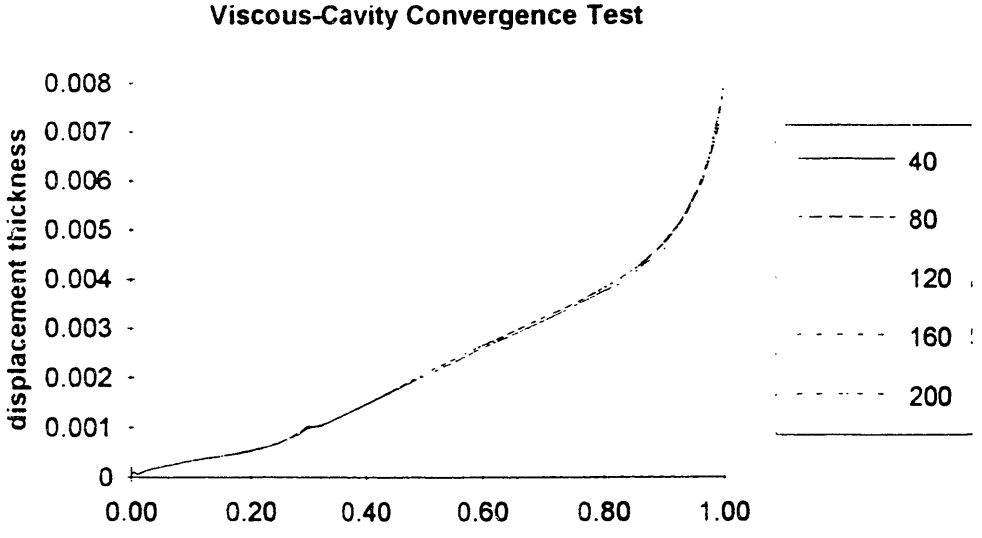

Figure (3-15) Convergence of displacement thickness with number of panels.

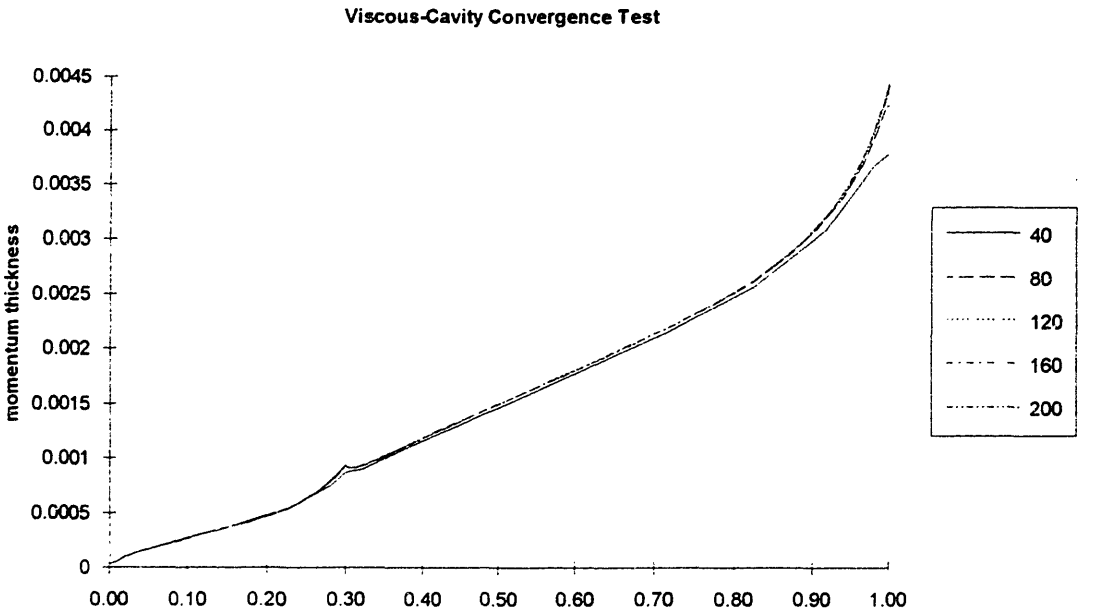

Figure (3-16) Convergence of momentum thickness with number of panels, $Re=10^6$.

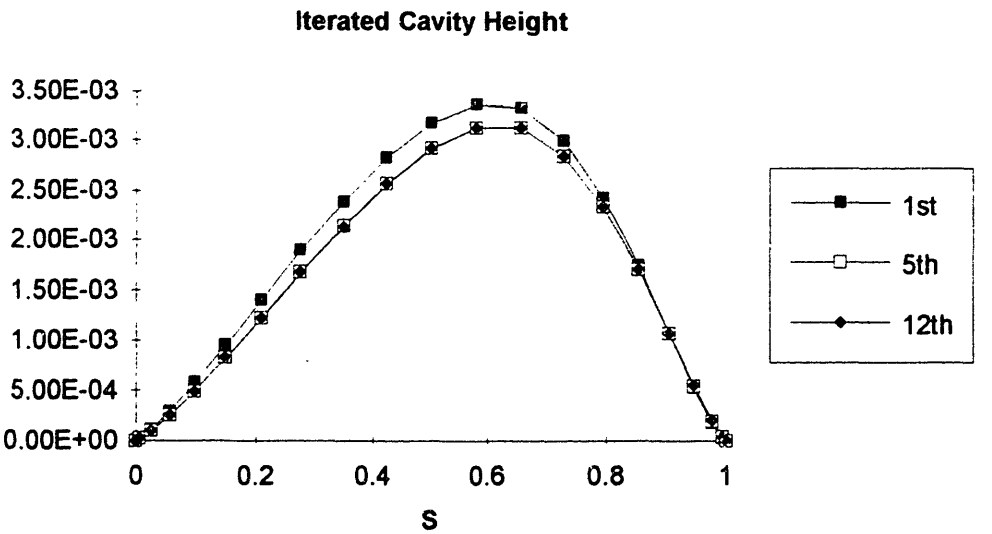

Figure (3-17) Iterated cavity height for configuration of Figure (3-13), $Re=10^6$.

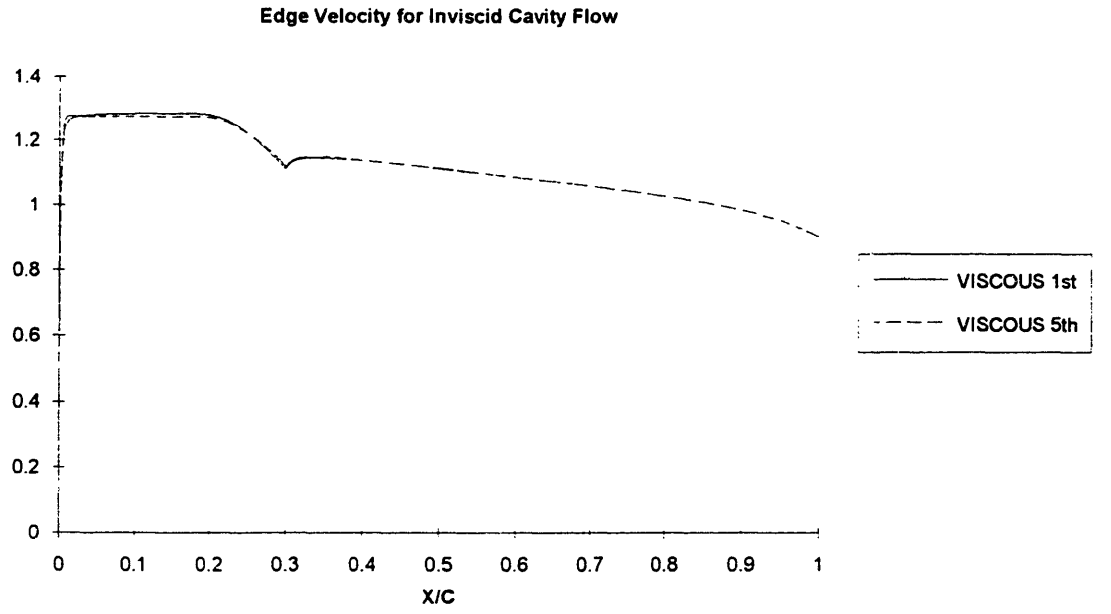

Figure (3-18) Iterated edge velocity for configuration of Figure (3-13), Re=10^6.

Figure (3-19) Iterated displacement thickness for configuration of Figure (3-13), Re=10^6.

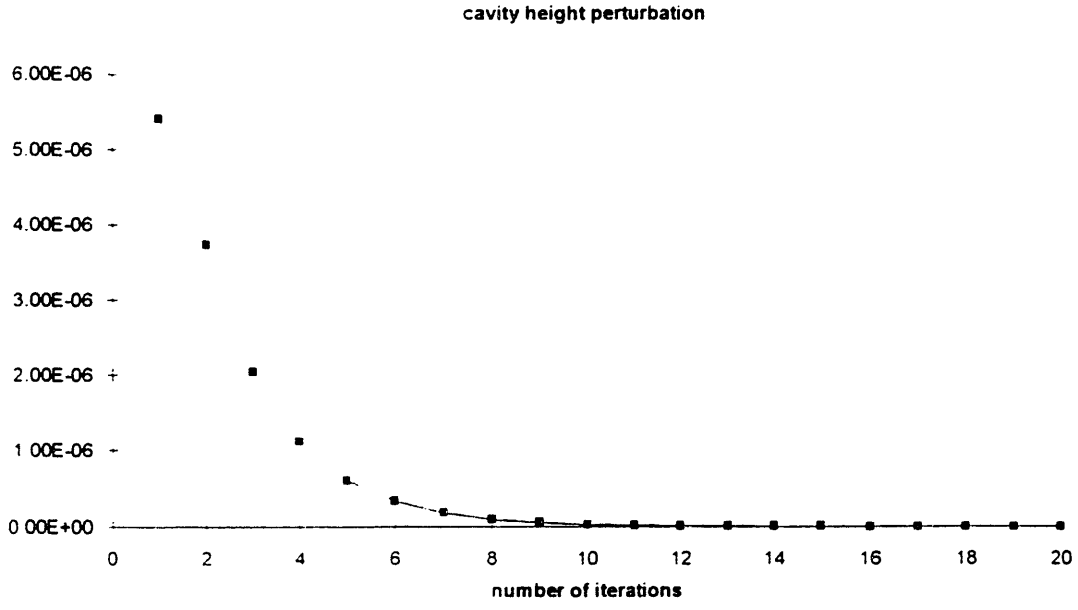

Figure (3-20) Rate of convergence of maximum cavity height perturbation.

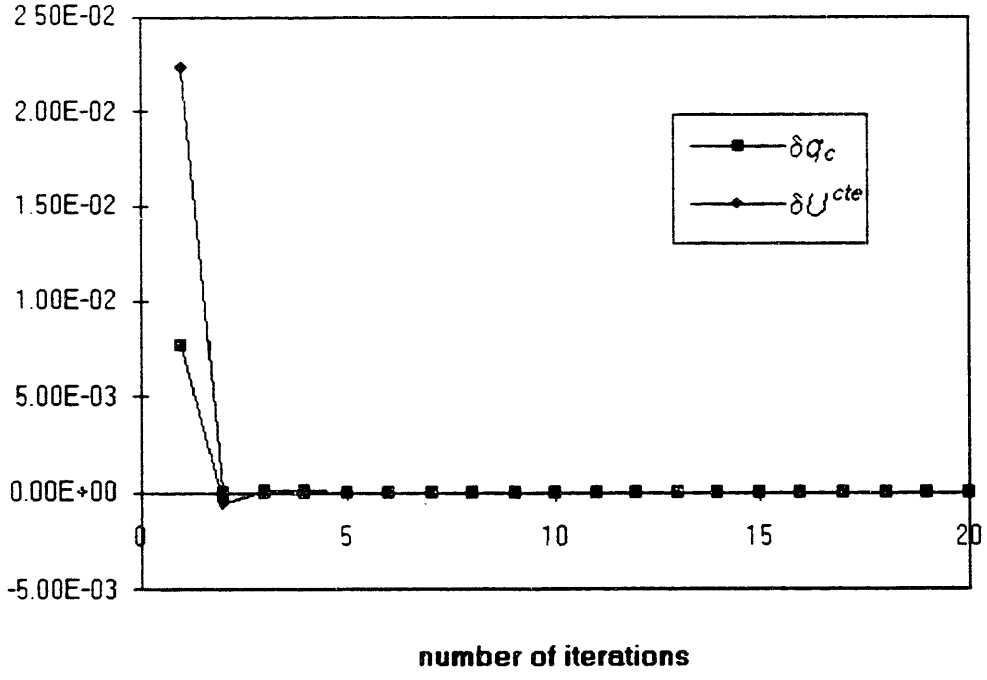

Figure (3-21) Rate of convergence for cavity velocity perturbations with number of iterations.

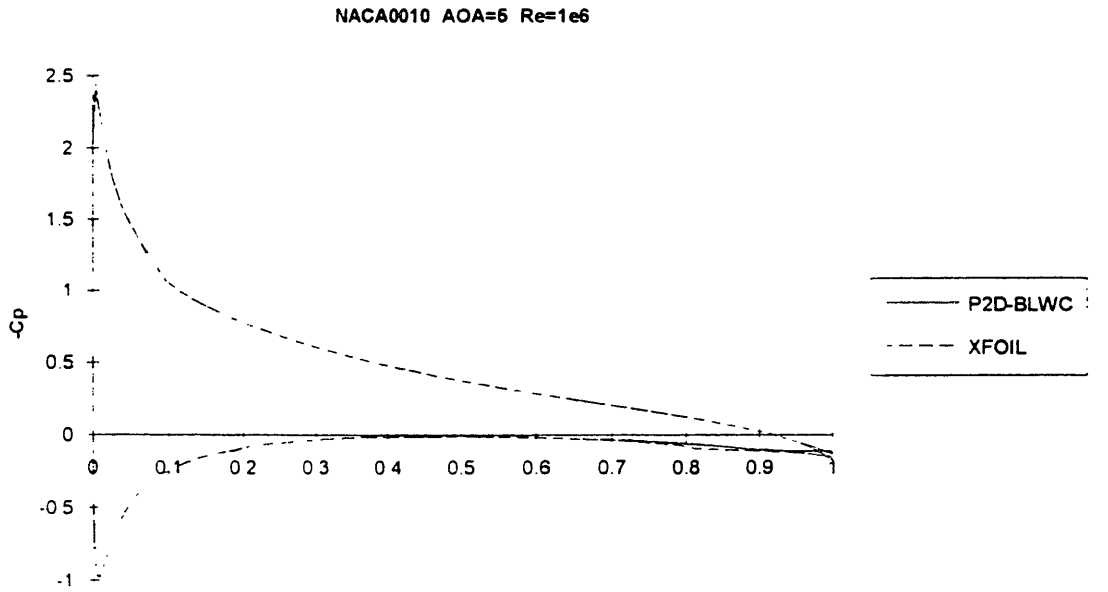

Figure (3-22) Comparison of pressure distribution results from P2D-BLWC and XFOIL.

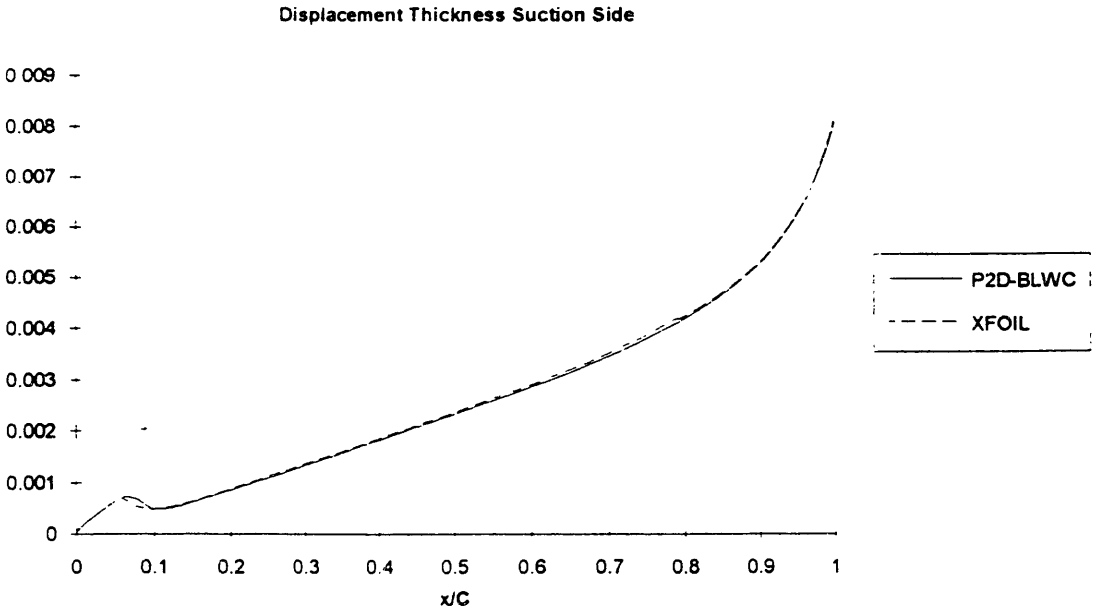

Figure (3-23) Displacement thickness on suction side from P2D-BLWC and XFOIL.

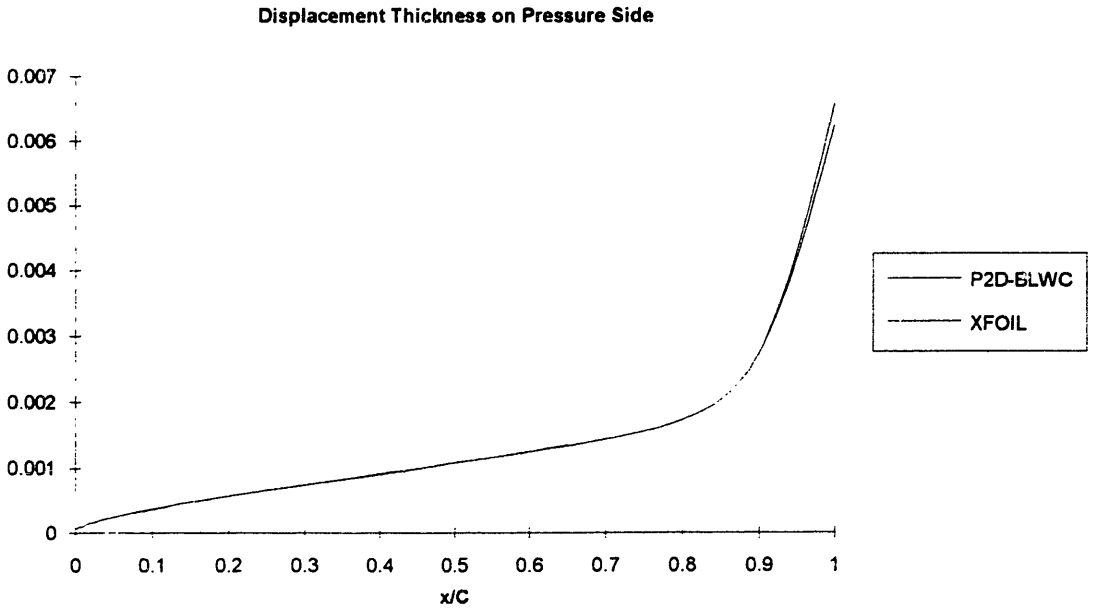

Figure (3-24) Displacement thickness on pressure side from P2D-BLWC and XFOIL.

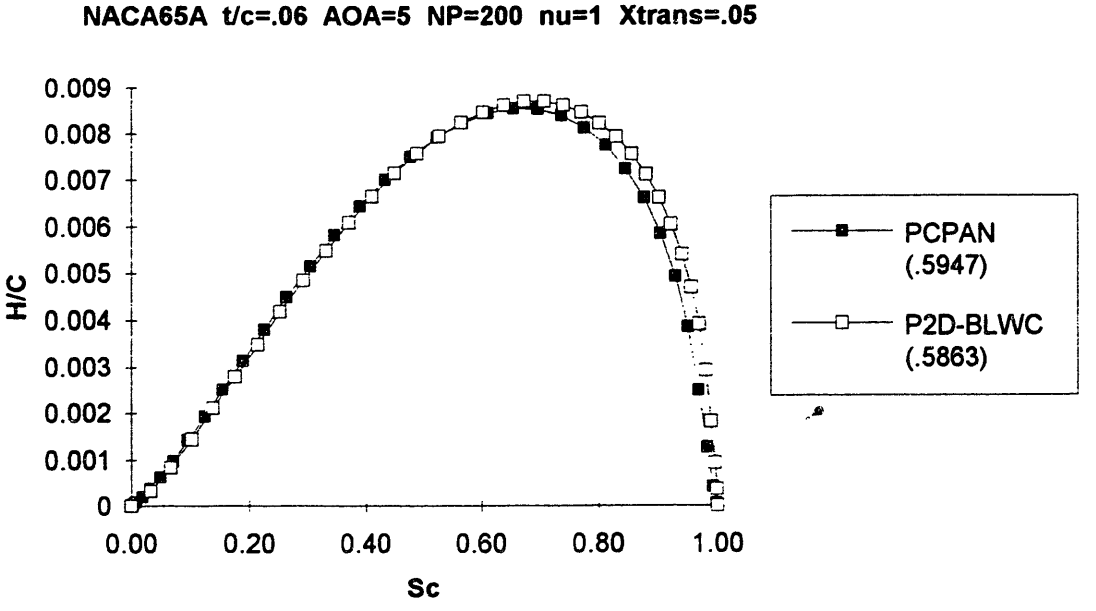

Figure (3-25) Comparison of inviscid cavity height results from P2D-BLWC and PCPAN, l=0.3, λ=.05.

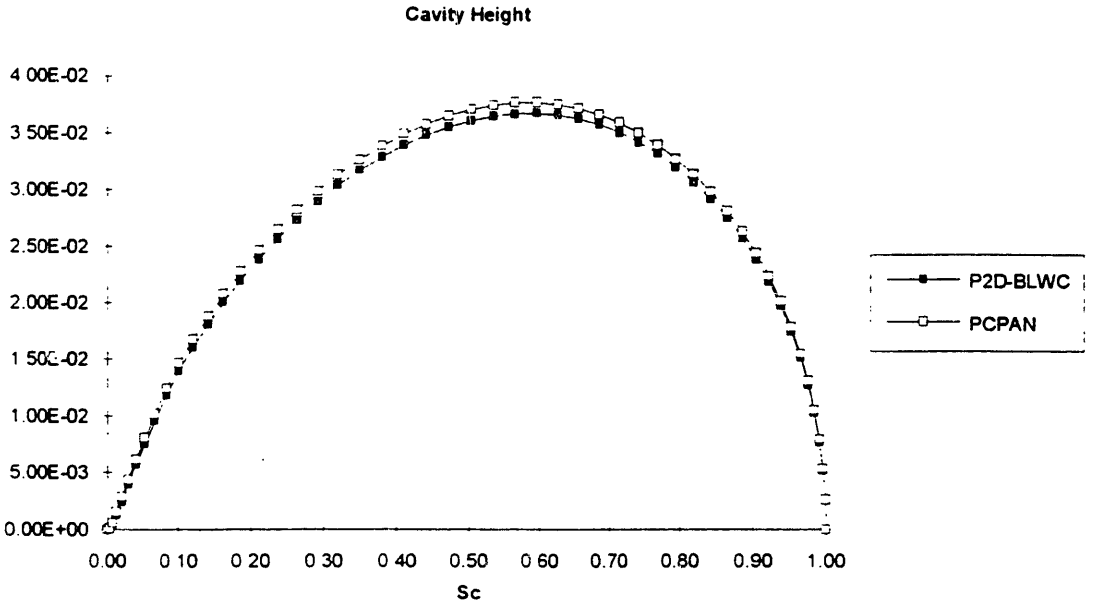

Figure (3-26) Comparison of cavity heights for a transition zone of zero length, l=0.3.

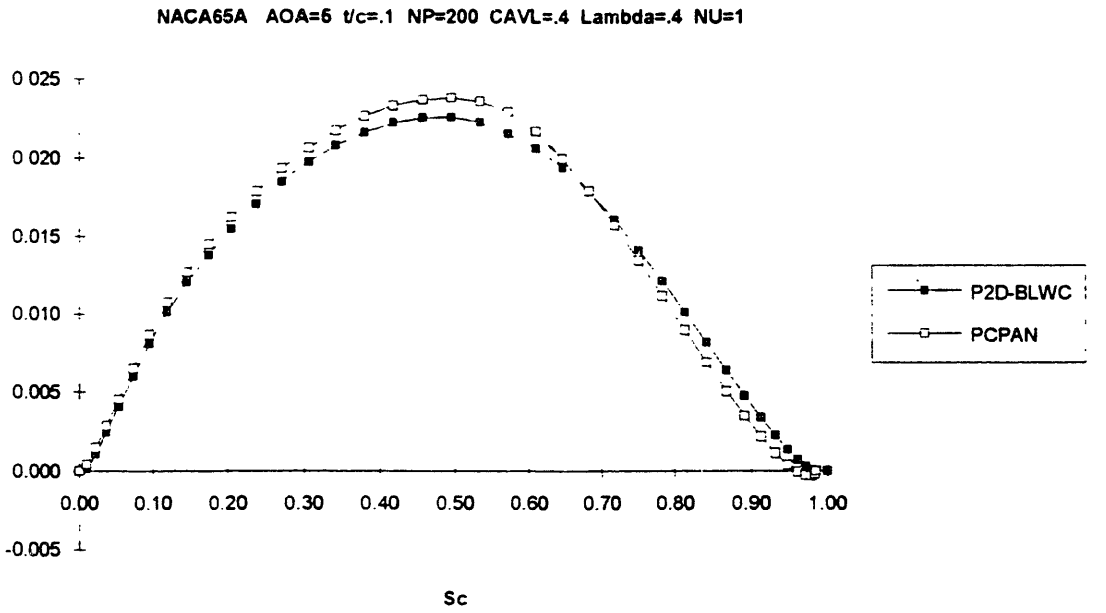

Figure (3-27) Comparison of cavity heights for a NACA65A foil, with a transition zone length of 0.4, l=0.3.

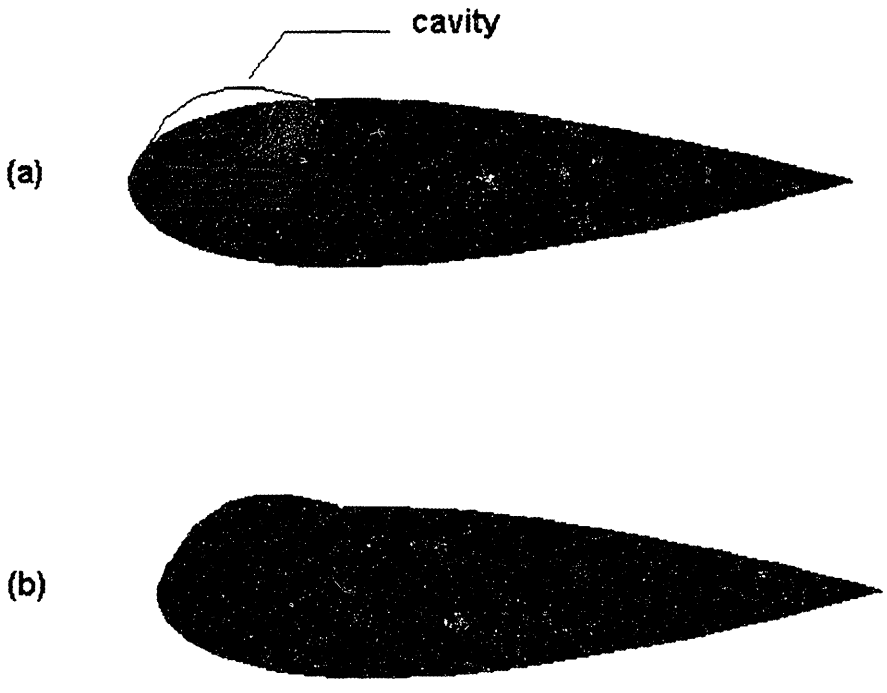

Figure (3-28) (a) Actual geometry with cavity. (b) Geometry for viscous validation test.

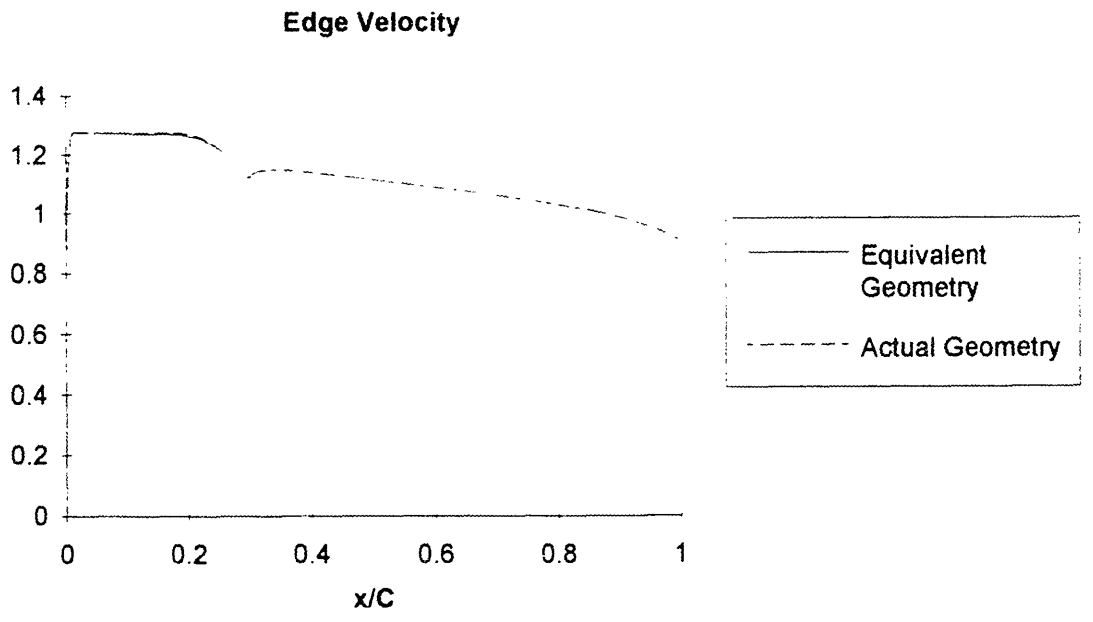

Figure (3-29) Edge velocity validation test results for NACA0010 with 80 panels.

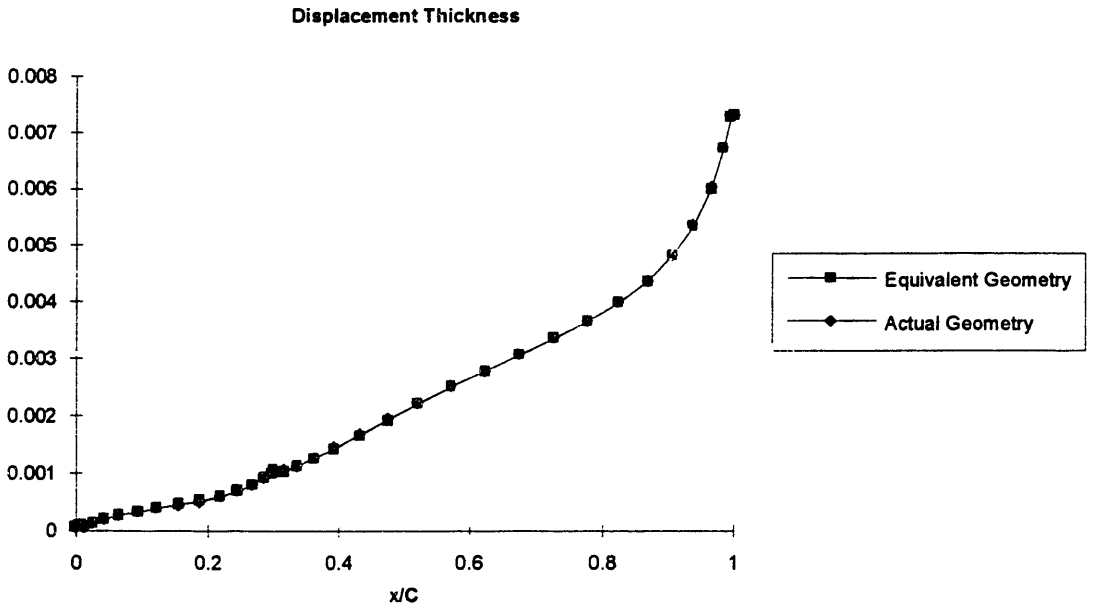

Figure (3-30) Validation test results for NACA0010 with 80 panels. Displacement thickness.

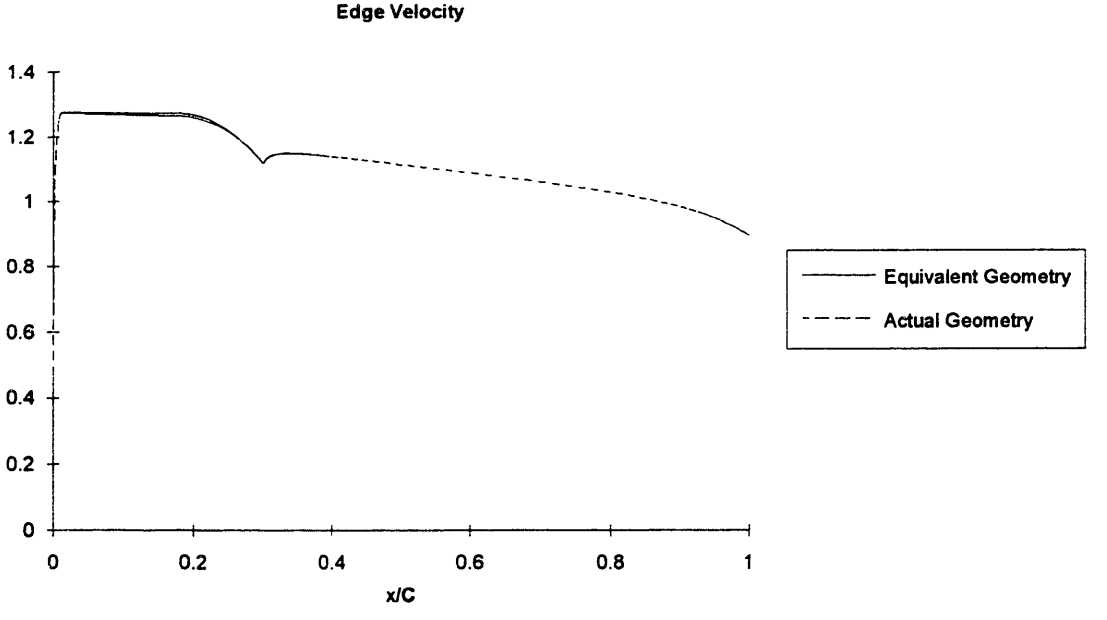

Figure (3-31) Validation test results for NACA0010 with 200 panels. Edge Velocity.

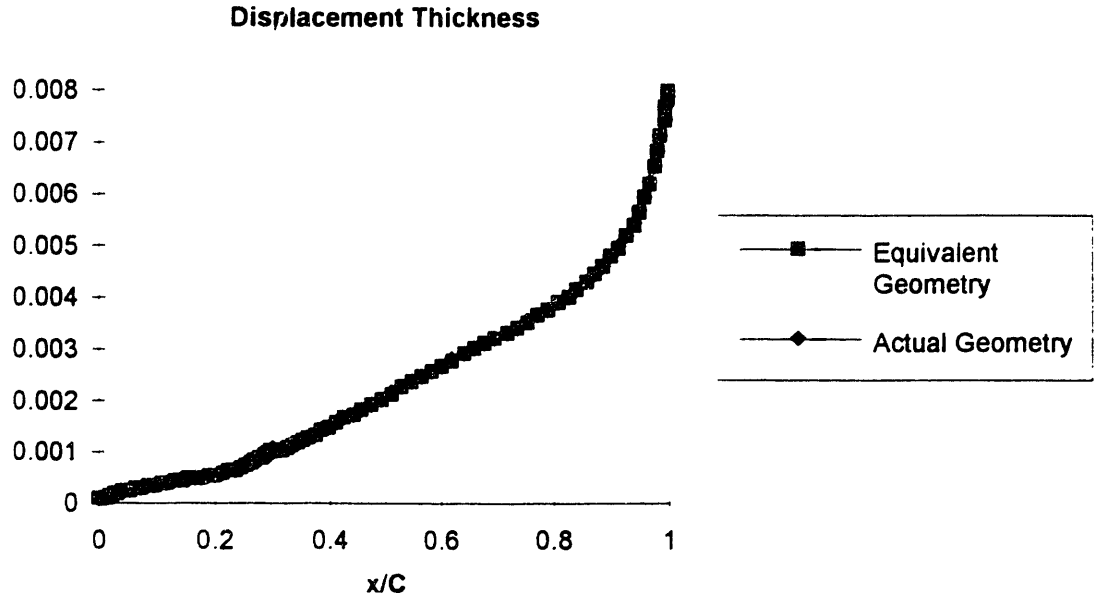

Figure (3-32) Validation test results for NACA0010 with 200 panels. Displacement thickness.

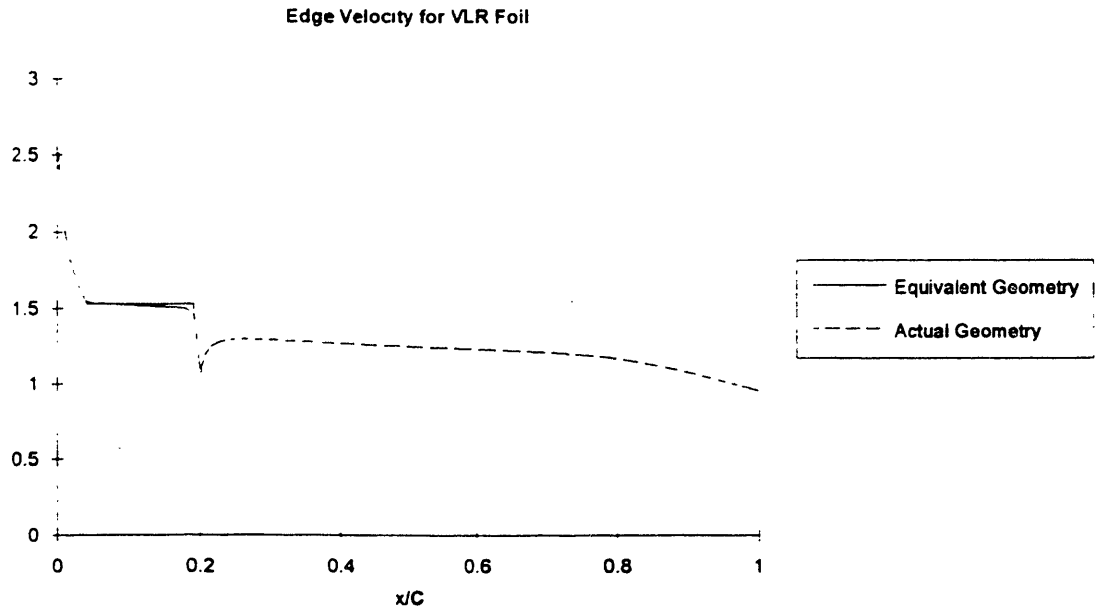

Figure (3-33) Edge velocity validation test results for VLR section with images.

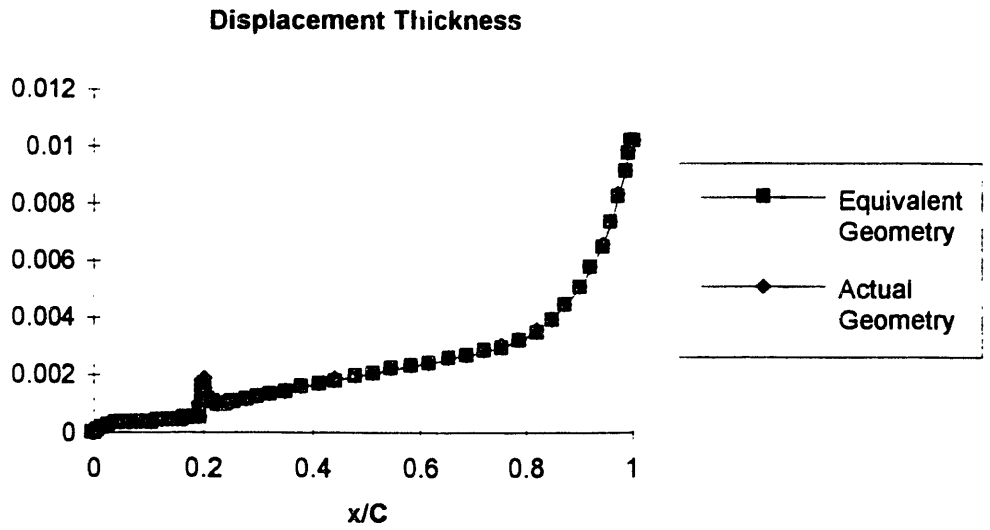

Figure (3-34) Displacement thickness validation test results for VLR section with images.

4. Experimental Studies

A hydrofoil with a VLR cross section was tested at the MIT Marine Hydrodynamics Lab (MHL), using the Variable Pressure Water Tunnel (VPWT). The conditions were such that the flow about the foil was partially cavitating. Experimental objectives were:

1. Measurement of boundary layer profiles for calculation of integral parameters such as displacement and momentum thicknesses.
2. Measurement of drag and lift coefficients.
3. Measurement of cavity velocity and determination of cavity number.

Section 4.1 describes the experimental apparatus and setup. Data measurement techniques are discussed in section 4.2. Experimental procedures are the subject of section 4.3. Data analysis techniques and experimental results are the subjects of sections 4.4 and 4.5, respectively.

4.1. Experimental Setup

The experiment described in this chapter was conducted at the MIT Marine Hydrodynamics Lab. The MHL is equipped with a variable pressure water tunnel, laser doppler velocimeter, and electronic data acquisition systems; all of which were used for this experiment. What follows is a brief description of this equipment and the

experimental setup. For greater detail about the MHL and its facilities, the reader is referred to Kerwin [10].

The original VPWT, which is shown in Figure (4-1), was built in 1928. It stands more than two stories in height, and has a 53 inch 20"x20" test section. The flow speed into the test section, and tunnel pressure are both adjustable. Flow in the loop is driven by an impeller. By means of a vacuum pump, the pressure can be decreased from atmospheric conditions as the need arises. This last feature, makes the VPWT an attractive choice for cavitation experiments.

The flow into the test section is very nearly uniform, with a turbulence level of approximately 1%. Note that this turbulence level is somewhat greater than those of other facilities. However, the areas of interest in the flow for this experiment, such as in the wake of the cavity or in the foil wake, should be turbulent in nature. Therefore, this should not present any major drawbacks.

A closeup of the test section is shown in Figure (4-2). On each side of the test section are large plexiglass windows. These windows allow for flow measurement using the LDV system, as well as flow visualization techniques. Each window is highly polished, and of nearly constant thickness to increase the accuracy of laser measurements.

The hydrofoil used for this experiment was a VLR section (Figure (4-3)). The chord length of the foil was 18 inches, and it had a leading edge radius of .002867 relative to the chord. Maximum foil thickness was 4 percent of the chord length, and thickness at the trailing edge was 0.4 percent of the chord. The foil was machined by Bird- Johnson Co. from aluminum. Its surface was anodized using a gold hard-coat to keep it from reacting with the seed media which is injected into the tunnel during testing. Figure (4-4) shows the foil as it would be mounted in the test section. Gaskets are on either of its sides to prevent cross-flow between the window and foil edge.

Set	Run	α	cm Hg	l/c	σ
A	1	8.00	25.80	0.20	1.31
A	2	8.00	32.50	0.10	4.06
B	1	5.00	14.50	0.36	1.22
B	2	5.00	16.80	0.20	1.28

Table (4-1) Flow conditions for experiment.

4.2. Experimental Procedure

The hydrofoil was installed in the tunnel as described in section 4.1. Water supplied from a storage tank at the MHL facility was used to fill the tunnel. Before any tests were run, the tunnel was dearated for a period of approximately twenty-four hours. This step was necessary to decrease the air nuclei content of the water; thereby, decreasing the amount of bubbles in the flow.

The experiment was performed at two angle of attacks, and a variety of measurements were made at each angle for two different tunnel pressures as shown in Table (4-1). The cavitation numbers shown are computed from the measured velocities. The first angle of attack was 8°. At this angle the pressures were 25.8 and 32.5 cm Hg. The angle of attack was then decreased to 5° for which the pressures were 14.5 and 16.8 cm Hg. At both angles of attack, the tunnel impeller was operated at 300 RPM. This resulted in a free stream speed of 19 ft/s. One additional run was conducted at 8° for a speed of 8.5 ft/s (150 RPM). However, at this speed it was necessary to decrease the tunnel pressure to about 7.75 cm Hg, to produce a stable cavity of less than 10% of the chord length. This low pressure resulted in a high level of bubble cavitation in the tunnel, especially in the wake of the cavity. For these conditions, measurements were to difficult and time consuming, and the run was not completed.

The following measurements were made for each run (a run corresponds to a fixed pressure and angle of attack). First, the cavity detachment and trailing edge points were

measured using the laser. From these measurments one can calculate the cavity length. Then, the horizontal and vertical velocities along a rectangular contour which enclosed the foil were measured. These velocity measurements along the contours were used for force calculations. Two sweeps, each at different chordwise locations dependent upon cavity size, were measured from a point above the cavity to the cavity surface. The measured profiles from these sweeps were used in determining the cavity velocity. Finally, boundary layer profiles at chordwise locations of 0.33, 0.4, 0.6, 0.75 and 0.87, were measured in the wake of the cavity. These boundary layer profiles were used for the calculation of displacement and momentum thicknesses. Both the boundary layer and cavity sweep profiles, were measured in the direction of the local body normal.

4.3. Data Measurement

The MHL facility is equipped with a laser doppler velocimeter, which was used for all velocity measurement. This section gives a brief overview of the LDV system and equipment.

The key feature of laser doppler velocimetry, is that it allows for nonintrusive velocity measurements. This is accomplished by first splitting the laser into individual beams of a single frequency. At the MHL facility, the laser is split into three beams, referred to by their respective colors: green, red and violet. Each beam is used to measure a particular component of velocity: green, is used for horizontal (x-axis) velocity measurements; red, for vertical (z-axis) velocities; and violet, which can be rotated about the y-axis for boundary layer measurements. Note that the beams can be used simultaneously or alone, as need dictates.

A dual beam technique is used for each of the three beams. This technique requires splitting each beam into two beams, and focusing these on a point in the flow at which one wishes to make a measurement. The two beams come together and form an

interference fringe pattern. Particles moving through the fringe pattern scatter light, and this scattered light has a frequency which is different from the incident beams. This change in frequency, referred to as Doppler shift, is proportional to the particle velocity. The Doppler frequency, f_d, is measured using photodetectors. The particle velocity is then calculated using

$$u = f_d \lambda_d / 2\sin(\theta_d)$$

where, λ_d is the wavelength of the incident beam, and θ_d is the half angle for the converging beams. Note that it is necessary to shift one of the beams up by 38 MHz using a Bragg cell. This step is necessary in determining the direction of motion of the particle.

Signals from the photodetectors are processed using TSI IFA-550 Intelligent Flow Analyzers, one for each of the colored beams. The flow analyzer is used to determine if the signal scattered by a particle should be kept or discarded. The acceptance criterion, is that the particle has passed over some minimum number of interference fringes. The minimum number of fringes used for this work is 8. The output from the analyzers is then collected using a PC.

The PC was used for laser positioning and control, and for calculating velocities from the particle velocity measurements. Each velocity measurement at a particular location, is actually the average of many particle velocity measurements

$$u = (1/N)\sum_{j=1}^{N} u_j$$

The number of counts N, varied from about 400-800 above and in the wake of the cavity, to as low as 200-300 points in locations far away from the foil and cavity. Figure (4-5) shows a typical histogram for the streamwise velocity in the wake of the cavity. In this case the mean was 25.8 ft/s with a standard deviation of 0.72 ft/s. The skew and kurtosis for this distribution is 0.160 and 2.9. Figure (4-6) shows a running mean for the same location. These plots, which were available to the experimenter during testing, were used in determining the number of the number of particle counts, N, and the data rate.

The seed media used for this experiment was silicon carbide with a mean diameter of 1.5 μm. It was injected into the flow during testing, and was allowed to mix before measurements were made. In addition to artificial seeding, bubbles advected by the flow also proved to be an effective scatterer. However, this did present some difficulties when the bubbles were large. These large bubbles resulted in boundary layer profiles which had many cusps. In addition the standard deviation of the data tended to be higher when the flow was cavitating.

4.4. Data Analysis Techniques

When examining the results of an experiment, it is not always possible to use measured data directly. Some degree of analysis is sometimes necessary before one can attain some useful information. This section describes the data analysis techniques employed in this study. First, the data smoothing technique which was applied to the boundary layer profiles is discussed. This is followed by a description of the method used for reconstruction of boundary layer profiles from measured data. The section is then concluded with an overview of force coefficient calculations, using the method outlined in Kinnas [11].

When making boundary layer measurements, the profiles obtained included many cusps as shown in Figure (4-7). These profiles would be sufficient for making direct comparisons of boundary layer profiles. However, when reconstructing boundary layer profiles and computing the integral parameters, it was necessary to smooth the data.

A simple exponentially weighted smoothing technique was used. First, the boundary layer is divided into N_J averaging intervals. For the *ith* interval, which has N_i points, the *jth* estimate $\hat{u}_j$ obtained from smoothing, is taken to be given by the following weighted sum of the measured values u_{meas}

$$\hat{u}_j = \sum_{k=1}^{N_i} (u_{meas})_k W_{jk}$$

where the weights are given by

$$W_{jk} = \exp\left[-(r_j - r_k)^2 / l_i^2\right]$$

The weights depend on the distance between each measurement, and some length scale l_i, which depends on the interval chosen. Figure (4-8) shows the results of applying this method to a measured profile. Notice that the desired effect is achieved, while the overall form of the profile is unaffected.

When viewing the smoothed profile of Figure (4-8), it is immediately apparent that the measured profile never reaches a constant value, as one expects of a boundary layer profile. This is due to the influence of the normal pressure gradient for the external inviscid flow. In boundary layer theory this gradient is usually neglected. If one is to calculate quantities such as displacement and momentum thicknesses, it becomes necessary to remove this influence and reconstruct a boundary layer profile.

The author chose the method described in Zierke and Deutsch [26]. In this method, the measured profile is assumed to be a composite of the inviscid profile, boundary layer profile and a matching constant. This can be written as

$$u_{meas} = u_{bl} + U_{inv} - U_e$$

However, the constant edge velocity U_e and the inviscid profile U_{inv} are unknown. Using the fact that both the measured and boundary layer profiles go to zero at the body surface, the edge velocity can then be obtained from

$$U_e = (U_{inv})_{wall}$$

The inviscid profile must be obtained in some manner from the data. If one assumes viscous effects are negligible far from the wall or body surface, the measured profile can be assumed to approximate the inviscid profile. The main difficulty lies in choosing at which point the viscous effects should be assumed negligible. Following Zierke and Deutsch [26], the point is taken to be where the slope of the measured profile

changes by at least 50%. The data from this point to the furthest measured point from the wall, is then fit using a least squares technique. This fitted profile is then extrapolated to the wall so that the edge velocity can be determined.

Some results from this method of boundary layer reconstruction are shown in Figures (4-9) and (4-10). In both cases the inviscid profile is fit using a linear expression. The method was also tested with a quadratic polynomial, which resulted in a slightly lower edge velocity. However, the boundary layer profiles were very similar in form. The point at which the inviscid profile was started from, was also varied without much effect on the reconstructed profiles.

One of the objectives of this experiment was the determination of forces and their associated coefficients. However, with the configuration as described in section 4.1, it was impossible to measure these directly. A method of obtaining these coefficients indirectly, using the momentum flux formulation due to Kinnas [11], was used for this work.

The first step in this method, is the measurement of the horizontal and vertical velocities along a rectangular contour which encloses the foil. A typical contour or box is shown in Figure (4-11). The free stream velocity U_∞ is taken to be the average of the horizontal flow upstream from the foil. It is convenient to define the perturbation velocity

$$u' = u - U_\infty$$

Assuming that:

1. Boundary layer effects at the walls are negligible.
2. $v << U_\infty$ at the upstream and downstream sides of the box.
3. $u' << U_\infty$ at the top and bottom of the box.

Kinnas [11] has shown that the lift and drag coefficients are given by

$$C_L = \rho U_\infty \Gamma$$

and

$$C_D = 2\int_{y_{BW}}^{y_{TW}} \Delta u_R dy - 2\int_{y_{BW}}^{y_{TW}} (\Delta u_R)^2 dy$$

where x and y have been non-dimensionalized by chord length, and Γ is the circulation around the foil. Note that the expression for the drag coefficient is correct to second order in Δu_R, the dimensionless wake defect. Given the velocity measurements along the contours and the free stream velocity, the integrals above are computed numerically allowing for the determination of C_L and C_D.

4.5. Comparison of Numerical and Experimental Results

The method of Chapter 2, provides a means for analyzing viscous, cavitating flow. It is natural at this point to ask, does the method agree with experimental observations, at least in the gross sense? The purpose of this section, is to describe comparisons between numerical predictions and experimental observations. The aim of these comparisons is to address this question.

When making comparisons of numerical and experimental results, only the gross flow parameters were compared. The reason for this is that the present method is not meant as a tool for the detailed analysis of the flow structure. The gross parameters that will be compared in this section, are the integral parameters δ^* and θ, and the lift and drag coefficients. The experimental force coefficients are computed using the method of Section 4.4. Integral parameters are computed by numerically integrating the reconstructed boundary layer profiles. The reconstruction of boundary layer profiles is discussed in Section 4.4.

Before presenting the comparisons, one further issue needs to be addressed. What would give rise to any differences between the numerical and experimental results? In the

		Experimental		Numerical	
Set	Run	Lift	Drag	Lift	Drag
A	1	1.361	0.028	1.468	0.031
A	2	1.356	0.016	1.438	0.015
B	1	0.882	0.019	0.926	0.018
B	2	0.861	0.011	0.883	0.010

Table (4-2) Comparison of force coefficients.

development of the numerical model, several fundamental assumptions were made. As a result, several flow effects were neglected. Some of these effects which are neglected, do tend to have a weak influence on the solution. However, a few of the effects which are neglected, can have a strong influence, and possibly be of the same order as those effects which have been retained One such effect, is the mass flux between the cavity and external flow In the numerical model, mass flux through the interface due to a change of phase, is taken to be zero. The other effect which is important, is the unsteadiness of the flow. This latter effect is important, for cavity pressure depends quadratically on the flow velocity. In this section, no attempts will be made to quantify these effects. This will be done in Chapter 5 However, the reader should take these effects into consideration, when interpreting the results of the following comparisons.

The results from the numerical code were computed under the following conditions. In each case, 120 panels were used to approximate the foil surface, and the angle of attack was taken to be the same as the measured value. The walls were modeled using ten image pairs. The detachment point and cavity length used for the computations, were taken to be equal to the measured values for these quantities. The pressure was taken to vary quadratically in the pressure recovery zone, and the transition length was

varied until the computed cavity number equaled the measured value. The relative tolerances used in the numerical computations were set at $\Delta q_c = \Delta U^{cte} = \Delta m^c = 10^{-5}$.

The edge velocity distributions, which were computed using the numerical code, are shown in Figures (4-12), (4-15), (4-18) and (4-21). In each of these figures, we see that the dynamic boundary condition has been satisfied for the specified tolerances. One point of interest in each of these figures, is that the cavity velocity is not the maximum velocity on the suction side. The maximum occurs somewhat upstream of detachment. In terms of pressure, this means that the cavity velocity is not the minimum pressure. This agrees with the experimental observations of Franc and Michel [6]. The velocities computed at the trailing edge of the cavity ranged from between 30 to 67 percent of the cavity velocity

The comparisons for the displacement thicknesses, are shown in Figures (4-13), (4-16), (4-19) and (4-22) In each case there are kinks in the computed displacement thickness distributions at the cavity detachment point and cavity trailing edge. Note that the boundary layer grows as it approaches the cavity trailing edge, and then decays and resumes growth in the cavity wake. The experimental results to compare favorably with the computed results. In general, the differences are greatest near the cavity trailing edge. This can be attributed to the complex nature of the flow in this region. However, we see from the displacement thickness results, that the pressure recovery model is adequate in terms of approximating the boundary layer growth.

Figures (4-14), (4-17), (4-20) and (4-23), show the results of the momentum thickness distribution comparisons. We see from these figures that the differences between experiment and computation are greater than those found in the displacement thickness comparisons. However, these differences are again greatest near the cavity trailing edge. Again we find that the momentum thickness rises to a local maximum at the cavity trailing edge, and then decays and begins to grow again in the wake of the cavity. As was the case in the displacement thickness comparisons, the pressure recovery model

does seem to adequately predict the growth of the momentum thickness. Although, in the cavity trailing edge region, by neglecting mass flux due to phase change and unsteadiness, results in larger differences near the trailing edge.

The comparison of the force coefficients, C_L and C_D, is shown in Table (4-2) for each of the test cases. The experimental coefficients were calculated using the method described in Section 4.4. In all cases, the lift coefficients from the numerical code were larger than those from experiment, and the numerical drag coeffcients were smaller than the experimental ones. The largest differences, about 7% for C_L and 5% for C_D, were found at the angle of attack of 8° (Set A). The reader is reminded that for this angle of attack, there were large deviations in the LDV measurements due to the high bubble content of the water. The experimental force coefficients calculated by the method of Section 4.4, are highly sensitive to these deviations of the measured velocities.

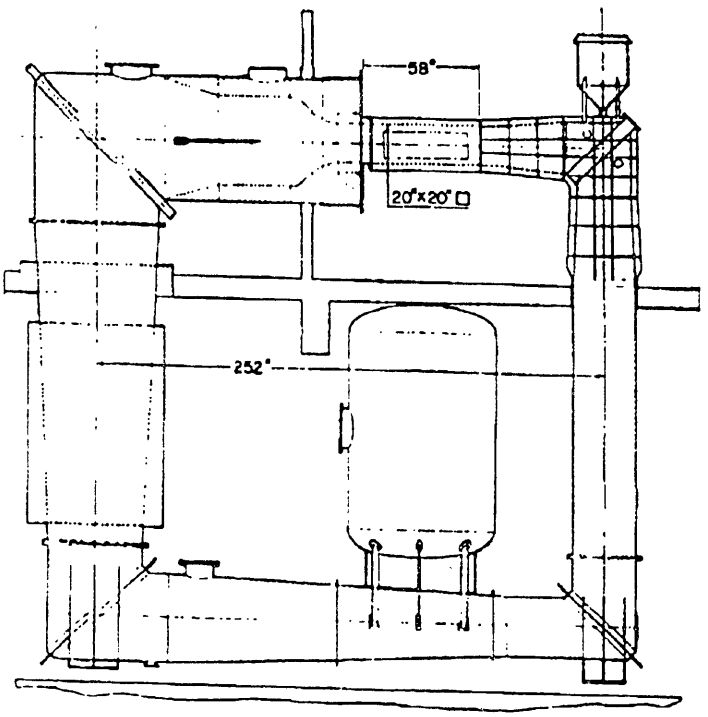

Figure (4-1) The variable pressure water tunnel at the MIT Marine Hdrodynamic Lab from Kerwin [10]

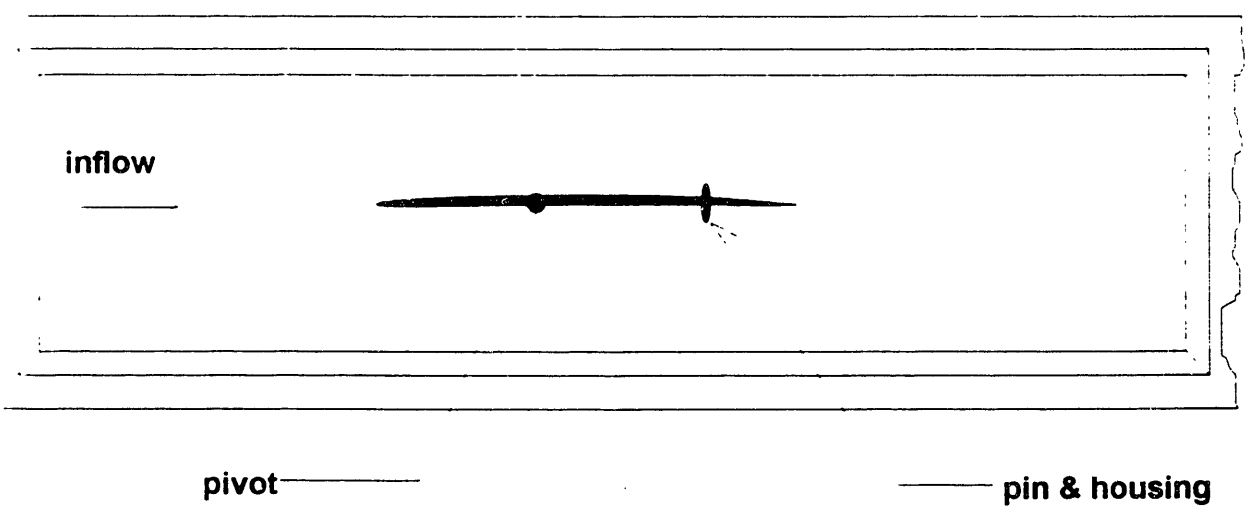

Figure (4-2) MHL test section.

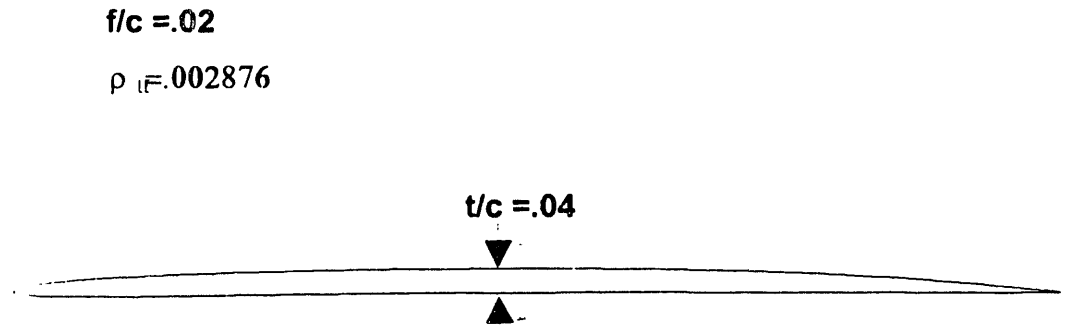

Figure (4-3) VLR foil cross section.

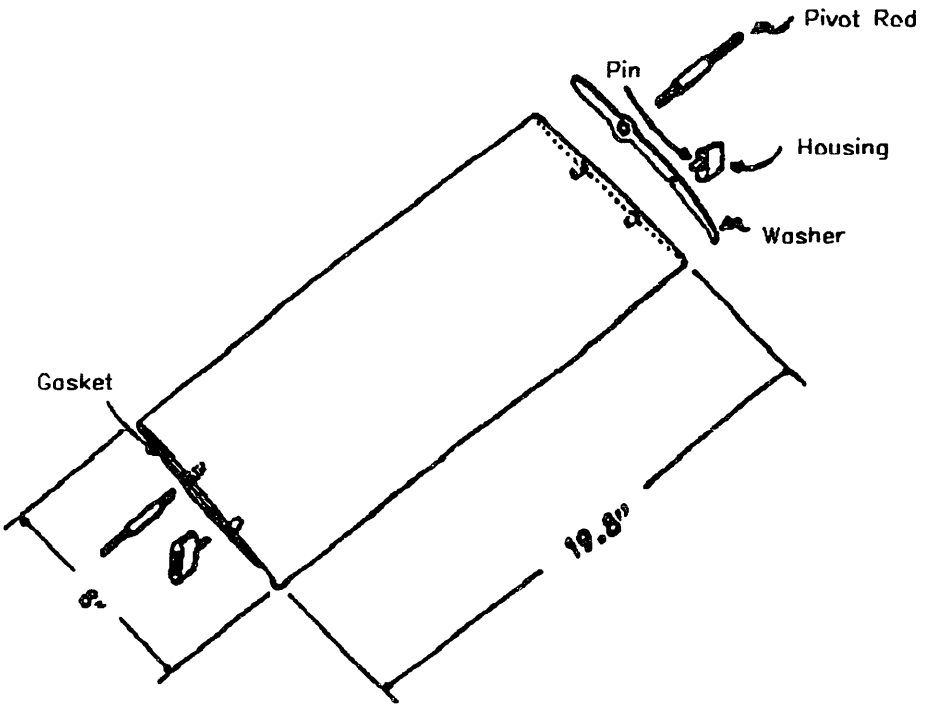

Figure (4-4) Foil configuration from Kinnas [11].

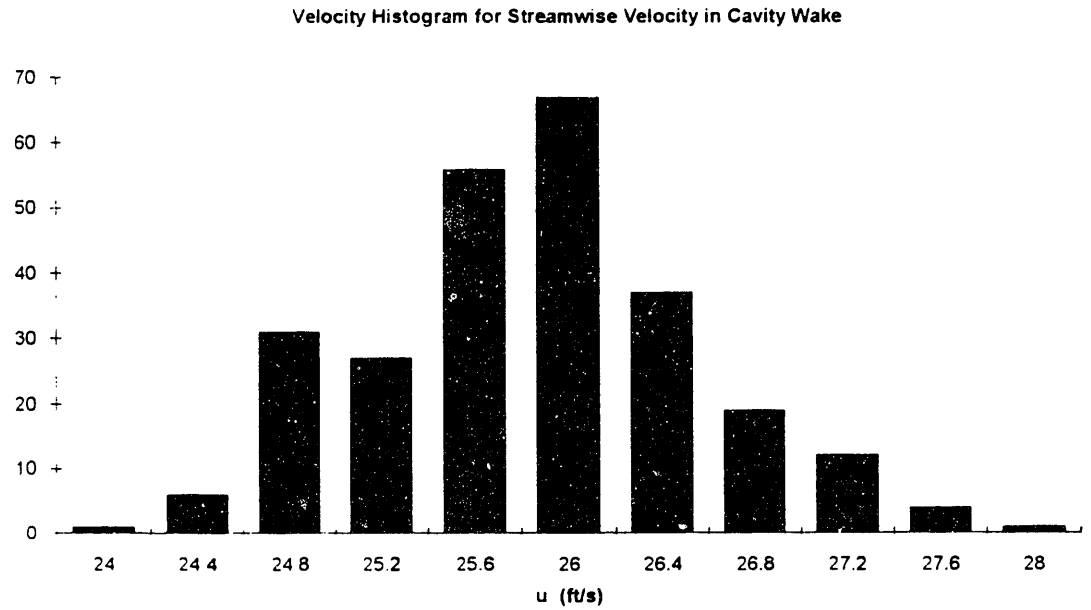

Figure (4-5) Velocity histogram for streamwise velocity in cavity wake.

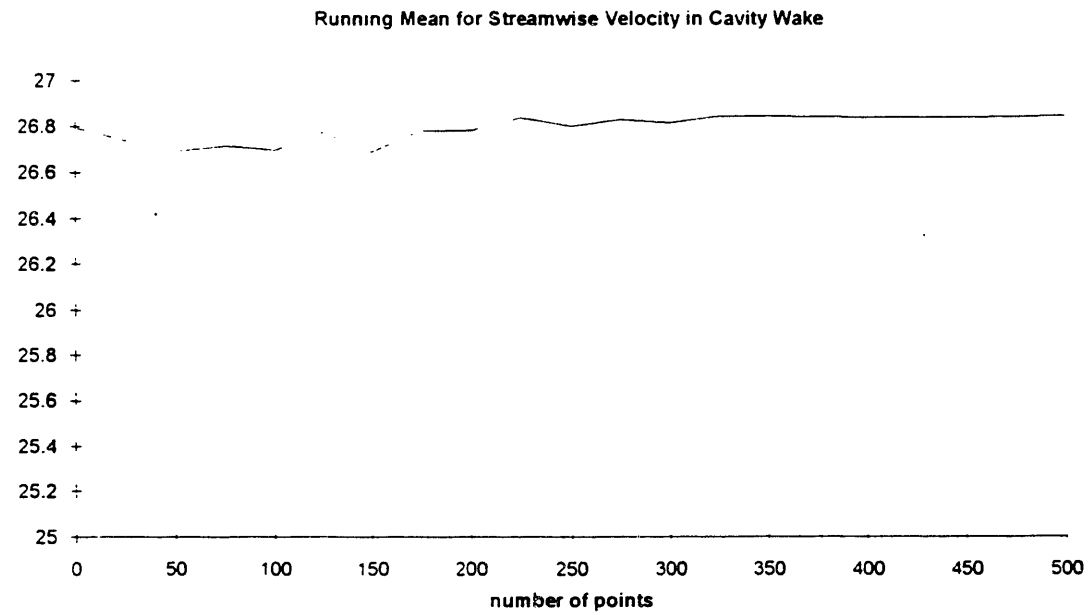

Figure (4-6) Running mean from LDV measurement.

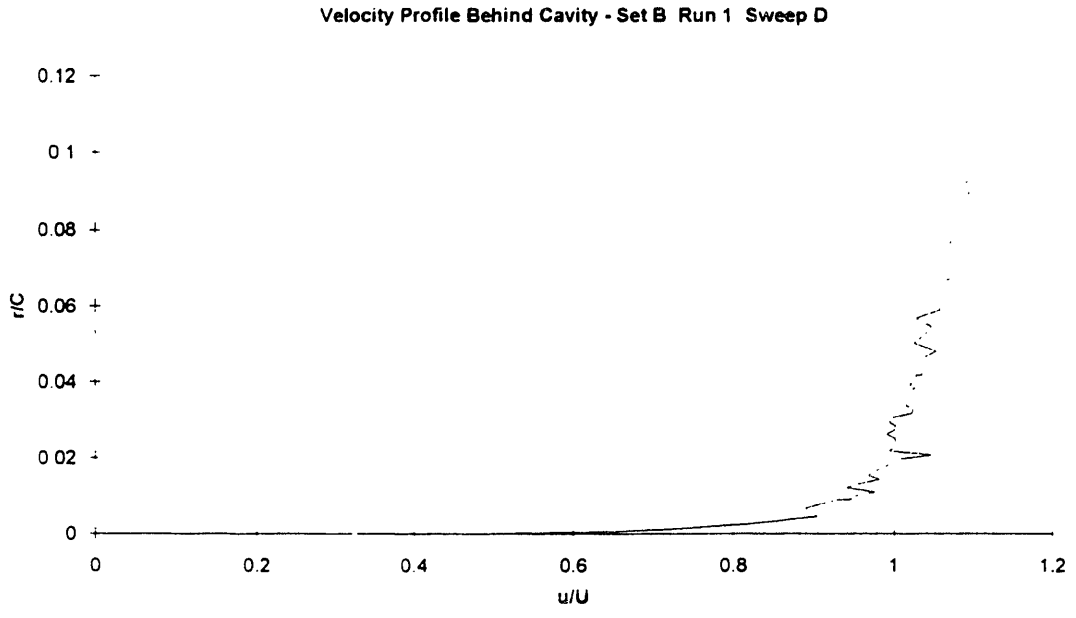

Figure (4-7) A typical boundary layer profile before smoothing.

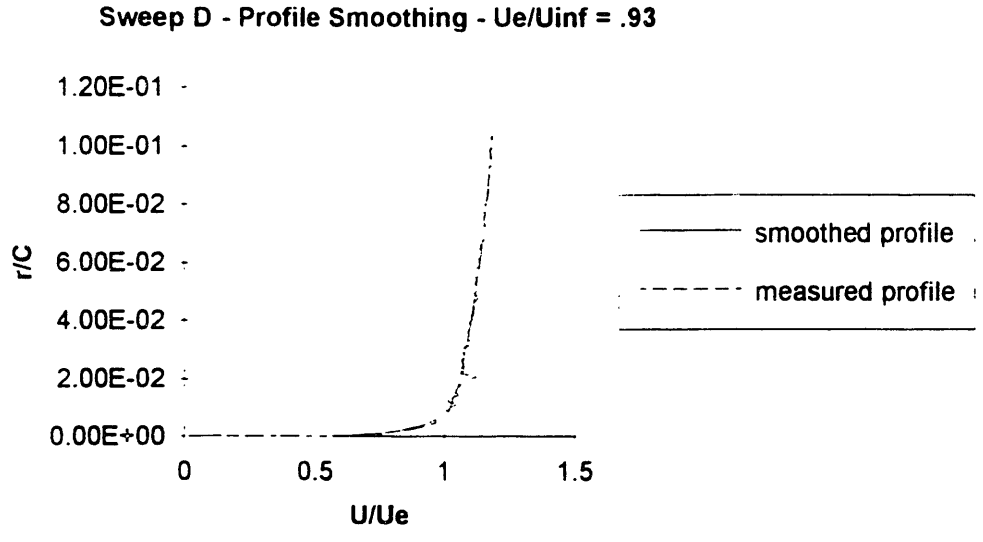

Figure (4-8) A typical boundary layer profile before and after smoothing.

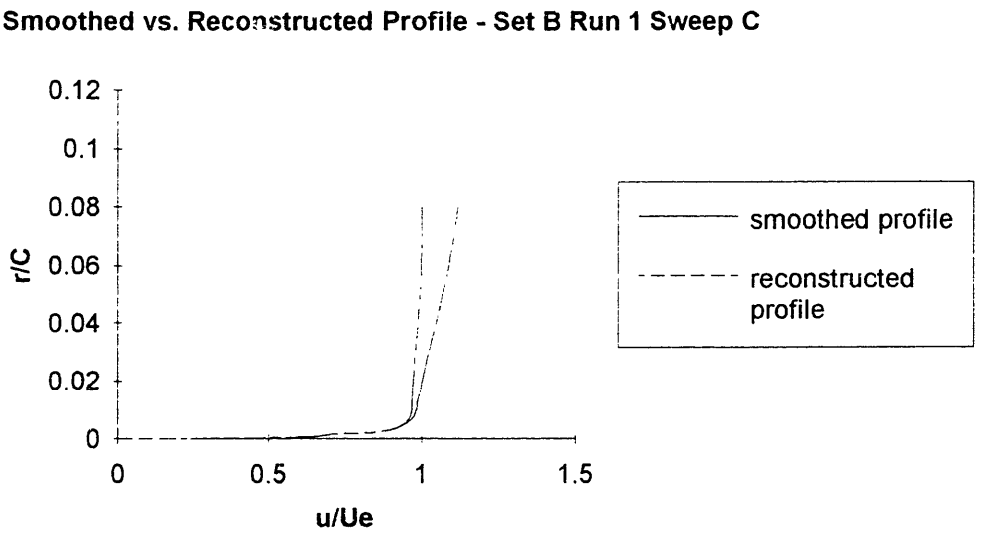

Figure (4-9) Results of boundary layer reconstruction for velocity sweep C run 1.

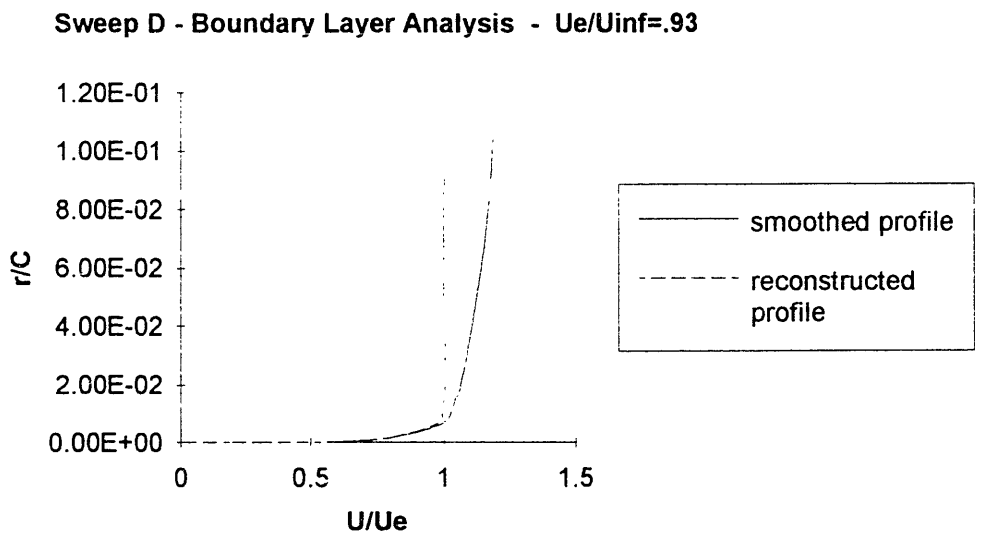

Figure (4-10) Results of boundary layer reconstruction for velocity sweep D run 1.

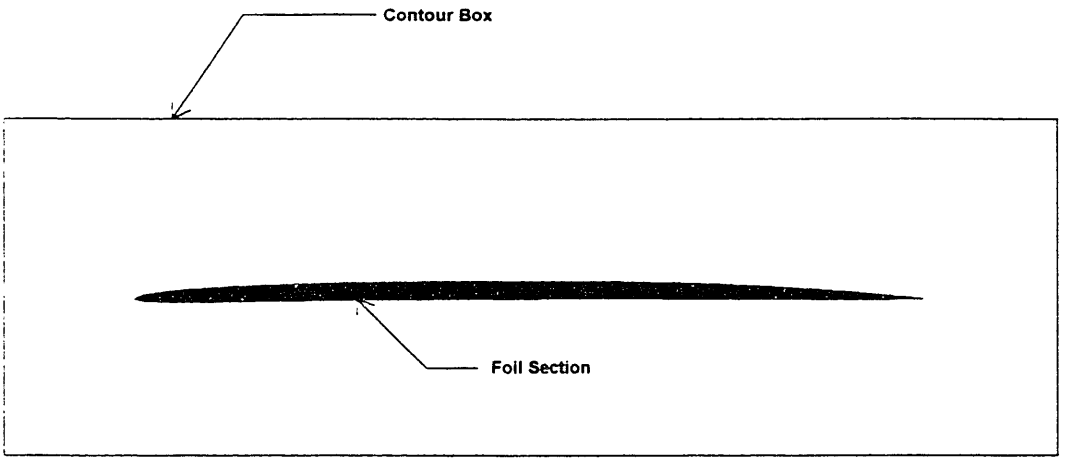

Figure (4-11) A typical contour box for flow velocity measurements.

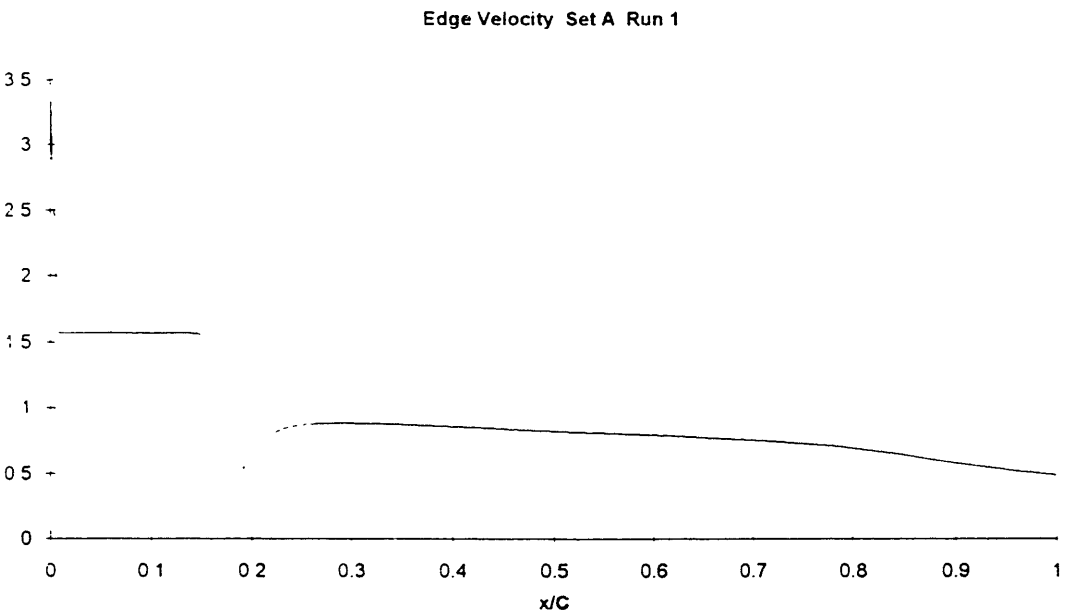

Figure (4-12) Edge velocity for Set A Run 1.

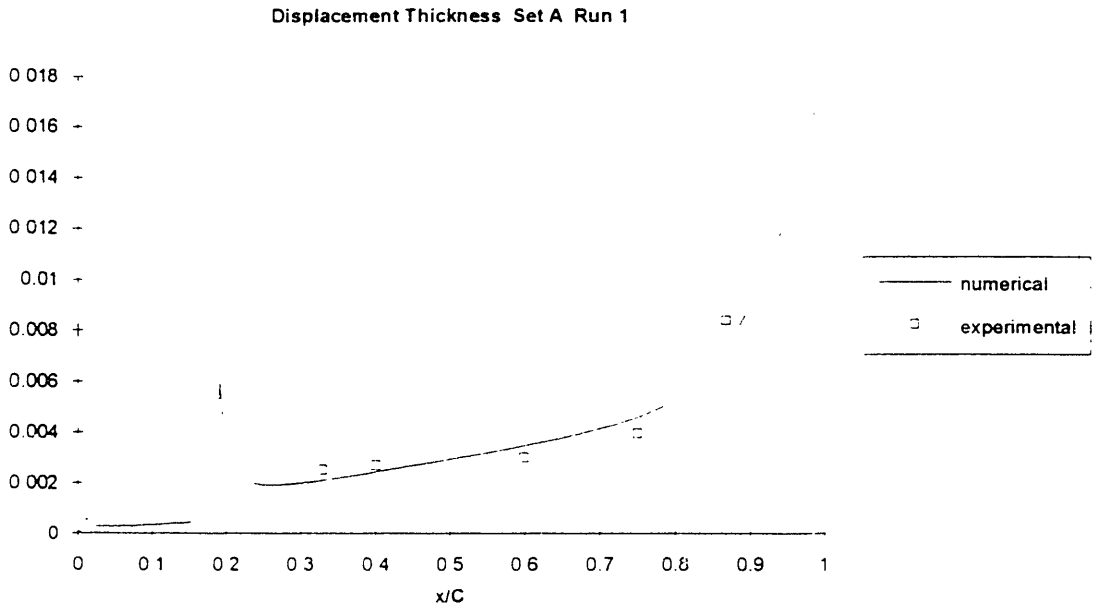

Figure (4-13) Displacement thickness for Set A Run 1.

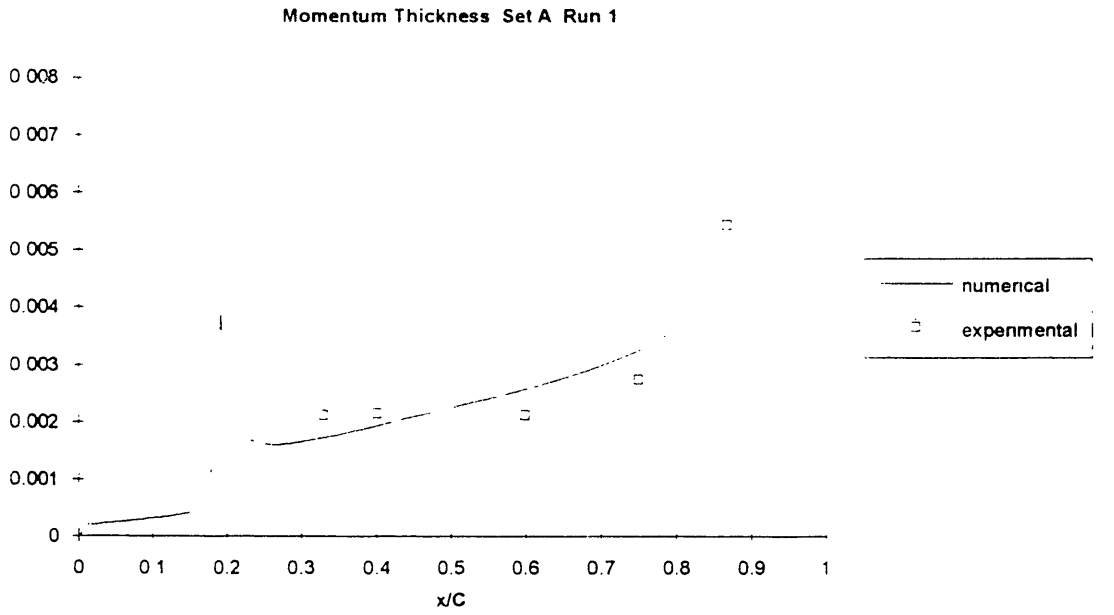

Figure (4-14) Momentum thickness for Set A Run 1.

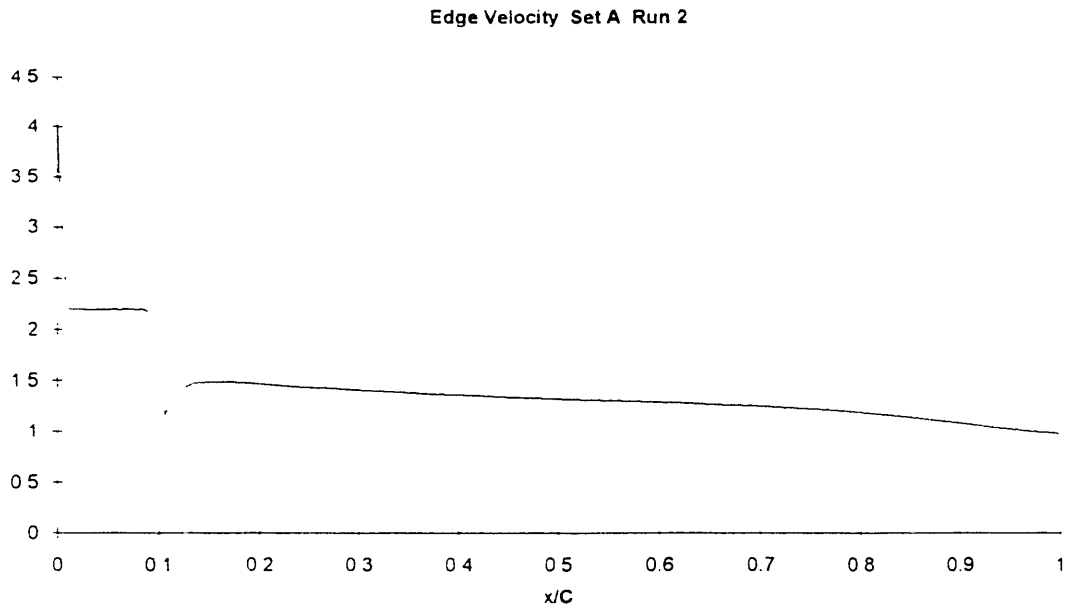

Figure (4-15) Edge velocity for Set A Run 2.

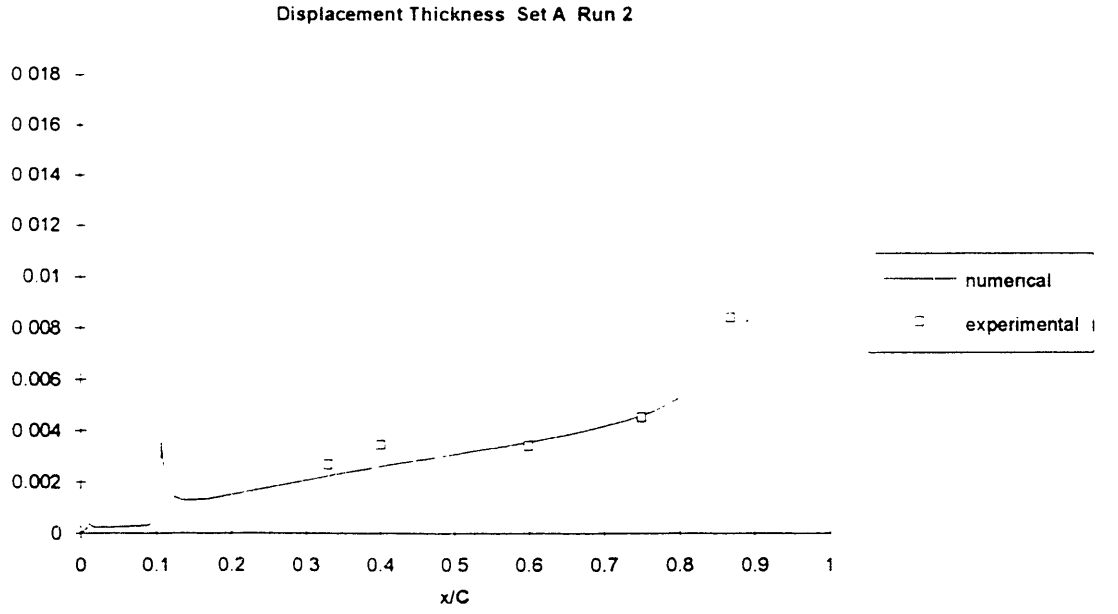

Figure (4-16) Displacement thickness for Set A Run 2.

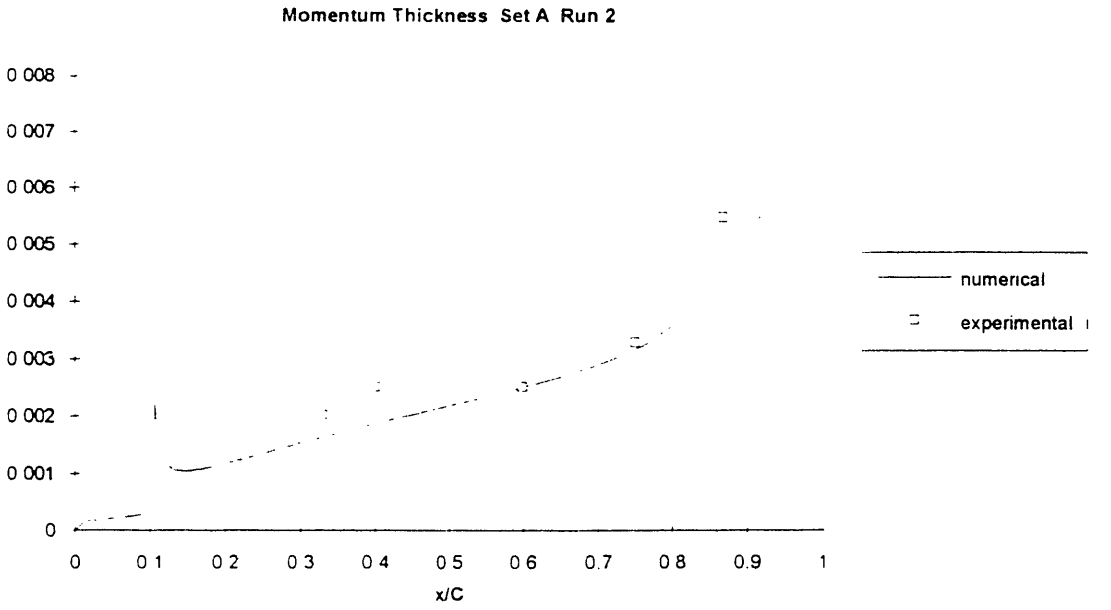

Figure (4-17) Momentum thickness for Set A Run 2.

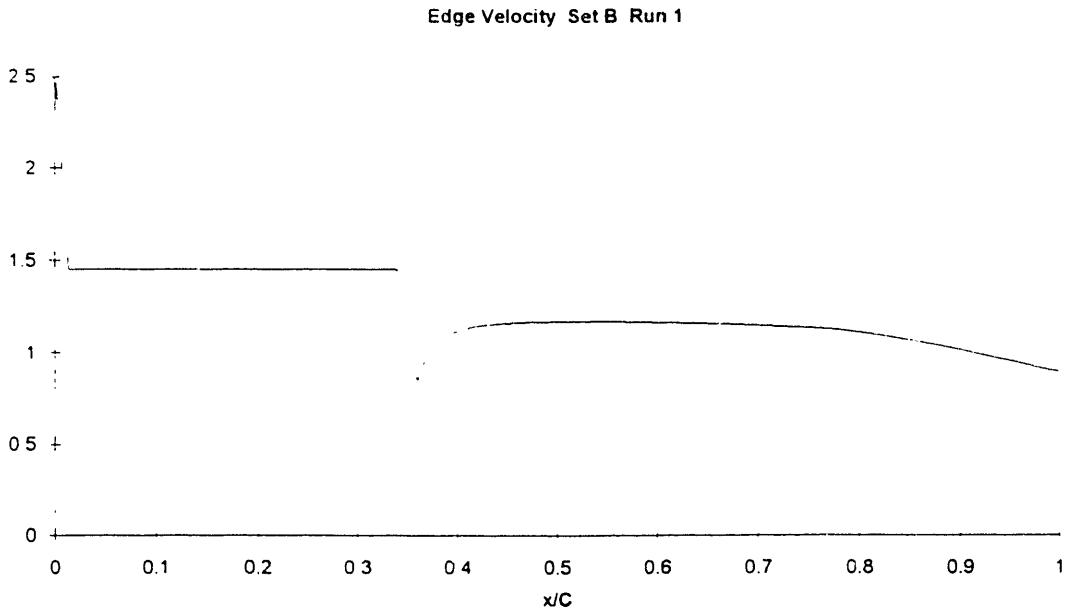

Figure (4-18) Edge velocity for Set B Run 1.

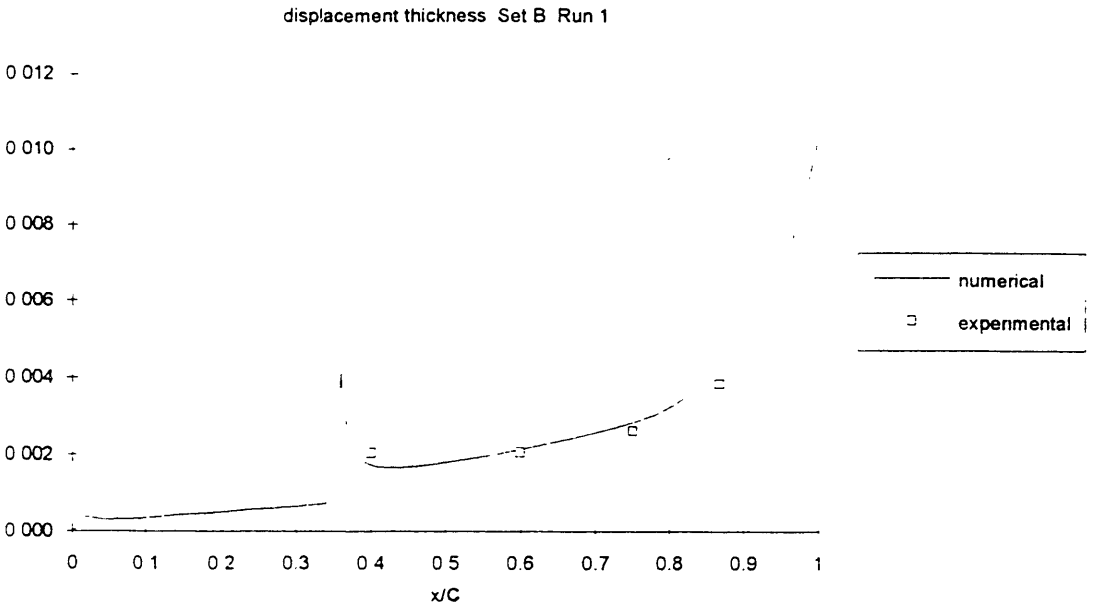

Figure (4-19) Displacement thickness for Set B Run 1.

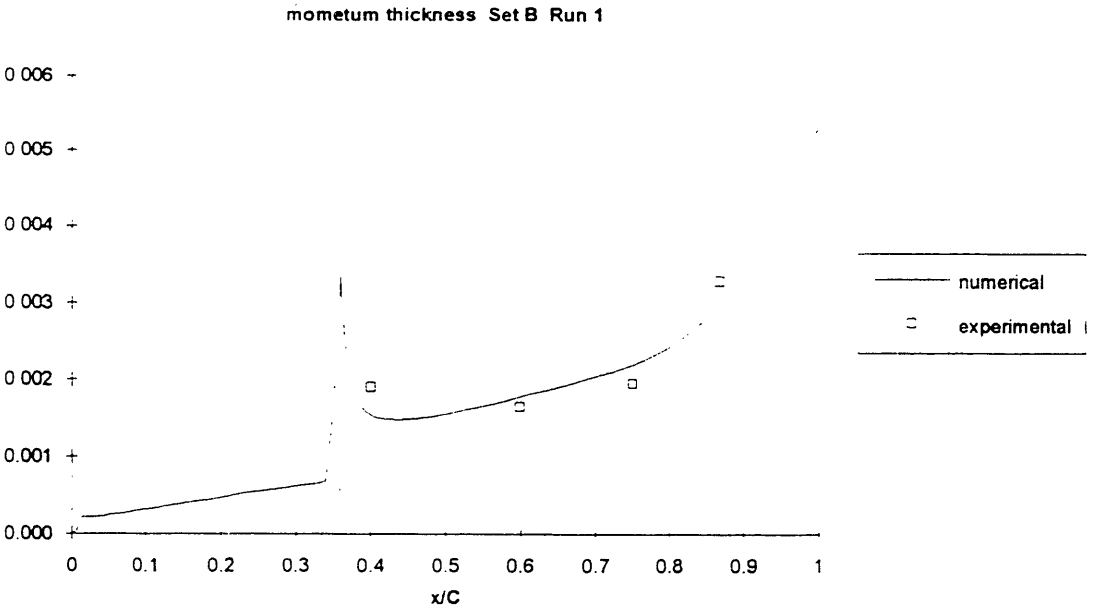

Figure (4-20) Momentum thickness for Set B Run 1.

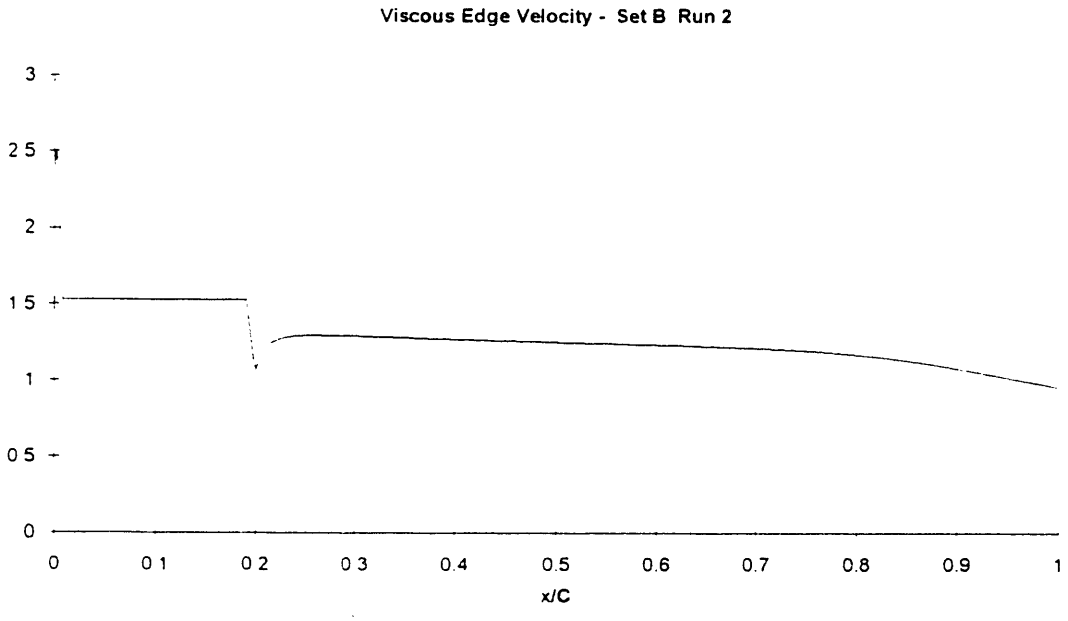

Figure (4-21) Edge velocity for Set B Run 2.

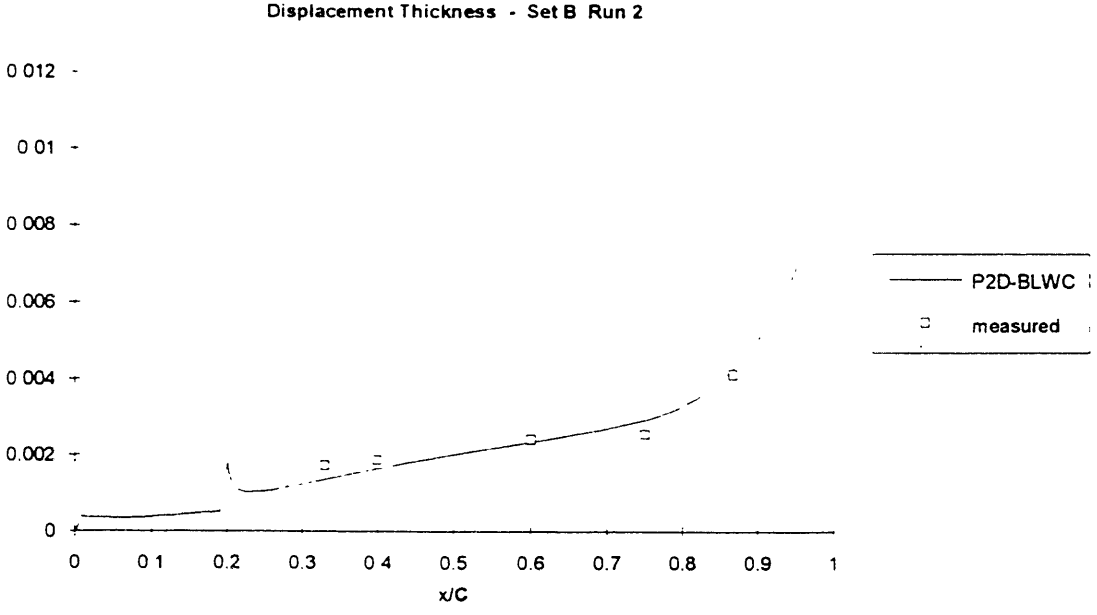

Figure (4-22) Displacement thickness for Set B Run 2.

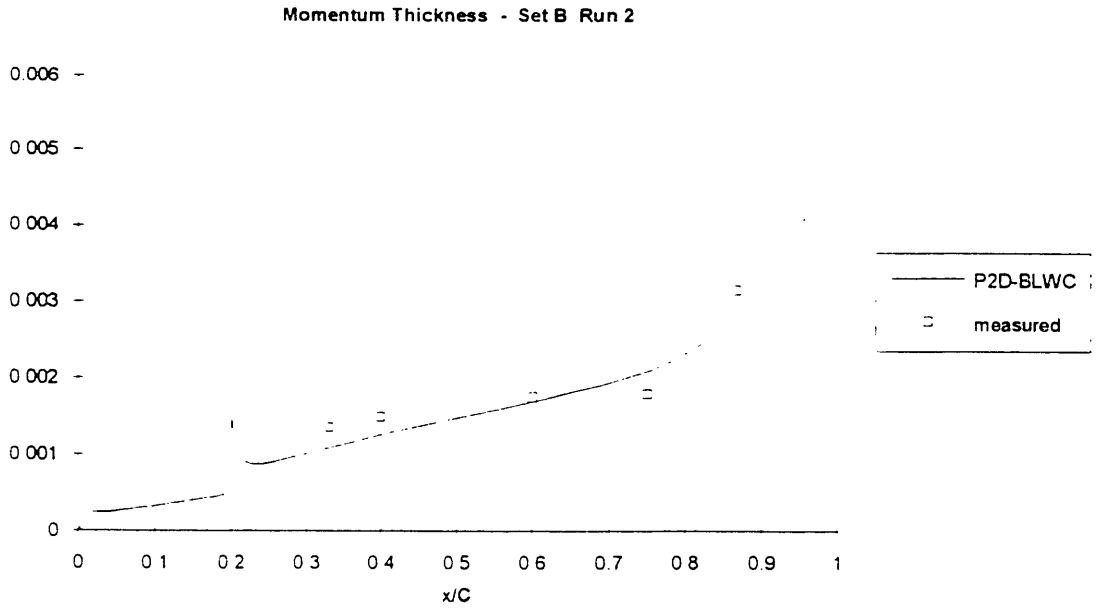

Figure (4-23) Momentum thickness for Set B Run 2.

5. Conclusions

In the previous chapters, a method for the analysis of viscous, cavitating flow was presented. At this point one may ask, how does the inclusion of the boundary layer influence cavity parameters? This question is addressed in Section 5.1 of this paper. In contrast, two effects which have been neglected, namely mass flux and unsteadiness, are investigated briefly in Section 5.2. The intent is to understand how these effects influence cavity parameters such as length, pressure or height. Finally, the paper closes with some recommendations for future work, in Section 5.3.

5.1. Effects of Viscosity on Cavitation

The method described in this paper, provides a means for the analysis of viscous cavitating flow around a hydrofoil. This tool allows us to address one more issue, that is the effects of viscosity on cavitation.

The addition of viscous effects, by means of the boundary layer, should indeed have some influence on the cavitating flow. To gain some measure of this influence, it becomes necessary to compare the inviscid cavitating flow with the viscous cavitating flow for the same conditions. This was completed for the present work as follows. First, the viscous cavitating flow was analyzed, and from this resulted a corresponding lift force and cavitation number. The inviscid cavity flow case was then run, and the angle of attack and

$(l/c)_{vis}$	Δl %	Δh %	$\Delta\alpha$ %
0.16	21	44	16
0.27	14	25	14
0.37	21	42	19

Table (5-1) Viscous effects on cavity parameters for the NACA0010 foil.

cavity length were varied until the lift and cavitation numbers obtained, matched those for the viscous case. The comparison is made for constant lift conditions, to avoid any differences due to the reduction in lift by the addition of the viscous boundary layer. Also from a designers point of view, these two conditions are those which would need to be specified.

Figure (5-1) shows the results of a study for the above conditions using a NACA0010 foil. The viscous cases were all run at a constant angle of attack of 2°, for the following cavity lengths: 0.16; 0.27; 0.37. Table (5-1) summarizes the results of Figure (5-1). The percent change in the cavity length, maximum cavity height, and angle of attack are shown for each length. Note that these are all percent decreases. What happens is that for a constant length, the addition of viscous effects reduces the cavity velocity and the cavitation number. To account for this one needs to increase the cavity length for the corresponding inviscid case. However, by increasing the cavity length, one increases the lift so it becomes necessary to decrease the angle of attack. Reduction of the angle of attack while holding the cavity length constant, results in a larger cavitation number, so it becomes necessary to further decrease the cavity length. One can continue iterating in this way, until the results above are obtained. This heuristic argument demonstrates why the percent changes are negative.

The results of another test case, similar to the one above, is presented here to show that the above results are not just mere aberrations for that particular configuration. The

foil used in this case was the VLR section used for the experiment described in Chapter 4. The results are presented in Figure (5-2). The viscous runs were carried out at an angle of attack of 5°, and the cavity lengths were 0.2, 0.3 and 0.4. Again, the percent changes shown are decreases in the viscous cavity parameters. The arguments used above apply here as well. Note that while the percent decreases in the cavity length and angle of attack were close in value, the changes in maximum cavity height were much different and always larger.

To aide in understanding what is happening above, we can examine the relationship of the cavity length to the parameter α/σ. This relationship is shown in the form of the graph of Figure (5-3). The curves presented are for the NACA0010 foil. One curve corresponds to inviscid cavity flow, the other is viscous cavity flow. With the aide of this figure. we can repeat the heuristic arguments above to more clearly demonstrate the viscous influence on the flow. From this chart we see that for the same value of α/σ, the inviscid cavity will be larger than the viscous cavity. As a result, the larger inviscid cavity will have more lift. To decrease lift and match the design condition, one can decrease the angle of attack while holding the length constant. However, by doing this the cavitation number increases. To match the design condition, it becomes necessary to decrease the cavity length. The result is a shorter cavity, with less volume.

The curves shown in Figure (5-3) are for two different Reynolds numbers: 10^6; 10^7. From this graph we see that as the Reynolds number is increased, the cavity length calculated using the present method, approaches the inviscid result for the same value of α/σ. The reason for this is that as the Reynolds number is increased, the boundary layer becomes thinner. This thinner boundary layer has a weaker influence on the cavity, so the solution approaches the inviscid solution.

$(l/c)_{vis}$	Δl %	Δh %	$\Delta\alpha$ %
.2	12.5	28	8
.3	8	60	11
.4	6	15	11

Table (5-2) Viscous effects on cavity parameters for the VLR foil section.

5.2. Effects of Unsteadiness and Mass Flux

In this section the effects of unsteadiness, and mass flux between the cavity and external flow, are considered briefly. The aim here is to get some estimate as to what degree these factors influence the solution. Note that in the present method, these effects are neglected.

In reality, the flows of interest here are inherently unsteady. This unsteadiness results in fluctuations of the cavity pressure, and therefore cavity length. Extending the present method to account for this effect is beyond the scope of this work. However, an estimate of how these effects influence the solution can be obtained by using a quasi-steady analysis. In such an analysis the cavity pressure is assumed to oscillate sinusoidally about some mean. The resulting cavitation number is

$$\sigma = 1.15 + 0.07\sin(\omega t) \tag{5-1}$$

where the magnitude of the perturbation has been approximated from the data of Chapter 4. For the quasi-steady analysis, the unsteady effects are accounted for by the change in cavitation number. All time derivatives are taken to be zero. Figure (5-4) shows the results of this analysis for the following cavitation numbers: 1.08; 1.15; and 1.22. These numbers correspond to the minimum, mean, and maximum, respectively. The foil used was a NACA0010 at an angle of attack of 5 degrees. As Figure (5-4) shows, there are

large deviations in the length of the cavity for the different cavitation numbers. The magnitude of the deviation of the cavity number was 6%, which resulted in a maximum deviation in length of 15%. Such estimates demonstrate that the effects of unsteadiness are very important, and should be included to make the model more accurate.

In the free-streamline model presented here, mass flux due to phase change has been neglected. In reality, there is a mass flux between the cavity and external flow over the entire interface due to evaporation and condensation. Modeling this mass flux would be very complicated, and accounting for it is beyond the scope of this work. However, we can estimate the influence that this mass exchange would have on the flow in a much simpler manner. In the present work, the cavity is assumed to close on the foil. The term close implies that the cavity height is zero at the trailing edge, and there is no mass flux. The transition zone at the trailing edge of the cavity, where the flow is turbulent and two phase, is modeled using pressure recovery as described in Chapter 2. The pressure recovery model allows for recompression near the trailing edge, but neglects the mass flux there. Instead of using pressure recovery, we can assume that there is some finite mass flux between the cavity and external flow. This mass flux would give rise to a pressure jump at the trailing edge interface due to condensation of the water vapor. The jump in pressure coefficient which is defined as

$$\Delta C_p = q_c^2 - q_c^2(s) \tag{5-2}$$

is given by

$$\Delta C_p = 2\gamma_v u_v (u_v - u_l) \tag{5-3}$$

where γ_v is the specific gravity of the water vapor which is taken to be 10^{-4}. The normal velocities at the interface for the vapor and liquid are denoted here as u_v and u_l respectively. Applying the equation for mass conservation gives

$$\gamma_v = u_l / u_v \tag{5-4}$$

or

$$u_v >> u_l \tag{5-5}$$

The vapor velocity can then be approximated as

$$u_v(s) = \sqrt{\Delta C_p(s)/2\gamma_v} \tag{5-6}$$

Mass flux from vapor to liquid is given by

$$m = \int_{S_\lambda}^{S_{CTE}} \gamma_v u_v ds \tag{5-7}$$

where the mass flux has been nondimensionalized by $\rho U_\infty c$. The objective here is to estimate the influence of this mass flux on the solution, and compare it with viscous effects. So when making the comparisons, first the viscous model was used to compute the mass flux at the cavity trailing edge and the pressure distribution. Based on the viscous pressure distribution, equation (5-7) was integrated to give the mass flux. Figure (5-5) shows the mass flux resulting from this analysis plotted versus the magnitude of the pressure increase. As this plot shows, the estimated mass flux is always smaller than the mass flux associated with the viscous model. However, the estimated flux is not a negligible quantity especially for large pressure changes which correspond to longer cavities. While this analysis provides only a very rough estimate of the mass flux, it does demonstrate the importance of the mass exchange.

5.3. Conclusions and Recommendations

Presented in this thesis is a method for the analysis of cavitation about hydrofoils in steady viscous flow. The method is based on a low order perturbation potential formulation. Viscous effects are accounted for by means of a boundary layer. Coupling of the viscous boundary layer and inviscid cavity flow is accomplished through the use of blowing sources.

The method was shown to be convergent. The Newton scheme used in satisfying the dynamic boundary condition on the cavity, need very few iterations to attain a reasonable tolerance on the cavity height and cavity velocity. Comparison of the results with those from experiment, were in general favorable. The numerical results showed the same general trends as those from experiment. However, differences near the trailing edge of the cavity are due to problems in the modeling assumptions in this region.

The addition of the viscous effects were shown to have a strong effect on the cavity, and those parameters which characterize it. It was shown that the effect of including the boundary layer, while maintaining a constant cavity length and angle of attack, was to decrease the cavity velocity. This decrease in cavity velocity, resulted in larger changes in the cavitation number. The cavitation number decreased as did the volume. The influence of viscous effects for constant design conditions, was also demonstrated. It was shown that for constant lift and cavitation number, large differences in volume, length and angle of attack occurred between the inviscid and viscous solutions.

While the method presented herein, may provide a useful tool for the analysis of viscous cavitating flow, it is only a beginning. A great many assumptions were made in its development. Some of these assumptions are nearly always approximately satisfied by the actual flow. However, a few assumptions are made either to make the problem more tractable, or because there is just not enough known about the details of the flow. If one assumes there is an interface between the sheet cavity and external flow, it would be necessary to account for mass flux through this interface due to phase change. This interface of course is always moving, so the problem really is by nature unsteady. Near the trailing edge of the cavity, the concept of the interface breaks down, because the flow there is highly unsteady and of multiphase. In addition, this turbulent multiphase flow is inherently three dimensional. Future efforts in this area should take into account these effects. However, before one can attempt this in a model, it would be necessary to gain more insights into the details of the flow through experimentation.

The present method does allow for the analysis of cavitating flow, with the inclusion of boundary layer effects. This method allows one to estimate those gross parameters which are important to designers of propellers or turbomachinery. Obtaining estimates in this way is more inexpensive than either model testing, or fully three dimensional two phase numerical flow models. However, as with any model, one must take into account the assumptions made in its development, when interpreting the numerical results.

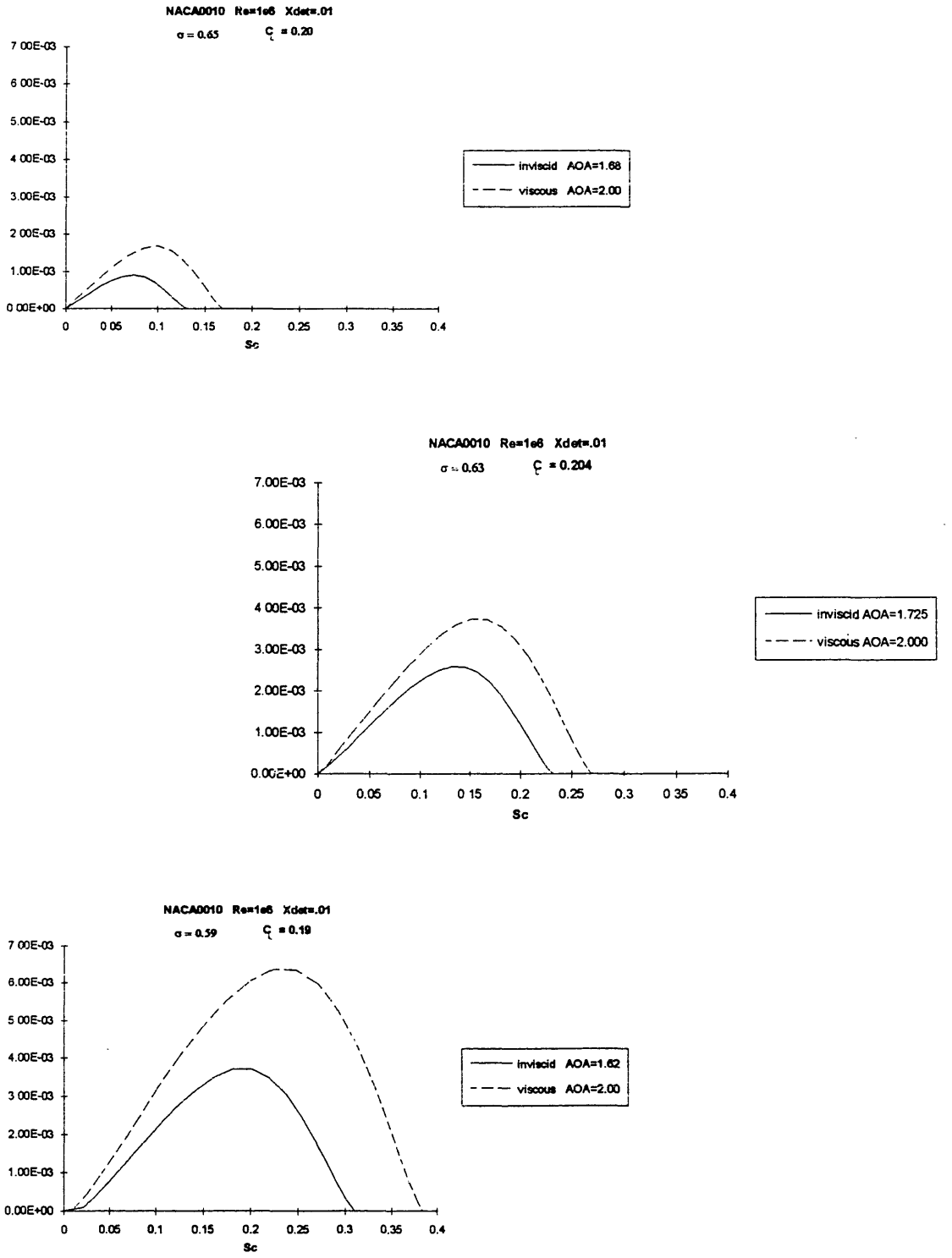

Figure (5-1) Comparison of inviscid and viscous cavity height distributions for the same cavitation number and lift coefficient for a NACA0010, at three different cavity lengths ($Re=10^6$).

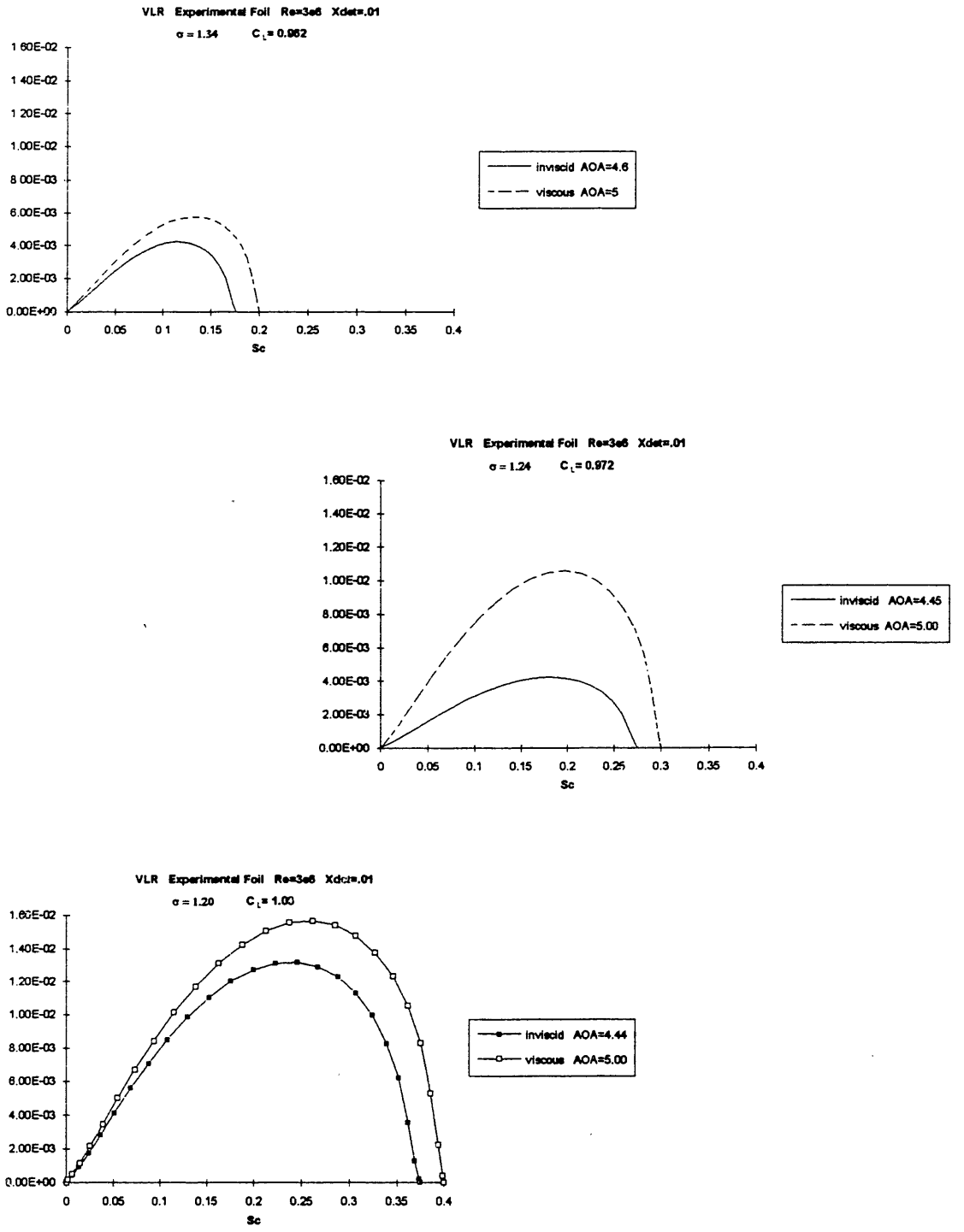

Figure (5-2) Comparison of inviscid and viscous cavity height distributions for the same cavitation number and lift coefficient for a VLR foil, at three different cavity lengths (Re=10^6).

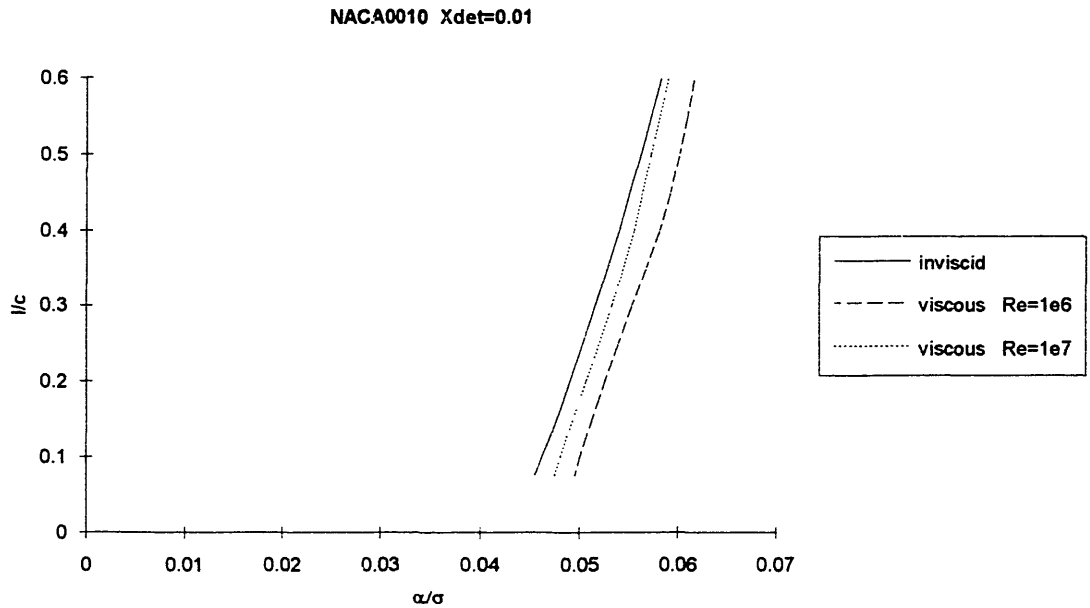

Figure (5-3) Comparison of inviscid and viscous curves of *l*/c vs. angle of attack/cavitation number.

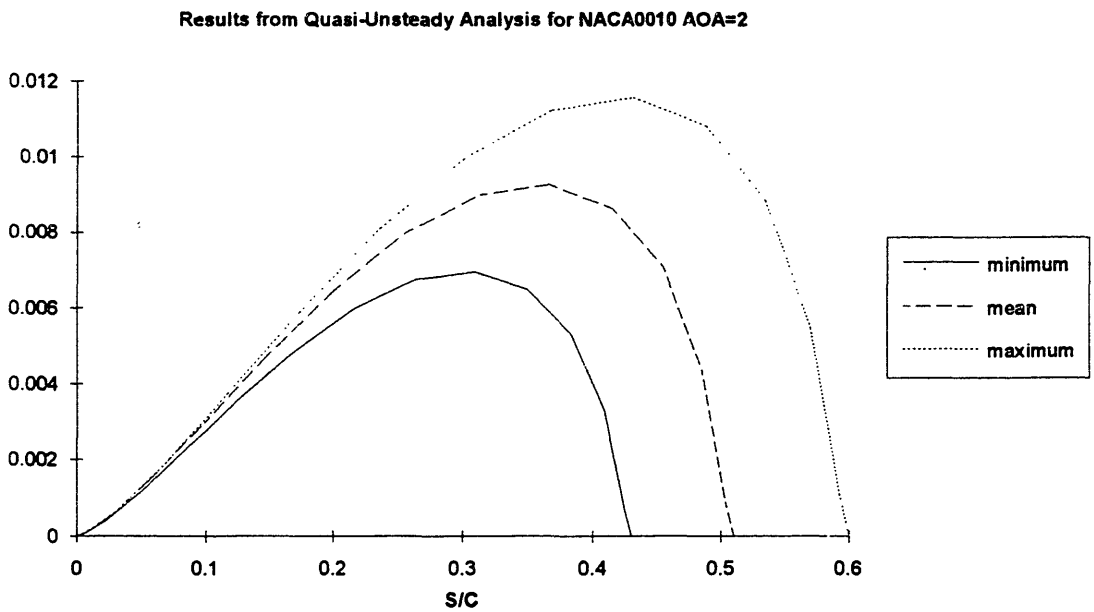

Figure (5-4) Comparison of cavity height distributions from the quasi-unsteady analysis.

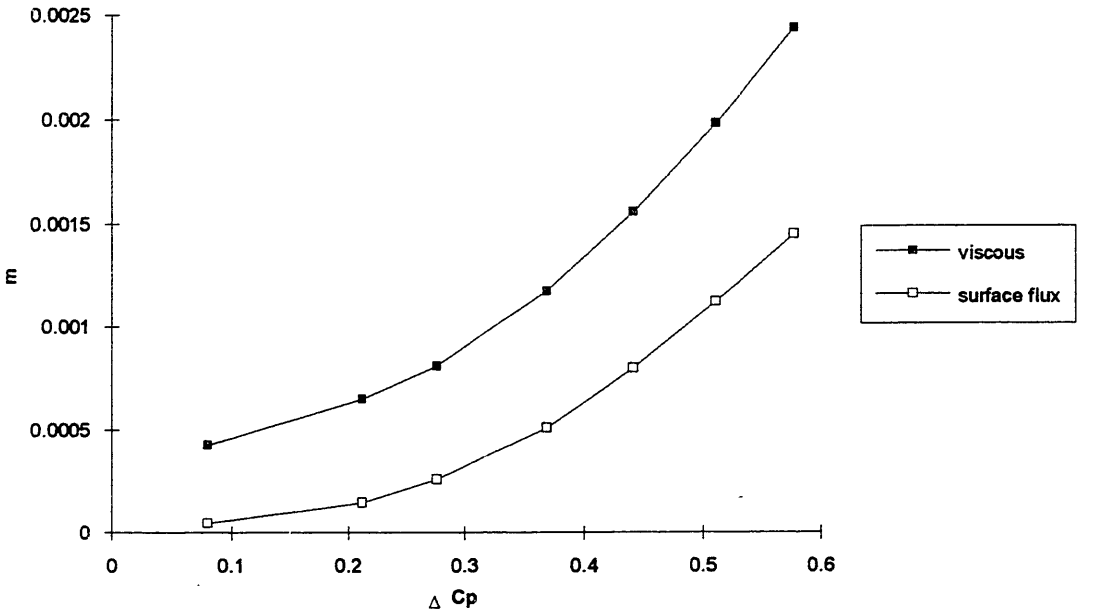

Figure (5-5) Mass flux at the trailing edge of the cavity for the viscous and open models.

References

[1] V.H. Arakeri. Viscous effects on the position of cavitation separation from smooth bodies. *Journal of Fluid Mechanics*, vol. 68, pp. 779-799, 1975.

[2] C. Brennen. Cavity surface wave patterns and general appearance. *Journal of Fluid Mechanics*, vol. 44, pp. 33-50, 1970.

[3] M. Drela. XFOIL: An analysis and design system for low reynolds number airfoils. In *Lecture Notes in Engineering (Volume 54, Low Reynolds Number Aerodynamics)*, Springer-Verlag, New York, 1989.

[4] M. Drela and M.B. Giles. Viscous-inviscid analysis of transonic and low reynolds number airfoils. *AIAA Journal*, 25(9), October 1987.

[5] N. Fine. *Nonlinear Analysis of Cavitating Propellers in Nonuniform Flow.* PhD thesis, M.I.T., Department of Ocean Engineering, October 1992.

[6] J.P. Franc and J.M. Michel. Attached cavitation and the boundary layer: experimental investigation and numerical treatment. *Journal of Fluid Mechanics*, vol. 154, pp. 63-90, June 1984.

[7] J.A. Geurst. Linearized theory for partially cavitated hydrofoils. *Int. Shipbuilding Progress*, Vol. 6, No. 60, August 1959.

[8] Gary S. Hufford. *Viscous Flow Around Marine Propellers Using Boundary Layer Strip Theory.* Masters thesis, M.I.T., Department of Aeronautics and Astronautics, June 1992.

[9] H. Kato, N. Takasugi, and H. Yamaguchi. Numerical analysis of a cavitating hydrofoil with finite span. In *Int. Symp. on Propulsors and Cavitation*, Hamburg, June 1992.

[10] J.E. Kerwin. The MIT Marine Hydrodynamics Water Tunnel - A 53rd Anniversary Celebration. May 21 1991. Presented at the New England Section SNAME Meeting, MIT.

[11] S.A. Kinnas. Hydrofoil Lift and Drag from Momentum Integrations. Technical Report 91-4, MIT, Department of Ocean Engineering, November 1991.

[12] S.A. Kinnas and N.E. Fine. Non-linear analysis of the flow around partially or super-cavitating hydrofoils by a potential based panel method. In *Boundary*

Integral Methods-Theory and Applications, Proceedings of the IABEM-90 Symposium of the International Association for Boundary Element Methods, pp 289-300, Springer-Verlag, Rome, Italy, October 1990.

[13] R. Knapp, J.W. Daily and F.G. Hammitt. *Cavitation,* McGraw-Hill, New York, 1970.

[14] Jin-Tae Lee. *A Potential Based Panel Method for the Analysis of Marine Propellers in Steady Flow.* PhD thesis, M.I.T., Department of Ocean Engineering, August 1987.

[15] P. Leehey. Supercavitating hydrofoil of finite span. In *IUTAM Symposium on Non-Steady Flow of Water at High Speeds,* PP. 277-298, Leningrad, June 1971.

[16] H. Lemonnier and A. Rowe. Another approach in modelling cavitating flows. *Journal of Fluid Mechanics,* vol. 195, pp. 557-580, April 1988.

[17] M.C. Meijer. Some experiments on partly cavitating hydrofoils. *Int. Shipbuilding Progress,* vol. 6(no 60), pp 361-368, August 1959.

[18] Jack Moran. An Introduction to Theoretical and Computational Aerodynamics, pp 199-200, John Wiley & Sons, 1984.

[19] Luigi Morino and Ching-Chiang Kuo. Subsonic potential aerodynamics for complex configurations: A general theory. *AIAA Journal,* vol. 12(no 2):pp 191-197, February 1974.

[20] J.N. Newman. *Marine Hydrodynamics.* The MIT Press, Cambridge, Massachusetts, 1977.

[21] M.P. Tulin. Steady two-dimensional cavity flows about slender bodies. Report 834, David Taylor Model Basin, 1953.

[22] J.S. Uhlman. A partially cavitated hydrofoil of finite span. *Journal of Fluids Engineering,* 100(3), pp. 353-354, September 1978.

[23] J.S. Uhlman. The surface singularity method applied to partially cavitating hydrofoils. *Journal of Ship Research,* vol 31(No. 2):pp. 107-124, June 1987.

[24] T.Y. Wu. A free streamline theory for two-dimensional fully cavitated hydrofoils. *J. Maths Phys.* vol 35, pp 236-265, 1956.

[25] T.Y. Wu. Cavity and wake flows. *Annual Review of Fluid Mechanics,* vol. 4, 1972.

[26] William C. Zierke and Steven Deutsch. The Measurement of Boundary Layers on a Compressor Blade in Cascade. NASA Contractor Report 185118, vol I, July 1989.